LRP 698/01 July 2001

Papers presented at the

28TH EPS CONFERENCE ON CONTROLLED FUSION AND PLASMA PHYSICS

Funchal, Madeira, Portugal
June 2001

Available in colour on the web at
crppwww.epfl.ch/crppabout/documents/conference/EPS01

ISSN 0458-5895

LIST OF CONTENTS

Stability and energy confinement of highly elongated plasmas in TCV

F. Hofmann, R. Behn, S. Coda, T.P. Goodman, M. Henderson, P. Lavanchy, Ph. Marmillod, Y. Martin, A. Martynov, J. Mlynar, J.-M. Moret, A. Pochelon, H. Reimerdes, O. Sauter, S. Alberti, C. Angioni, K. Appert, J. Bakos[1], P. Blanchard, P. Bosshard, R. Chavan, I. Condrea, A. Degeling, B.P. Duval, D. Fasel, J.-Y. Favez, A. Favre[2], I. Furno, P. Gomez[3], P. Gorgerat, J.-P. Hogge, P.-F. Isoz, B. Joye, I. Klimanov, J.B. Lister, X. Llobet, J.-C. Magnin, A. Manini, B. Marlétaz, J.-M. Mayor, P. Nikkola, P.J. Paris, A. Perez, Z.A. Pietrzyk[4], V. Piffl[5], R.A. Pitts, A. Scarabosio, E. Scavino, A. Sushkov[6], G. Tonetti, M.Q. Tran, H. Weisen, A. Zabolotsky

Centre de Recherches en Physique des Plasmas,
Association EURATOM - Confédération Suisse,
Ecole Polytechnique Fédérale de Lausanne, CH-1015 Lausanne, Switzerland

[1]KFKI-RMKI, Budapest, Hungary

[2] present address: EEMA Engineering, CH-2003 Neuchâtel, Switzerland

[3] present address: CEA, Cadarache, DRFC, St.-Paul-lez-Durance, France

[4] present address: Redmond Plasma Physics Laboratory, University of Washington, Redmond WA 98052, USA

[5]IPP, Prague, Czech Republic

[6]INF, Russian Research Centre, Kurchatov Institute, Moscow, Russian Federation

Abstract

The operating space of the TCV tokamak has been extended to higher elongation, κ=2.8, and higher normalised current, $I_N=I_P/aB$=3.6MA/mT, than were previously attainable. This has been achieved by optimising the parameters of the vertical position control system and by optimising the plasma shape. Experimental current and beta limits were found to be consistent with ideal MHD stability calculations, using measured plasma shapes and profiles. The sawtooth period was measured as a function of elongation and sawtooth oscillations are found to disappear, at high elongation, when the internal inductance drops below l_i~0.69. MHD events at high elongation have been analysed, using magnetic fluctuation measurements. The electron energy confinement time at high elongation, $2.2<\kappa<2.7$, shows a strong dependence on density and power flux through the plasma surface, but no statistically significant dependence on κ. Finally, we have applied off-axis, second harmonic, X-mode electron cyclotron resonance heating (ECRH) in order to flatten the current profile and improve vertical stbility. This gave access to previously inaccessible domains in κ-I_N space.

1. Introduction

Tokamak plasmas with elongated and shaped cross-sections have been studied in many laboratories around the world. Elongated plasmas allow higher plasma currents and higher beta values, and yield better energy confinement than circular ones [1-4]. However, elongated plasmas are inherently unstable with respect to an axisymmetric mode, the so-called vertical instabilty. This instability can lead to Vertical Displacement Events (VDEs) and disruptions which can produce large mechanical forces due to induced currents in the vacuum vessel. The instability can be stabilised by a combination of passive structures and active feedback coils, under the condition that there is a finite stability margin with respect to the ideal axisymmetric mode. The stability margin is defined as $m_s=1/(\gamma \tau_V)$, where γ is the open-loop growth rate of the n=0 mode and τ_V is the decay time of the stabilising currents in the passive structures. The optimum elongation depends on a number of parameters, such as major radius, toroidal magnetic field, aspect ratio, etc., and is by no means obvious. TCV was designed to push the elongation as high as possible, in order to find out whether the favourable trends which were observed in several tokamaks at moderate elongation would remain valid at higher elongation.

In this paper, we first describe how the operating space of TCV was extended to κ=2.8, we then discuss the stability limits that were encoutered in this process and we investigate MHD phenomena and electron energy confinement of highly elongated plasmas. Finally, we report on initial experiments of current profile modification, using ECRH, with the aim of improving the vertical stability.

2. Extension of the TCV operating space

2.1. Optimisation of the vertical position control system

TCV has a unique vertical position control system using active feedback coils both outside and inside the vacuum vessel [5]. The external coils are driven by slow power supplies with a response time of ~1ms. They are used for proportional and derivative feedback. The internal coils are driven by a fast supply with a response time of less than 0.1ms and they are used for derivative feedback only.

Closed-loop, axisymmetric stability of the complete system depends on a large number of parameters, such as the properties of the vertical position observer, the signal processing electronics, the PID gains, the power supply characteristics, the location of active coils, the geometry of passive stabilisers and finally, the plasma parameters themselves (shape, current distribution, plasma-wall distance, stability margin, etc.). In order to achieve the maximum possible elongation or, equivalently, the minimum stability margin, all of the above parameters must be optimised. This cannot be performed experimentally, by trial-and-error methods, since the number of parameters to be varied is too large. For TCV, we use a numerical model [6], the Deformable Plasma Model (DPM), to optimise the important parameters. This model has been shown to give good agreement with experimental results [7].

The stability of the closed-loop system depends on three feedback gains, i.e. the proportional (P) and derivative (D) gains in the slow loop, acting on the external coils, and the fast derivative gain (G) in the fast loop, acting on the internal coils. As an example, we show the stable domain in three-dimensional gain space, predicted by the DPM for a typical TCV plasma (Fig.1). For each value of the fast gain, G, there is a tear-drop shaped stable island in the plane of the slow gains, P and D [6]. The size of the stable island increases with G, but when G exceeds a critical value (G=74 ms in Fig.1), stablity is lost. The volume of the stable domain in gain space (Fig.1), for a given plasma, can be considered as a measure of the overall performance of the con-

trol system. We have used the DPM to optimise those system parameters that can actually be varied in the experiment, i.e. the observer characteristics, the transfer functions characterising the feedback loop and the configuration of the external active coils. The result of this optimisation is that we can now operate at very low stability margins, typically $m_s>0.03$. A further reduction of the stability margin would be extremely difficult to achieve and would not lead to any significant extension of the operating space.

2.2. Plasma shape optimisation

The shape of the plasma boundary in TCV can be approximately described by the expressions $R = R_0+a\,[\cos(\theta+\delta\sin\theta - \lambda\sin2\theta)]$, $Z = Z_0+a\,\kappa\sin\theta$, where R_0 and a are the major and minor radii, respectively, Z_0 measures the vertical position of the magnetic axis, and κ, δ, and λ designate elongation, triangularity and squareness, respectively. It is well known that both n=1 external kink stability and n=0 axisymmetric stability, at a given elongation, depend on triangularity and squareness [8]. In order to find the best combination of δ and λ, at fixed elongation, we have performed n=0 and n=1 stability calculations using the DPM [6] and KINX [9] codes. The DPM model gives us the n=0 growth rate in presence of all passive conductors in TCV and KINX is used to calculate the low beta current limit for a given plasma shape and current profile. As a starting point, we use a reconstructed experimental TCV equilibrium with κ=2.70. We then vary triangularity and squareness and, for each combination (δ, λ), we increase the total current, until we reach the n=1 stability limit. The reason for increasing the current to its limit is that, in Ohmic plasmas, the internal inductance and, consequently, the n=0 growth rate decrease with increasing current. The DPM model is then used to compute the n=0 growth rate, for those plasmas

which are close to the n=1 stability limit, as a function of δ and λ (Fig.2). We note that the n=0 growth rate has a minimum when $\delta \sim 0.6$ and $\lambda \sim 0.25$ and conclude that, for Ohmic plasmas, this corresponds to the optimum choice of the shape parameters. This result has been confirmed experimentally. In fact, virtually all experiments at high elongation, $\kappa > 2.5$, were performed with triangularities in the range $0.53 > \delta < 0.63$ and squareness, $0.22 > \lambda > 0.26$. Experimental variations of δ and λ outside these domains have not produced any improvement in the axisymmetric stability. It should be noted that the optimum plasma shape, as it is defined here, depends, to a large extent, on the shape of the conducting shell which serves as a passive stabiliser. In TCV, relatively high values of λ are necessary for good n=0 stability because the shape of the passive stabiliser, i.e. the vacuum vessel, is rectangular. In other tokamaks with D-shaped vacuum vessels the optimum plasma shape is characterised by lower values of λ and higher values of δ [4].

3. Comparison of experimental and theoretical stabilty limits

3.1. Stability limits in κ-I_N space

Figure 3 shows the normalised current, $I_N = I_P/(a\,B)$, as a function of elongation. Experimental results are shown as red squares and theoretical stability limits with respect to the n=0 and n=1 modes are shown as heavy black lines. We note that there is an upper limit to the normalised current, given by the ideal n=1 external kink. There is also a lower limit to the normalised current since, in Ohmic plasmas, the internal inductance and the n=0 growth rate both increase with decreasing current, and the minimum current is reached when the n=0 stability margin approaches zero. The accessible operating window in plasma current becomes smaller as the elongation increases (Fig.3). In Fig.4, we show the safety factor at 95% of the poloidal flux,

as a function of elongation, and it is evident that, at high elongation, $\kappa>2.3$, the experimental current limit is no longer given by $q_{edge}=2$, but is characterised by progressively higher q-values as κ increases. This is in agreement with ideal MHD stability calculations, using experimental plasma shapes and profiles.

3.2. Current and beta limits

The ideal MHD beta limit, as given by the n=1 external kink, for a D-shaped plasma in TCV, with Ohmic current profile and $\kappa=2.5$, is shown in Fig.5 as a function of the normalised current. The stability limit is shown as a band of finite width to indicate the effect of small variations in the pressure and current profiles within the experimental uncertainties. On the same figure, we plot all TCV experimental equilibria with $\kappa<2.5$ and we see that the experiments are entirely consistent with the theoretical predictions. It should be noted that the theoretical stability limit was computed for $\kappa=2.5$, whereas the experimental points include all elonagtions in the range $1<\kappa<2.5$. However, at low current, the theoretical stability limit is given by the Troyon scaling law [10], which is independent of elongation. Fig.5 shows that we have reached the beta limit at very low and very high values of the normalised current. At intermediate values of I_N, however, where the beta limit is highest, the experimental points are still far from the limit. The reason for this is that plasmas with $\kappa=2.5$ and $I_N\sim2$ are beyond the ideal n=0 stability limit, unless the current profile can be broadened by ECRH, as will be discussed in section 5.

4. Characteristics of highly elongated plasmas

4.1. Sawteeth

The sawtooth period, τ_{ST}, in highly elongated plasmas, $2.3<\kappa<2.8$, generally decreases with elongation, as shown in Fig.6. In the discharge shown here, the density was higher during current rampup than during rampdown. Since the sawtooth period is roughly proportional to the density [11], rampup and rampdown values are different (blue triangles in Fig.6). However, if we normalise the sawtooth period to the density, rampup and rampdown values are approximately the same revealing the true dependence on elongation (red triangles in Fig.6). When the elongation increases, a discontinuity is observed at $\kappa\cong1.9$, after which the sawtooth period, and the relative soft X-ray fluctuation amplitude, continue to decrease up to an elongation between 2.3 and 2.6, where the sawteeth disappear. This transition occurs at a very precise value of the internal inductance, $l_i=0.69$, whereas the sawtooth inversion radius remains approximately constant throughout this scenario, $\rho_{inv}\cong0.49$. The electron temperature profile remains practically unchanged through the transition at $l_i=0.69$. Even without sawteeth, the electron temperature profile remains flat in the central plasma region with a sharp rollover in the vicinity of ρ_{inv}, suggesting that the q=1 radius does not change during the transition. Apparently, there are unstable modes, at very high elongation, which flatten the core temperature profile, even though the macroscopic sawteeth have disappeared [11].

4.2. MHD phenomena

MHD activity is analysed in TCV using magnetic fluctuation and soft X-ray emission diagnostics. Magnetic measurements are obtained from fast pick-up coils which measure fluctuations of the poloidal magnetic field inside the vacuum vessel. TCV is equipped with two toroidal pickup coil arrays in the equatorial plane, and four poloidal arrays. Bi-orthogonal decomposition of the magnetic measurements allows us to

deduce toroidal and poloidal mode numbers. Toroidal mode numbers are easily identified by inspection of the principal eigenvectors, whereas poloidal mode numbers are obtained from a comparison of the measurements with modelled island structures [12].

Three typical MHD phenomena which are observed in highly elongated plasmas are shown in Fig.7. The first, a VDE, is caused by a low n=0 stability margin, $m_s<0.03$ (Fig.7a). We note that the vertical displacement, $Z\ I_p$, reaches large values before the plasma current starts to decay. This behaviour reflects the fact that, in TCV, the plasma can move a considerable distance vertically without making contact with the top or bottom wall. Analysis of magnetic probe signals shows that the poloidal and toroidal mode numbers of this event are predominantly m/n=1/0. The second event (Fig.7b) is a burst of MHD activity causing a minor disruption. Such bursts usually appear at low q, close to the current limit. In the case shown here, the burst consists of a cascade of three different modes with mode numbers m/n=4/3, m/n=3/2 and m/n=5/4. All three modes rotate in the electron diamagnetic drift direction with a frequency which is approximately proportional to the toroidal mode number, f≅n*5kHz. Finally, the third event (Fig. 7c) is a current limit disruption preceeded by a locked mode with mode numbers m/n=2/1. The growth rate of this mode is approximately $1000s^{-1}$. Note that, in contrast to the VDE, the vertical displacement, $Z\ I_p$, remains relatively small and the plasma current shows the charactristic spike due to the rapid decrease of l_i.

4.3. Electron energy confinement

Previous work on TCV has shown the energy confinement time in ohmic plasmas to be strongly dependent on plasma shape [13,14]. Analysis of an extensive database of

discharges with $1.06 < \kappa < 1.86$ and $-0.41 < \delta < 0.72$ revealed that, for constant plasma density and edge safety factor, the confinement time increases with elongation and decreases with triangularity. This variation is not caused by changes in the underlying diffusivity, which in fact was found to be independent of shape; rather, the dependence of the global confinement on the plasma shape could be explained solely by the changes in the temperature gradients induced by the geometrical effects of flux expansion and compression, combined with degradation of the thermal conductivity with increasing energy flux. A subsequent study of ECW-heated plasmas confirmed the decrease of confinement time with triangularity but was unable to provide an unambiguous result for the dependence on elongation, owing to a strong correlation of the latter with the plasma current in the database [15].

The dataset discussed in the present paper, with $2.19 < \kappa_a < 2.73$, has provided an opportunity to extend the previous study of ohmic plasmas to considerably higher edge elongations and to put part of the conclusions of that study to the test. The present study covers only narrow ranges ($\pm$15%) of triangularity, magnetic field and plasma current. Thus, no significant information can be extracted on the dependence of confinement on these quantities. However, the dataset spans a broad range of values of the two crucial parameters on which confinement was found to depend in the previous study, namely the ohmic input power and the line-averaged density: $0.6 < P_{in} < 1.5$ MW and $1.5 \times 10^{19} < \bar{n}_e < 7.9 \times 10^{19}$ m^{-3}. Finally, the edge safety factor varies over the range $2.6 < q_a < 4.1$.

The global confinement is characterised in terms of τ_{Ee}, defined as the electron stored energy W_e divided by the power loss from the plasma. The electron stored energy is calculated by volume integraton of electron density and temperature profiles obtained by fitting Thomson scattering measurements at 20 to 28 spatial posi-

tions (depending on the elongation) along a vertical chord. The power loss is derived by subtracting the time derivative of the electron energy from the ohmic heating power, which typically constitutes only a 1-2% correction. Since no local ion temperature measurements are available in TCV, we are unable to provide a reliable estimate of either the total energy confinement time or the true electron energy confinement time; however, the quantity τ_{Ee} defined above constitutes a lower bound for the latter. For simplicity, we shall refer to τ_{Ee} as the electron energy confinement time. For the purposes of examining the dependence of confinement on shape, the considerations that follow are valid provided that the ratio of ion to electron stored energy for constant density and input power does not depend on shape.

The confinement time is studied as a function of elongation, line-averaged density $\bar{n}_e$ and edge power flux q_{oh}. The latter is calculated by subtracting the radiated power from the ohmic input power, and dividing the result by the surface area of the plasma boundary. It should be noted that the radiated power represents a substantial fraction, between 20% and 35%, of the total power loss; however, this ratio does not exhibit any dependence on plasma shape. Over the parameter range examined in the present study, the confinement time varies by more than a factor of 6. However, for constant $\bar{n}_e$ and q_{oh}, τ_{Ee} shows little dependence on elongation in the considered range. To quantify this observation, we performed straightforward offset-multilinear regressions on the logarithms for the two cases $\tau_{Ee}(\bar{n}_e, q_{oh}, \kappa)$ and $\tau_{Ee}(\bar{n}_e, q_{oh})$; in both cases error bars were obtained on the coefficients by error propagation from an estimated 25% uncertainty on the confinement time, and by locating the 95% confidence level. For the trilinear regression we obtained $\alpha_n = 0.93 \pm 0.20$, $\alpha_q = -0.86 \pm 0.38$, $\alpha_\kappa = 1.0 \pm 2.2$; thus, α_κ is essentially an indifferent parameter in the regression, showing only a slight increasing trend. In the bilinear regression the coefficients are $\alpha_n = 0.88$

$\pm$ 0.16 and α_q = -0.93 $\pm$ 0.35, virtually identical to their bilinear counterparts. The weak dependence on κ is clearly demonstrated by Figs. 8(a) and 8(b), which show the confinement time, normalised by the appropriate powers of $\bar{n}_e$ and q_{oh}, respectively, as a function of q_{oh} and $\bar{n}_e$.

Although a stronger dependence of confinement on elongation was observed at lower κ [13,14], the present result is in agreement with the interpretation of the dependence of τ_{Ee} on shape as a geometrical flux-surface effect. This effect is quantified by the "shape enhancement factor" (SEF), defined as the ratio of the confinement time of a shaped plasma to that of an appropriate reference cylindrical case [13,14]. The SEF is an increasing function of elongation with an asymptotic value of 2, and in practice begins to saturate for $\kappa > 2.2$ [16]: as κ goes from 2.19 to 2.73, the SEF increases typically by less than 6%.

The shape dependence could be factored out by dividing τ_{Ee} by the SEF, although this dependence is too weak to be of any significance. Indeed, an offset-bilinear regression for this case causes only minimal change in the coefficients from the previous one, yielding the result $\tau_{Ee}/SEF = C\, n_e^{\alpha_n} q_{oh}^{\alpha_q}$, with $\alpha_n = 0.89 \pm 0.18$ and α_q = -0.93 $\pm$ 0.39 [see Fig. 9(a)]. It should be noted that for the lower elongation database it was found that $\alpha_q \sim -0.5$ [14]; the power degradation thus appears to be more pronounced in this dataset. This, however, is not directly related to shape, rather to the power itself. The average input power is substantially larger for these discharges than those of the previous study; when the two datasets are examined jointly, it becomes apparent that $d(\log(\tau_{Ee}))/d(\log(q_{oh}))$ is a decreasing (negative) function of q_{oh}, and has little dependence on elongation or triangularity.

It is worthwhile testing this database, as was done for previous ones, against well-known scaling laws. The nearly linear dependence on density is immediately remi-

niscent of the Neo-Alcator scaling [17], which was found to provide a good description of lower elongation discharges, provided a correction was made for the SEF [16]. This comparison is hampered by our lack of detailed ion temperature information, since the Neo-Alcator scaling refers to the total plasma energy confinement time. We find, however, that good agreement is obtained again if the total ion energy is between 40% and 50% of the total available ohmic energy. By contrast, even the most generous assumption for the ion energy content makes the experimental confinement time at high κ fall well below that given by the ITER 1996 L-mode scaling [18]. This is due to the optimistic scaling with elongation ($\kappa^{0.64}$) in the ITER scaling, which is invalidated at high κ by the observed saturation of confinement with κ. In ohmic discharges as well as in many instances of ECH L-mode shots in TCV, the Rebut-Lallia-Watkins (RLW) expression for the electron energy confinement time [19] is generally found to hold remarkably well [14,15]. As shown in Fig. 9(b), the agreement remains satisfactory for the current dataset.

5. Current profile modification using ECRH

In this section, we present initial experiments using EC wave current profile broadening to create and stabilise high elongation, high q discharges, which would be Ohmically unstable. These experiments are motivated by the fact that, at high elongation, the theoretical beta limit reaches a maximum at relatively low values of the normalised current (I_N~2 in Fig.H), or equivalently, high values of q. Several different EC schemes can, in principle, be used to broaden the current profile: off-axis ECH, on-axis counter-ECCD or off-axis co-ECCD. PRETOR transport code simulations [20], using local RLW heat transfer coefficients [19] show that off-axis ECH is the preferred scheme for profile broadening. The optimum deposition radius in off-axis

ECH is approximately given by $\rho=0.7$, where ρ is defined as $\rho=[V/V_{LCFS}]^{1/2}$ and V and V_{LCFS} are the volumes inside the flux surface under consideration and inside the last closed flux surface, respectively [11].

The standard EC launch scenario in these experiments uses two gyrotrons at the second harmonic frequency, with a total power of 1MW, shared between upper lateral and equatorial launchers [21]. The discharges are pre-programmed with constant quadrupole and hexapole fields throughout the Ohmic and EC heated phases. If we use a high pre-programmed triangularity, similar to that used in Ohmic discharges, we obtain a bean-shaped plasma cross-section in the EC heated phase, with 8% indentation on the high-field side (HFS). This leads to very high central elongation, $\kappa_0 \sim \kappa_{edge}$, and poor vertical stability due to an increased inboard and outboard plasma-wall distance. By decreasing the pre-programmed triangularity, the indentation during the EC heated phase is removed, the elongation on axis is reduced and the vertical stability is considerably improved. This allows operation at high elongation and high q-values ($\kappa=2.4$, $q_{95}=8.3$), which would be impossible with peaked Ohmic profiles. It is interesting to note that Ohmic plasmas with the same elongation, $\kappa=2.4$, are vertically unstable for $q_{95}>3.1$.

A typical discharge is shown in Fig.10a. The elongation increases from $\kappa=1.8$ in the Ohmic phase to $\kappa=2.4$ in the EC heated phase. Simultaneously, the internal inductance decreases from $l_i=1.25$ to $l_i=0.83$, which can be attributed to both the increasing elongation and the flattening of the current profile. Open-loop growth rates of the vertical instabilty, as obtained from a rigid displacement model [6], are $\gamma=996s^{-1}$ in the Ohmic phase and $\gamma=2238s^{-1}$ in the EC phase, at time t=1.4s, when the elongation reaches its maximum value. While the launch angle of the upper beam is kept constant, the lower beam is swept downward during the discharge in order to keep the

deposition radius approximately constant at ρ~0.7 (Fig.10b). A disruption-free termination of the discharge was obtained by shutting off the ECH power only after the start of the pre-programmed elongation ramp-down. Off-axis ECH broadens the electron temperature profile, as seen in Fig.11. A power balance analysis shows that the application of off-axis ECH reduces the electron thermal conductivity in the central plasma region, inside the deposition radius, and increases it in the outer region [11].

6. Conclusions

Highly elongated, Ohmic plasmas with $\kappa<2.8$ and $I_N<3.6$MA/mT have been created in TCV. The experiments show that the normalised plasma current is constrained by a lower limit, imposed by axisymmetric stability, and an upper limit, given by the n=1 external kink mode. The stable operating window between these two limits becomes smaller as the elongation increases. We have shown experimentally that the classical current limit, defined by $q_{edge}=2$, is only valid up to an elongation of κ~2.3. At higher elongations, $2.3<\kappa<2.8$, the current limit is characterised by progressively higher values of q. This is consistent with ideal MHD stability calculations, with the experimental plasma shapes and profiles.

Soft X-ray measurements show that the sawtooth period decreases with elongation and that the sawtooth oscillations disappear, at very high elongation, when the internal inductance is less than l_i~0.69. Several types of MHD events have been observed in these experiments. At high elongation, we frequently see bursts of MHD activity, consisting of cascades of several different rotating modes. These bursts can either cause a minor disruption or they can lead to a locked mode, followed by a major disruption. Electron energy confinement times at high elongation, $2.2<\kappa<2.7$, were

measured using Thomson scattering data. A statistical analysis of these results shows that the confinement time increases with density and decreases with power flux through the plasma surface, but there is no significant dependence on elongation. This is in contrast to earlier results at lower elongation, where a clear increase of τ_{Ee} with κ was observed [16].

Current profile modification has been achieved by far off-axis application of second harmonic, X-mode ECRH power. This has allowed a substantial extension of the operating space at high q-values. For example, at an elongation κ=2.4, the maximum value of q_{95} obtainable without loosing vertical stability, has been increased form 3.1 to 8.3 by ECRH current profile tailoring. In future experiments, it is planned to apply this method to plasmas with higher current and higher elongation, κ>2.4, using a combination of second and third harmonic ECH [22].

Acknowledgements

This work was supported in part by the Swiss National Science Foundation.

References

[1] Lomas, J.P., et al., Plasma Phys. Control. Fusion 42 (2000) B115.

[2] Cordey, J.G., et al., Plasma Phys. Control. Fusion 39 (1997) B115.

[3] Kamada, Y., et al., in Fusion Energy 1996 (Proc. 16th Int. Conf. Montreal, 1996), Vol. 1, IAEA, Vienna (1997) 247.

[4] Lazarus, E.A., et al., Phys. Fluids B4 (1992) 3644.

[5] Hofmann, F. et al., Nucl. Fusion 38 (1998) 399.

[6] Hofmann, F. et al., Nucl. Fusion 38 (1998) 1767.

[7] Hofmann, F. et al., Nucl. Fusion 40 (2000) 767.

[8] Eriksson, G. et al., in 1992 International Conference on Plasma Physics (Proc. Conf. Innsbruck 1992), Vol. 16C, Part I, European Physical Society, Geneva (1992) I-343.

[9] Degtyarev, L. et al., Comput. Phys. Commun. 103 (1997)10.

[10] Troyon, F. et al., Plasma Phys. Control. Fusion 26 (1984) 209.

[11] Pochelon, A., et al., accepted for publication in Nuclear Fusion.

[12] Reimerdes, H., Ph.D. Thesis, EPFL, Lausanne, 2001.

[13] Moret. J.-M. et al., Phys. Rev. Letters 79 (1997) 2057.

[14] Weisen, H. et al., Nucl. Fusion 37 (1997) 1741.

[15] Pochelon, A. et al., Nucl. Fusion 39 (1999) 1807.

[16] Weisen, H. et al., Plasma Phys. Control. Fusion 39 (1997) B135

[17] Parker, R. R. et al., Nucl. Fusion 25 (1985) 1127.

[18] Kaye, S. M. et al., Nucl. Fusion 37 (1997) 1303.

[19] Rebut, P.H., et al., in Proc. 12th Int. Conf. Plasma Physics and Controlled Nuclear Fusion Research, Nice 1988, IAEA, Vienna 1989, Vol. 2, 191.

[20] Angioni, C., et al., in Proc. Theory of Fusion Plasmas, Varenna 2000, ISSP-19 (Editrice Compositori, Bologna, 2001) 73.

[21] Goodman, T.P., et al., 19th Symp. Fusion Technology, Lisbon 1996, Vol. I (1996) 565.

[22] Alberti, S., et al., Proc. 18th IAEA Fusion Energy Conf., Sorrento 2000, paper PD/2.

Figure Captions

Fig.1. Stable volume of the closed-loop vertical position control system, in three-dimensional gain space, as predicted by the DPM for a D-shaped plasma with I_P=351kA, B_T=1.0T, κ=2.1, δ=0.42 and $\gamma_{n=0}$=2300s^{-1}.

Fig.2. Growth rate of the n=0 mode, in s^{-1},as a function of triangularity and squareness, for plasmas with κ=2.7, which are close to the n=1 current limit.

Fig.3. Normalised current, $I_N=I_P/(a\ B)$, vs. elongation. Experimental results, obtained from D-shaped, Ohmic plasmas with $0.4<\delta<0.6$, are shown as red squares. Theoretical stability limits with respect to the n=0 and n=1 modes are shown as black lines.

Fig.4. Safety factor at 95% of the poloidal flux vs. elongation. Experimental results, shown in green, include all TCV discharges between March 1994 and May 2001. The theoretical current limit is shown approximately by the red line.

Fig.5. Toroidal beta vs. normalised current. Experimental results, obtained from MHD equlibrium reconstructions, are shown in green. They include all TCV discharges with $\kappa<2.5$ between March 1994 and May 2001. Theoretical stability limits are indicated by the band between the two red lines.

Fig.6. Sawtooth period (blue) and normalised sawtooth period (red) as a function of elongation for a discharge whose maximum elongation was 2.65.

Fig.7. Typical MHD events in highly elongated plasmas: (a) Vertical Displacement Event, (b) Burst of MHD activity, and (c) locked mode leading to a major disruption.

Fig.8. Electron energy confinement time, (a) divided by $\bar{n}_e^{0.88}$, as a function of the power flux q_{oh}, and (b) multiplied by $q_{oh}^{0.93}$, as a function of the line-averaged electron density $\bar{n}_e$. The color coding refers to the edge elongation κ_a.

Fig.9. (a) Experimental fit of the electron energy confinement time, corrected for the shape enhancement factor, to a power law in the line-averaged density and in the power flux; (b) experimental electron energy confinement time vs. Rebut-Lallia-Watkins scaling.

Fig.10. Current profile modification with ECRH: (a) Evolution of plasma parameters, (b) Poloidal view of plasma shapes and ECRH beams at 3 times (0.55s, 0.75s, 1.40s). Cold resonance location and q=1 surface in the Ohmic phase (0.55s) are shown as dashed lines.

Fig.11. Temperature and density profiles obtained from Thomson scattering. Ohmic and ECRH phases are shown in blue and red, respectively.

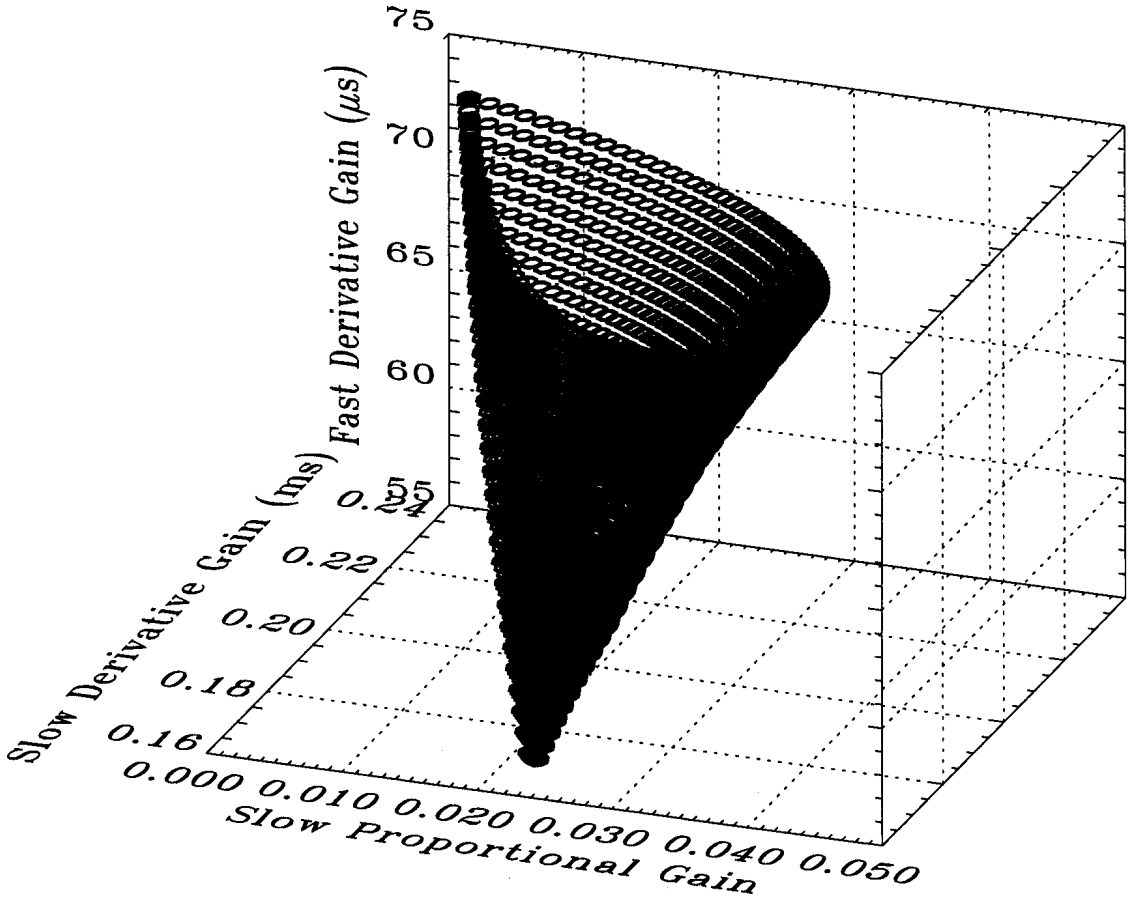
Fast Derivative Gain (μs)
75
70
65
60
55
Slow Derivative Gain (ms)
0.24
0.22
0.20
0.18
0.16
0.000 0.010 0.020 0.030 0.040 0.050
Slow Proportional Gain

Fig. 1

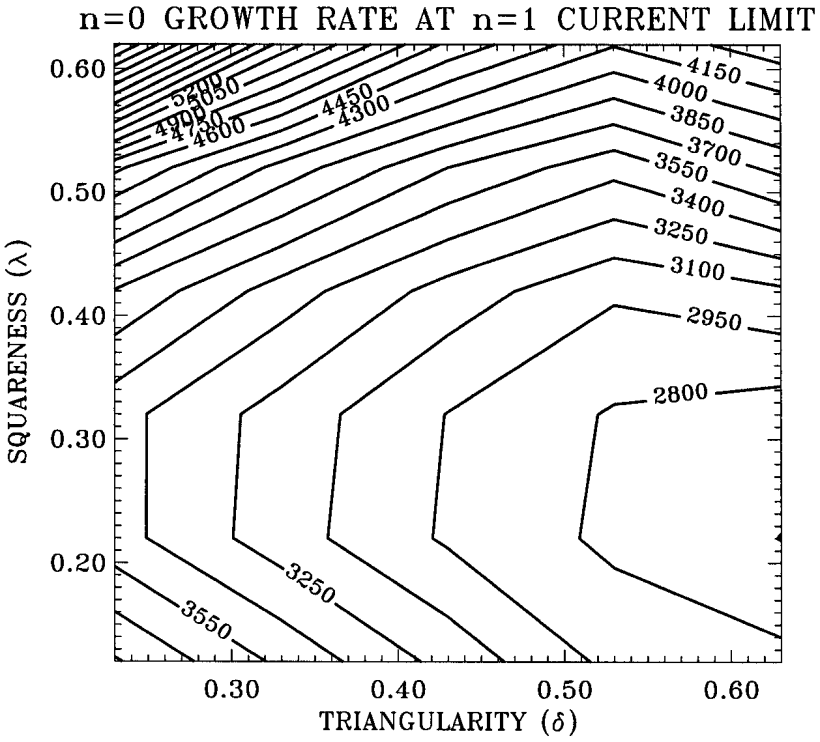
n=0 GROWTH RATE AT n=1 CURRENT LIMIT
SQUARENESS (λ)
TRIANGULARITY (δ)
0.60
0.50
0.40
0.30
0.20
0.30
0.40
0.50
0.60
4150
4000
3850
3700
3550
3400
3250
3100
2950
2800
4450
4300
4600
3250
3550

Fig. 2

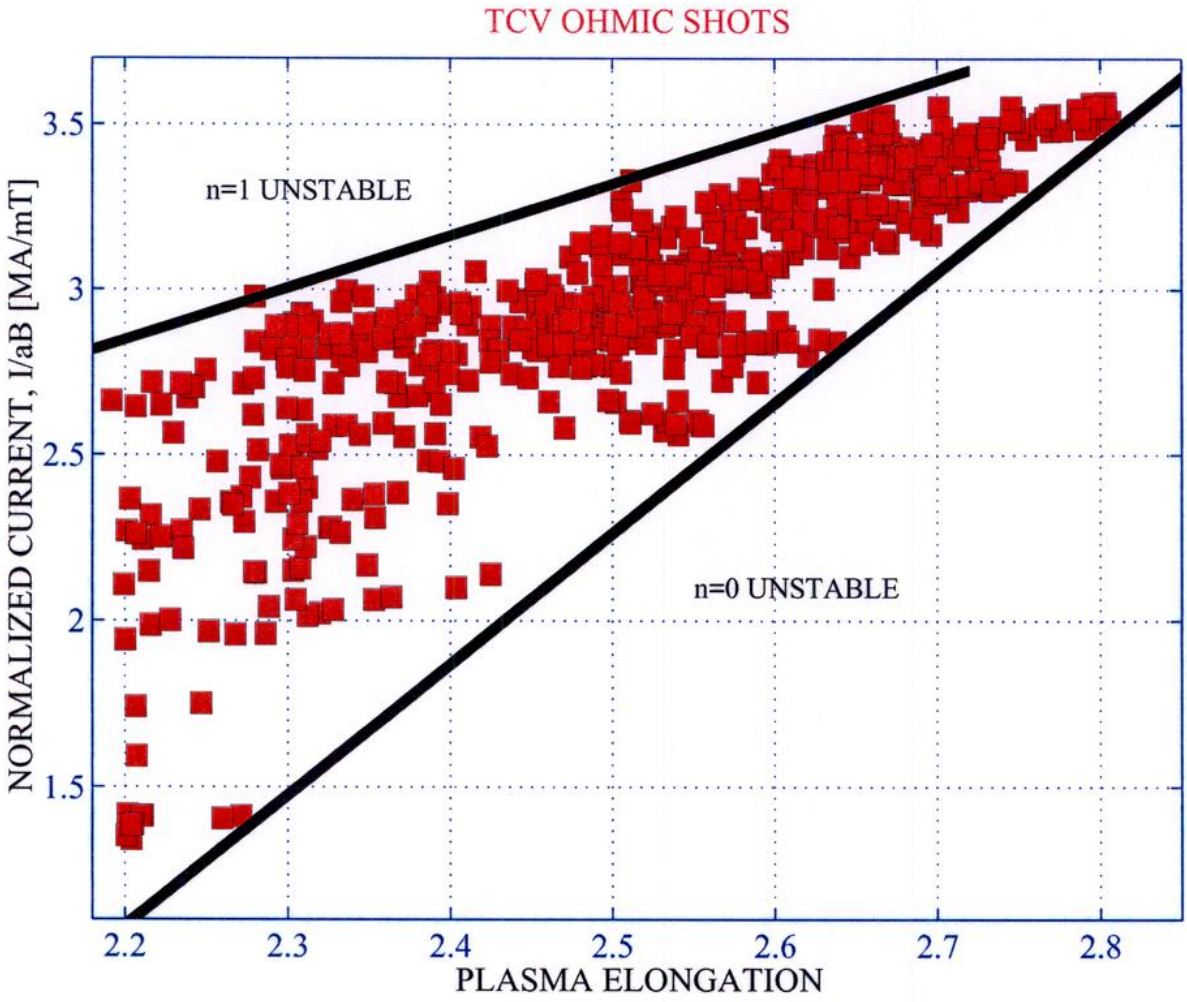
TCV OHMIC SHOTS
n=1 UNSTABLE
n=0 UNSTABLE
NORMALIZED CURRENT, I/aB [MA/mT]
PLASMA ELONGATION
3.5
3
2.5
2
1.5
2.2
2.3
2.4
2.5
2.6
2.7
2.8

Fig. 3

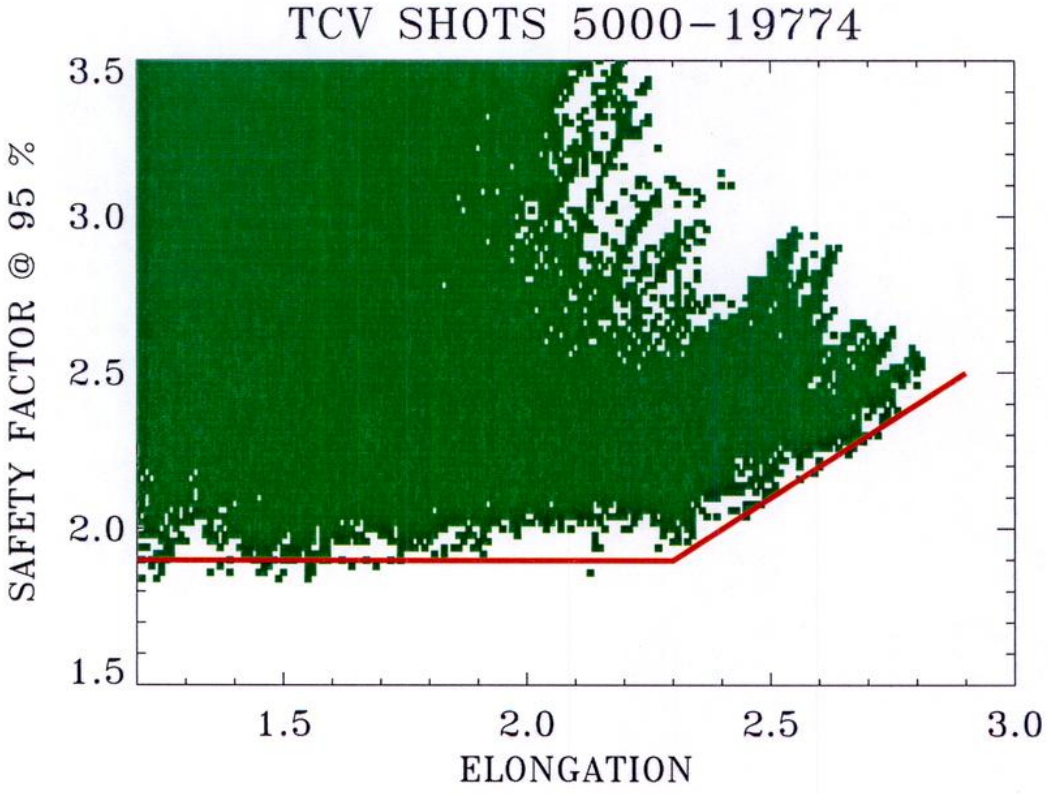
TCV SHOTS 5000-19774
SAFETY FACTOR @ 95 %
3.5
3.0
2.5
2.0
1.5
1.5
2.0
2.5
3.0
ELONGATION

Fig. 4

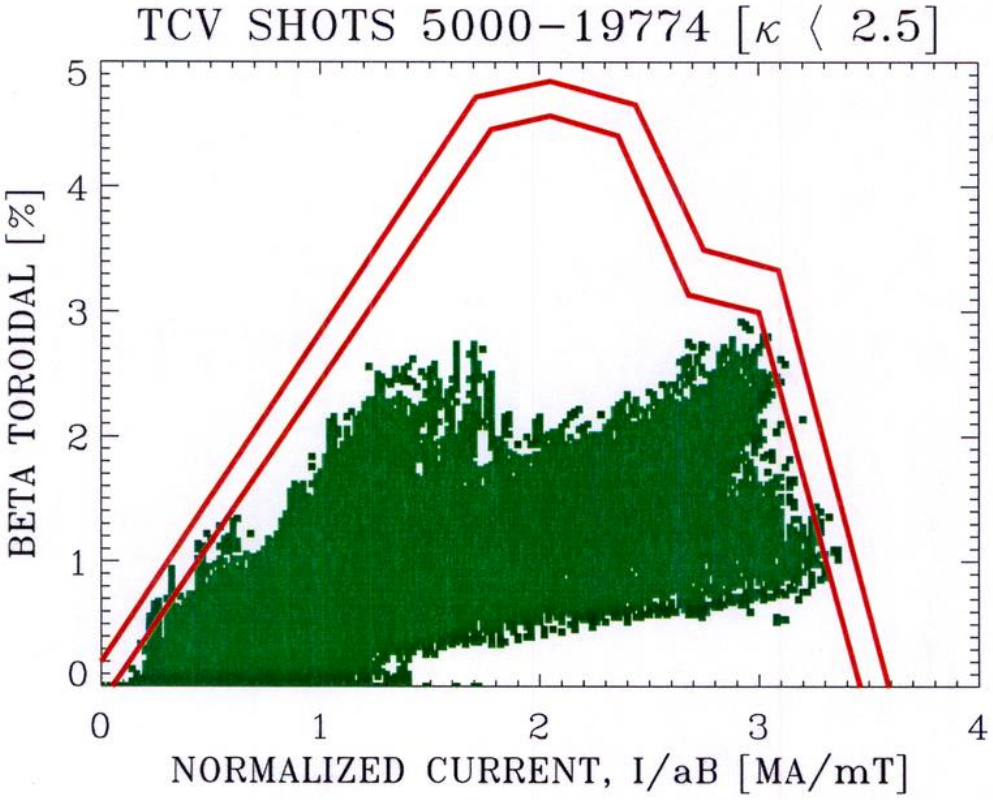
TCV SHOTS 5000−19774 [κ ⟨ 2.5]
BETA TOROIDAL [%]
NORMALIZED CURRENT, I/aB [MA/mT]
0
1
2
3
4
5

Fig. 5

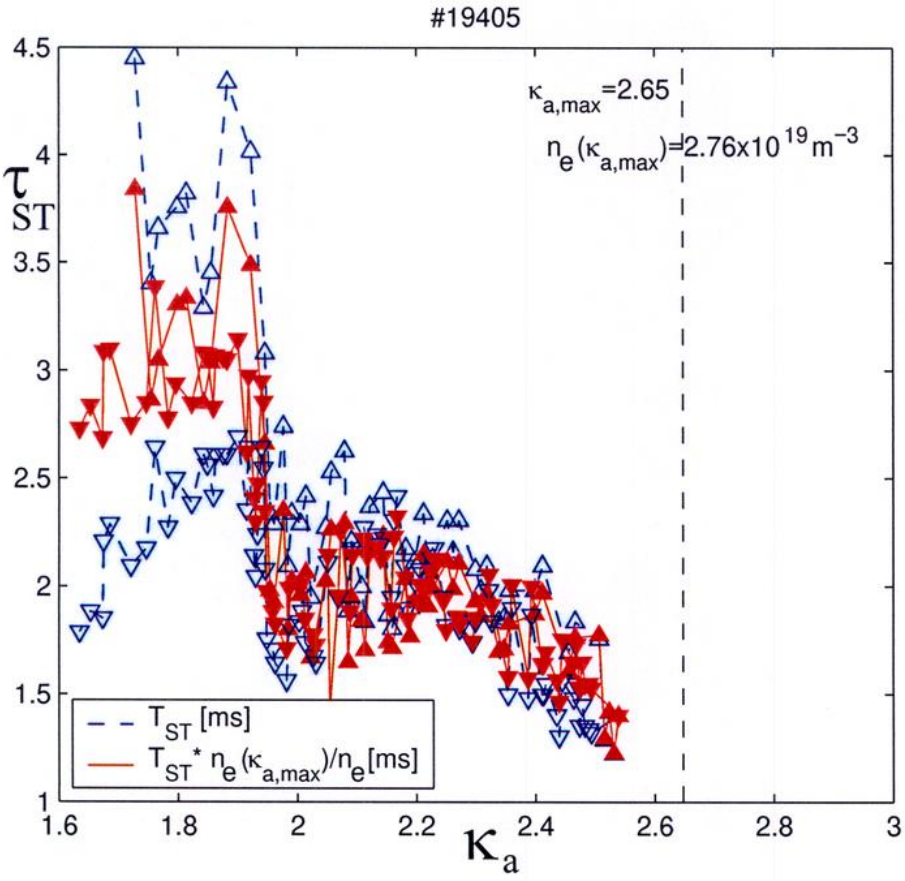
#19405
$\kappa_{a,max}$=2.65
$n_e(\kappa_{a,max})$=2.76x10^{19}m^{-3}
τ_{ST}
κ_a
T_{ST} [ms]
T_{ST}* $n_e(\kappa_{a,max})/n_e$[ms]
4.5
4
3.5
3
2.5
2
1.5
1
1.6
1.8
2
2.2
2.4
2.6
2.8
3

Fig. 6

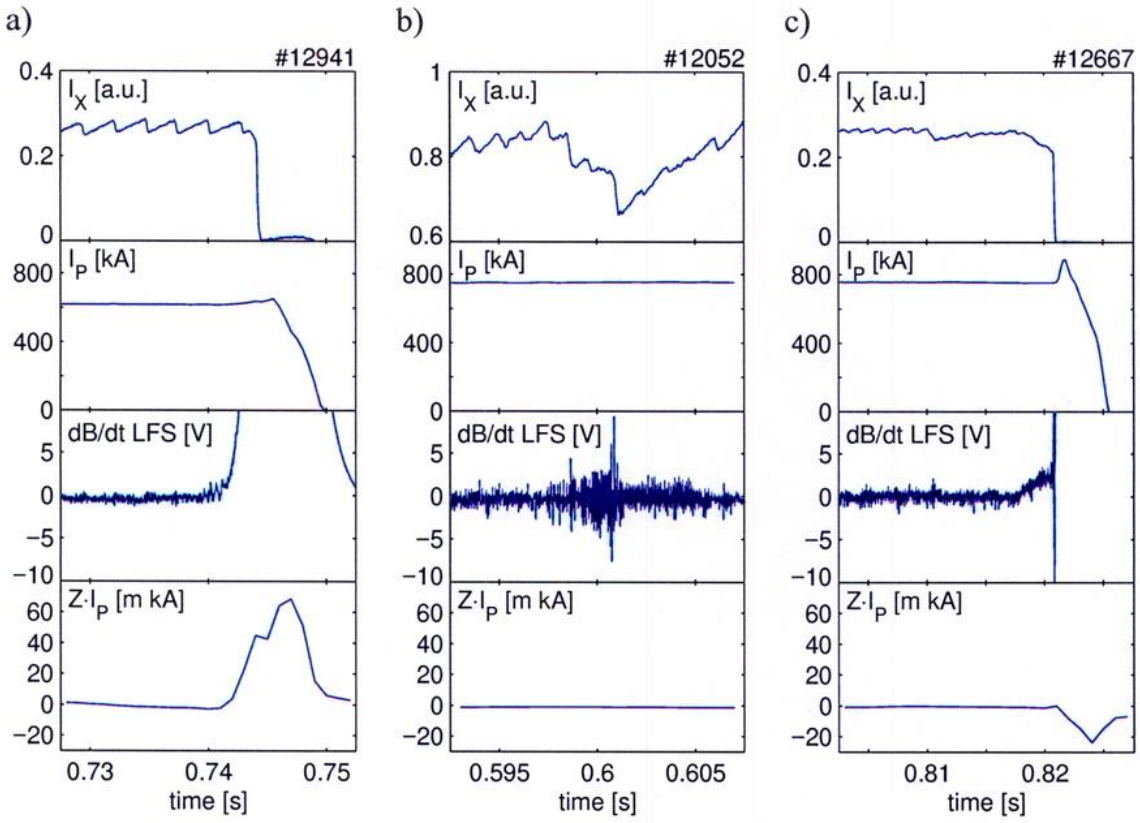
a)
#12941
I_X [a.u.]
I_P [kA]
dB/dt LFS [V]
$Z \cdot I_P$ [m kA]
time [s]
b)
#12052
I_X [a.u.]
I_P [kA]
dB/dt LFS [V]
$Z \cdot I_P$ [m kA]
time [s]
c)
#12667
I_X [a.u.]
I_P [kA]
dB/dt LFS [V]
$Z \cdot I_P$ [m kA]
time [s]

Fig. 7

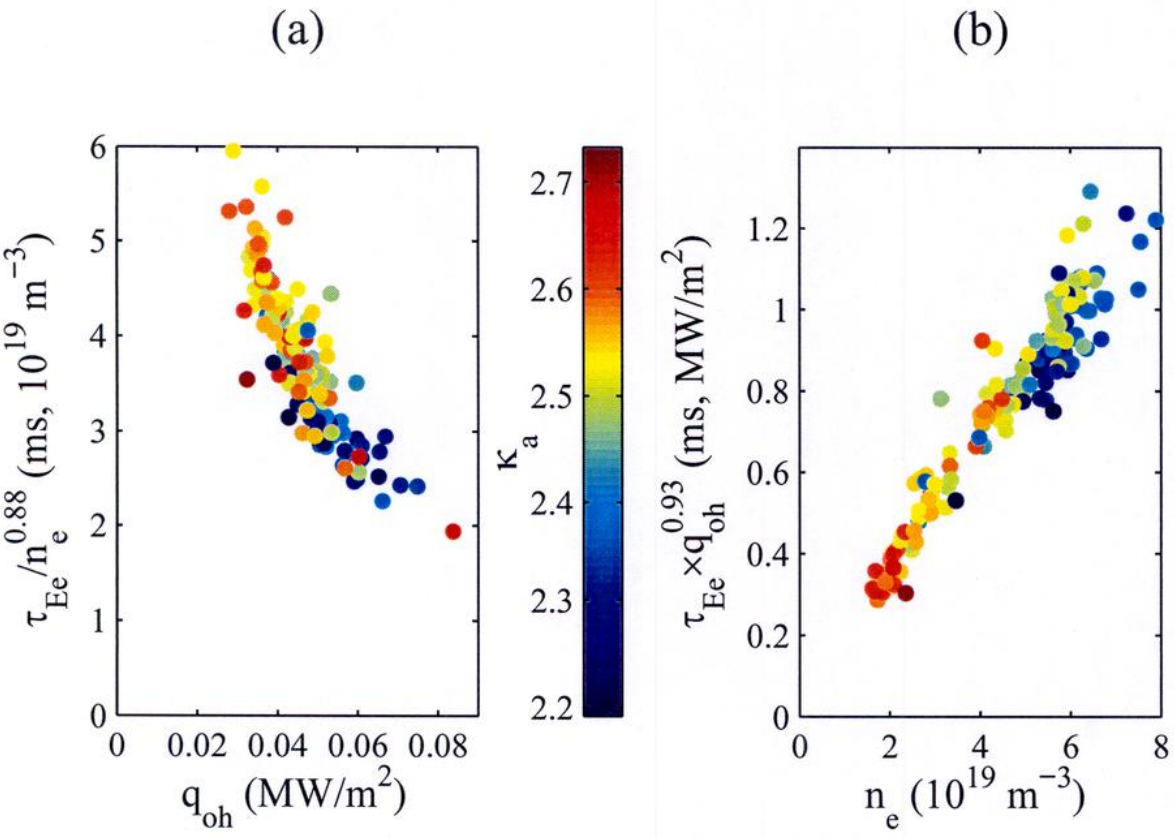
(a)
(b)
$\tau_{Ee}/n_e^{0.88}$ (ms, 10^{19} m^{-3})
q_{oh} (MW/m^2)
κ_a
$\tau_{Ee} \times q_{oh}^{0.93}$ (ms, MW/m^2)
n_e (10^{19} m^{-3})

Fig. 8

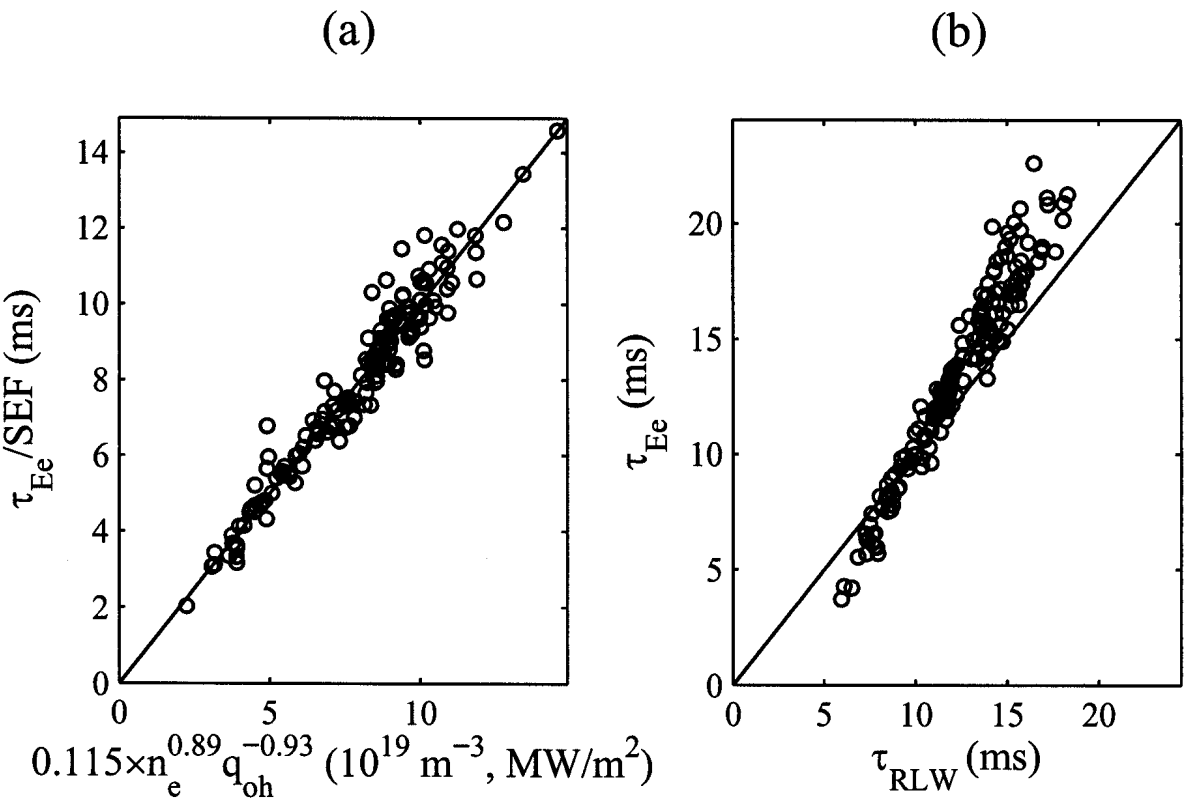
(a)
(b)
τ_{Ee}/SEF (ms)
$0.115 \times n_e^{0.89} q_{oh}^{-0.93}$ (10^{19} m^{-3}, MW/m^2)
τ_{Ee} (ms)
τ_{RLW} (ms)
0
2
4
6
8
10
12
14
5
15
20

Fig. 9

(a) (b)

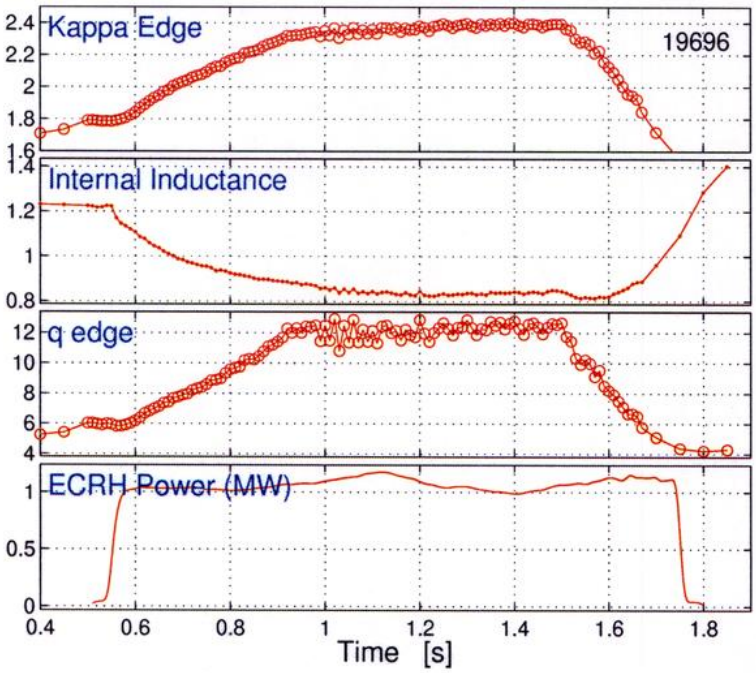
Kappa Edge
19696
Internal Inductance
q edge
ECRH Power (MW)
Time [s]

Fig. 10

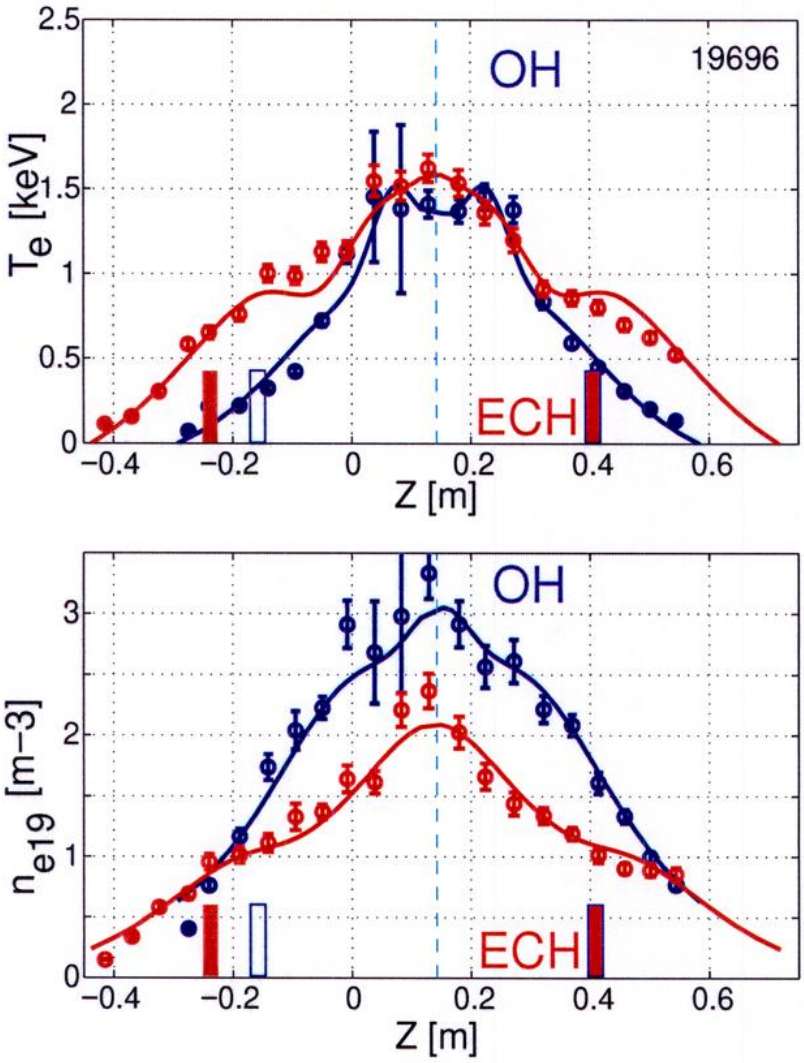

Fig. 11

CHARACTERISATION OF ION-TEMPERATURE-GRADIENT-DRIVEN (ITG) MODES IN THE W VII-X STELLARATOR CONFIGURATION

S. Allfrey, A. Bottino, R. Hatzky[1], G. Jost, L. Villard

Centre de Recherches en Physique des Plasmas, Association Euratom-Confédération Suisse, Ecole Polytechnique Fédérale de Lausanne, 1015 Lausanne, Switzerland

[1] *Max-Planck-Institut für Plasmaphysik, Teilinstitut Greifswald, D-17491 Greifswald, Germany*

1 Introduction

Micro-instabilities, ion acoustic (drift) waves, destabilized by spatial inhomogeneities, are commonly held responsible for anomalous transport in tokamaks. Optimized stellarator configurations such as W VII-X [1] should reduce neo-classical transport to a level close to that found in tokamaks. At this point anomalous transport properties may become dominant. Thus it is now necessary to develop tools for the study of drift wave turbulence in three dimensional geometries. In this article we present results from both linear and non-linear Particle-In-Cell, global, gyrokinetic simulations, the former in the full 3-D geometry, the latter in an appropriate system of reduced dimensionality.

2 Linear simulation

The 3D global PIC code, EUTERPE [2][3] uses a low beta approximation within the linear gyrokinetic model with electrons assumed adiabatic. Thus the perturbed ion distribution function obeys,

$$\frac{d}{dt}f(\vec{R},v_{||},\mu,t) = -\frac{\langle\vec{E}\rangle\times\vec{B}}{B^2}\frac{\partial f_0}{\partial\vec{R}} - \frac{q_i}{m_i}\vec{h}\cdot\langle\vec{E}\rangle\frac{\partial f_0}{\partial v_{||}} - \left(v_{||}\frac{\partial f_0}{\partial v_{||}} + \frac{1}{2}v_\perp\frac{\partial f_0}{\partial v_\perp}\right)\langle\vec{E}\rangle\cdot\vec{h}\times\frac{\vec{\nabla}B}{B^2}. \quad (1)$$

The equations for the particle guiding centers are,

$$\frac{d\vec{R}}{dt} = v_{||}\vec{h} + \frac{v_{||}^2 + v_\perp^2/2}{\Omega}\vec{h}\times\frac{\vec{\nabla}B}{B}, \qquad \frac{dv_{||}}{dt} = \frac{1}{2}v_\perp^2\vec{\nabla}\cdot\vec{h}, \qquad \frac{d\mu}{dt} = 0. \quad (2)$$

And the system of equation is closed by invoking quasi-neutrality,

$$\frac{en_0}{T_e}\phi - \vec{\nabla}_\perp\cdot\left[\frac{n_0}{B\Omega}\vec{\nabla}_\perp\phi\right] = \int f(\vec{R},v_{||},v_\perp,t)\delta^3(\vec{R}-\vec{x}-\vec{\rho})Bd\vec{R}d\alpha dv_{||}d\mu \quad (3)$$

This Poisson equation is solved in the PEST-1 (s,θ^*,φ) system of coordinates using a finite element method. As a matter of noise reduction, the right hand side of equation 3 is Fourier filtered in (θ^*,φ). EUTERPE has been successfully benchmarked against the helical version of the GYGLES code [5].

The goal of the linear simulations was an understanding of the coupling behavior of the ITG mode in W VII-X. Typically the magnetic geometry of a confinement system may lead to couplings between Fourier harmonics in the periodic coordinates. In a tokamak the predominantly $m = 1$ poloidal variation in $|B|$ leads neighboring poloidal harmonics to couple allowing the ballooning structure to the Toroidal-ITG

mode. Such behavior extends to 3D-geometries [4]. The existence of a given coupling may be determined by choosing our Fourier filter to allow only for this coupling and looking for the growth of a normal mode.

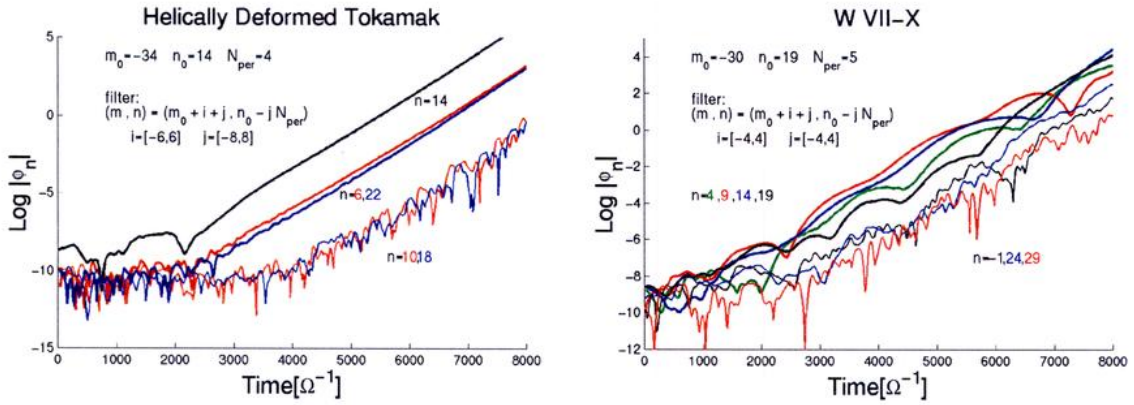

Figure 1: Toroidal harmonics of the perturbed electrostatic potential ϕ_n. The deformed tokamak shows clear mode coupling which is entirely absent for W VII-X.

As an example, shown on the left of figure 1, are results from a tokamak configuration, helically deformed such that the spectrum of $|B|$ is dominated by $B_{m,n_{per}} = B_{1,0}$, $B_{2,2}$ and $B_{1,2}$, here m is the poloidal mode number, $n = n_{per} \times N_{per}$ is the toroidal mode number and N_{per} is the toroidal periodicity of the system. The linear growth of all modes present in the chosen filter shows that we have couplings $(m, n) \rightarrow (m + 1, n)$, $(m, n) \rightarrow (m + 2, n - 2 \times N_{per},)$ and $(m, n) \rightarrow (m + 1, n - 2 \times N_{per},)$ as could be expected from the $|B|$ spectrum by analogy to the case of the tokamak.

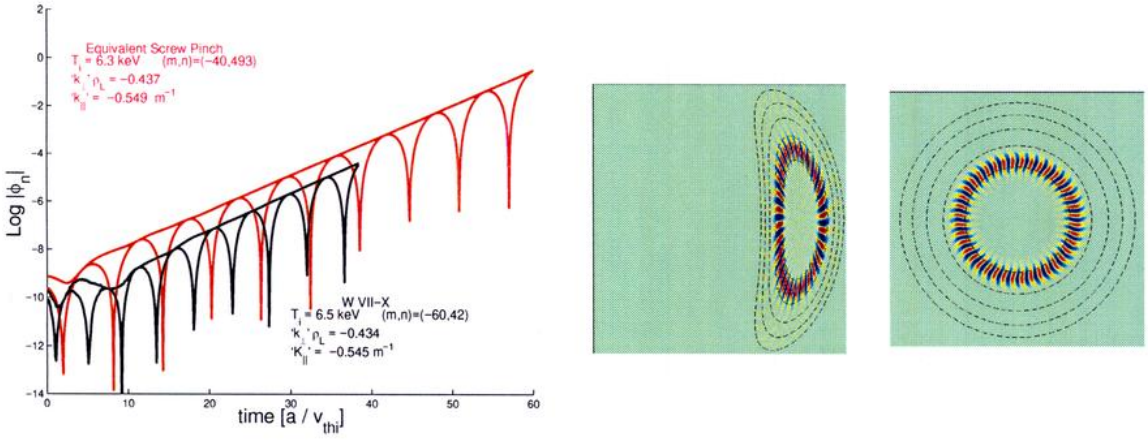

Figure 2: Comparison of growth rates and poloidal mode structures for W VII-X and the 'equivalent' screw pinch. W VII-X: $\gamma = 0.1529[v_{thi}/a]$, $\omega = 0.6804$ screw pinch: $\gamma = 0.1473, \omega = 0.5283$.

In contrast, application of a number of different filter shapes, based on the dominant components of $|B|$, to the W VII-X configuration could find no evidence of coupled

modes. This led to the conclusion that here ITG modes would be 'slab' like, consisting of a single (m, n) harmonic. This observation motivated comparison with a straight screw-pinch configuration. This 'equivalent' straight system was constructed by keeping the connection length ($\frac{1}{R_0 q}$) and profile shapes unchanged. This comparison, shown in figure 2, found agreement in growth-rates to within 5% and similar mode structures, which in both cases simply conformed to the geometry of the magnetic surfaces.

3 Non-Linear simulation

We have shown that ITG modes in W VII-X have a slab like character which indeed may be well approximated by an equivalent screw-pinch equilibrium. As a first approach to it's non-linear simulation we further approximate the geometry to that of a straight Θ-pinch, still allowing for such slab modes. We make this approximation with the goal of achieving energy conservation in non-linear drift wave turbulence simulation.

The TORB [6] code has been adapted from the toroidal non-linear, global, gyrokinetic, δf PIC code ORB [7]. As with the linear code, electrons are treated as adiabatic. The markers are advanced using a 4^{th} order Runga Kutta scheme. Cubic splines are used for the finite element resolution of the Poisson equation. The charge density is Fourier filtered in the periodic coordinates. This filtering process has been shown to be energy conserving [8].

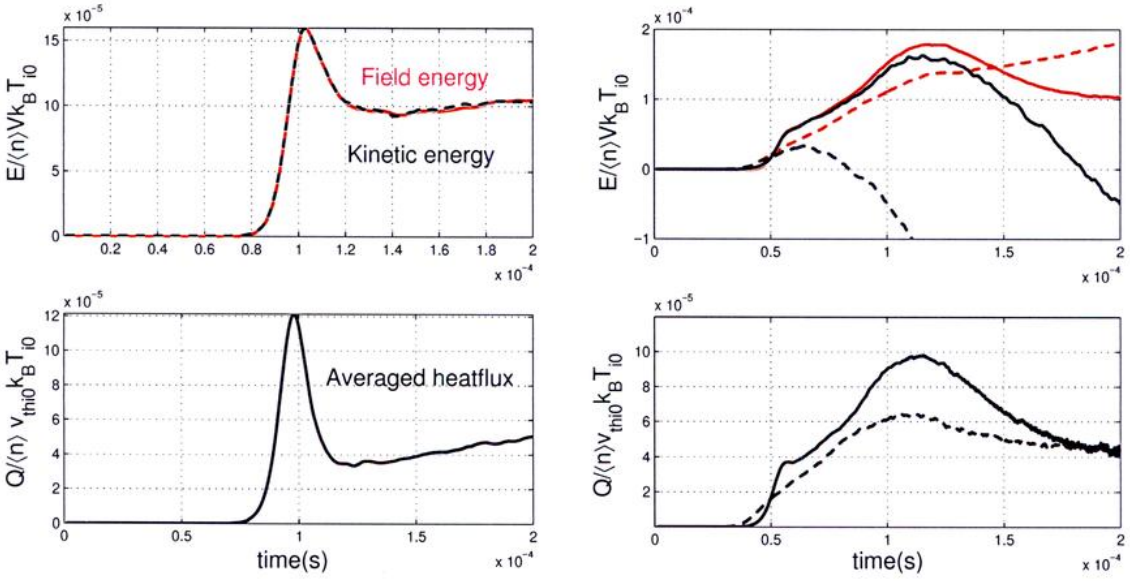

Figure 3: Conservation of energy and heat flux. Left 67 million tracers, filter $m = -24 : 24$ $n = 0 : 6$, optimized loading. Right 16 million tracers, filter $m = -96 : 96$ $n = 0 : 6$, solid: optimized loading, dashed: no loading optimization.

The most unstable linear modes for the equilibrium we consider are $(m, n) = (24, 1); (45, 2); (48, 3)$. Results using a filter retaining harmonics up to the fastest growing $n = 1$ mode (left of figure 3) show very good energy conservation well past the initial saturation phase.

TORB makes use of an intelligent initial loading of markers in velocity and configuration space. A well chosen initial loading has been found to be of great assistance in improving energy conservation. This is shown on the right of figure 3, for two simulations using a filter containing all the dominant linear modes, with and without intelligent loading. Conservation comparable to that shown for the restricted filter sill requires > 120 million tracers [8].

4 Conclusions and further work

Linear simulation has shown W VII-X to be well approximated by a straight screw pinch with respect to pure ITG instabilities. The EUTERPE code should be extended to include electron physics and the effects investigated.

Non-linear simulations of a Θ-pinch approximation to W VII-X have shown good energy conserving properties. The code is now being adapted for the screw-pinch configuration suggested by linear results. Recently, correct treatment of the electron response to the field line average electrostatic potential has been implemented in TORB. This will allow consistent inclusion of the effects of zonal flows, corresponding to the $(m, n) = (0, 0)$ component of the perturbed electrostatic potential.

Acknowledgment This work was partly supported by the Swiss National Science Foundation.

References

[1] J. Nürhenberg *et al.*, Trans. Fusion Tech. 27, 71 (1995).

[2] G. Jost, T. M. Tran, W. A. Cooper, L. Villard and K. Appert, to be published Phys. Plasmas, July 2001.

[3] G. Jost, T. M. Tran, K. Appert, S. Allfrey, W. A. Cooper and L. Villard, submitted to Computer Physics Communications 2001.

[4] G.Jost *et al.*, *Theory of Fusion Plasmas* (Proc. Int. Workshop, Varenna, 2000). Editrice Compositori, Società Italiana di Fisica, Bologna, 2001.

[5] M. Fivaz, S. Brunner, G. de Ridder, O. Sauter, T. M. Tran, J. Vaclavik, L. Villard and K. Appert, Comp. Phys. Communications, 111 1998 p27.

[6] R. Hatzky, T. M. Tran, A. Könies, R. Kleiber, *Theory of fusion plasmas: Proceedings of the Joint Varenna-Lausanne International Workshop, 2000*, edited by J. W. Connor, O. Sauter and E. Sindoni (Editrice Compositori, Bologna, 2000) p407.

[7] T. M. Tran, K. Appert, M. Fivaz, G. Jost, J. Vlaclavik and L. Villard, *Theory of fusion plasmas: Proceedings of the Joint Varenna-Lausanne International Workshop, 1998*, edited by J. W. Connor, E. Sindoni and J. Vaclavik (Editrice Compositori, Bologna, 1999) p45.

[8] R. Hatzky, T. M. Tran, A. Könies, R. Kleiber and S. Allfrey, to be published 2001.

Improved Core Electron Energy Confinement in TCV Tokamak Plasmas with Central EC Counter Current Drive

R. Behn, Z.A. Pietrzyk*, C. Angioni, S. Coda, T.P. Goodman, M.A. Henderson, F. Hofmann, J. Mlynar, O.Sauter, A. Scarabosio, H. Weisen and the TCV team

Centre de Recherches en Physique des Plasmas
Association EURATOM-Confédération Suisse
Ecole Polytechnique Fédérale de Lausanne, Switzerland
**) present address : Redmond Plasma Physics Laboratory, University of Washington, USA*

A quasi stationary regime of improved core electron energy confinement (ICEC) has been identified in the TCV tokamak. It has been obtained under conditions of dominant electron heating using cyclotron waves at the second harmonic (82.3GHz for TCV) and is characterized by core electron temperatures near and above 10 keV and global electron energy confinement times 3 to 4 times higher than those predicted by the RLW scaling law [1,2]. The heating scenario comprises two phases separated by a time delay of about 300ms : a so-called pre-heating phase with off-axis power deposition and a high performance phase during which additional power is injected into the centre in counter current drive (CNTR-ECCD) orientation with a toroidal component of the beam launching angle of about 30 degrees. For the experiments described here, power levels of 0.9 to 1.35MW were used for preheating at a normalized radius of $\rho \sim 0.3$, whereas up to 0.9MW were injected for central counter ECCD. The target plasma, in limiter configuration, is described by the following parameters : $\langle n_e \rangle = 1.5\ 10^{19}\ m^{-3}$, $I_p = 200kA$, $\kappa \sim 1.7$, $q(a) \geq 7$.

Fig.1
Combined EC heating and current drive, Profiles from top to bottom : power density, integrated power, density of EC diven current, integrated EC-driven current,

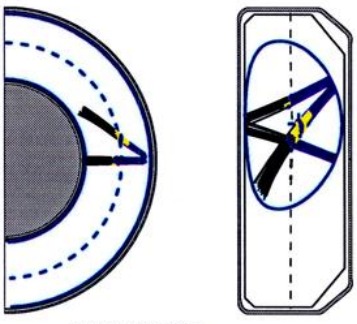

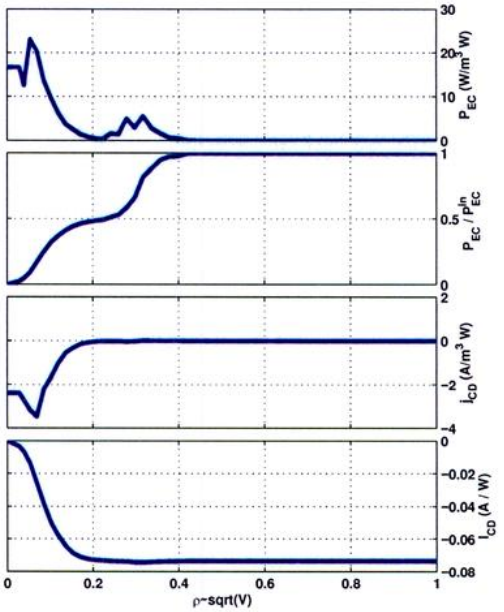

The particular configuration with 4 gyrotron beams launched from different ports, is explained by fig. 1. It shows results of ray tracing using the TORAY code [3], which also calculates the amount of EC-driven current. As will be discussed later, the exact location for both off-axis and central power deposition are important and have to be optimized to achieve a quasi-stationary phase of improved performance.

Figs. 2 and 3 show T_e and n_e profiles measured by Thomson scattering during the 3 different phases (ohmic, pre-heat, combined ECH & ECCD) of a shot which entered the ICEC regime after 0.7s. During this phase the T_e profiles are strongly peaked (peaking factor of 6 to 8) and the appearance of sharp gradients suggests a spatial variation of the transport parameters (transport barrier). The zone with the largest gradients lies clearly inside the q=2 surface. The electron density profiles show rather little change, apart from a tendency towards slightly hollow shapes during the high temperature phase, an effect which is known as particle pump-out.

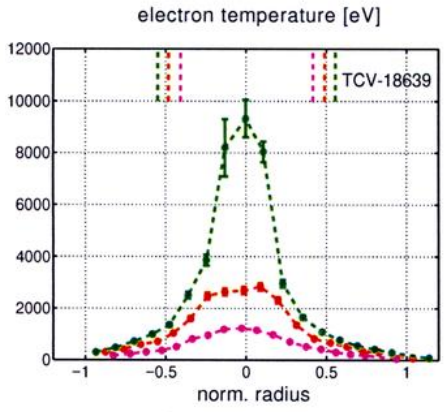

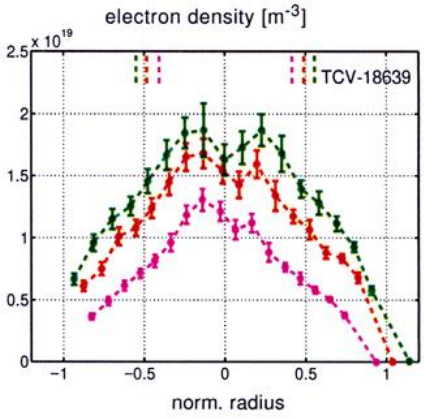

Figs 2 & 3
T_e and n_e profiles from Thomson scattering
magenta (bottom) : ohmic phase
red (middle) : pre-heat phase
green (top) : combined off-axis ECH & central CNTR-CD
markers at the top: location of q=2 surface

The time evolution of the central electron temperature is presented in fig.4 for 3 cases, 2 referring to the combined ECH-counter-CD scenario, which leads to the ICEC regime, and a reference case for which central CNTR-CD was replaced by heating only. The ICEC cases are characterized by a central T_e , which is about a factor of 2 above that of a standard EC-heated plasma at the same input power level. The increase in the energy confinement, expressed by the H-factor (referring to RLW scaling) reaches values between 3 and 4. This enhancement is explained by the formation of a core region with reduced transport and is the consequence of modifications in the current density profile due to off-axis heating and central counter CD. This conclusion has been based on numerical simulations using the PRETOR code. With the local EC power density and driven current as input, PRETOR is capable of reproducing the experimentally observed temperature profiles during all phases of a shot [4]. The calculated spatial variation of the heat diffusision coefficient χ_e (fig. 6) is in good agreement with the experimental data and clearly shows a reduction of core transport to or even below the level in the ohmic phase.

Since PRETOR is coupled to an equilibrium solver, it can also consistently calculate the profiles of the current density and safety factor which in this case is characterized by reversed shear in the centre (fig. 7).

Fig. 4

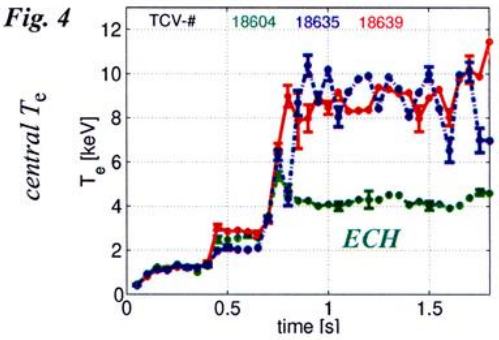

Fig. 5

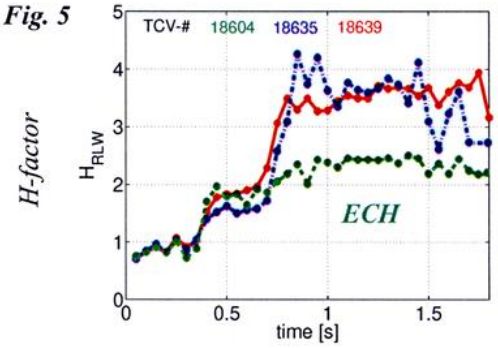

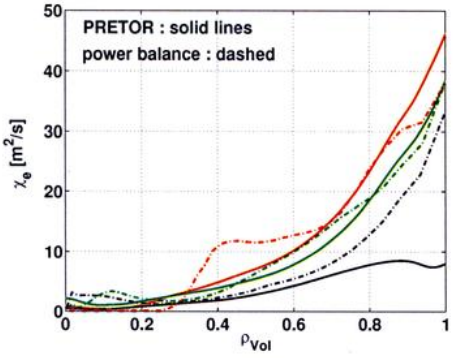

Fig. 6 *χ_e-profiles from experimental data & PRETOR*
black : ohmic
red : pre-heat phase (off-axis ECH)
green : combined ECH & CNTR-CD

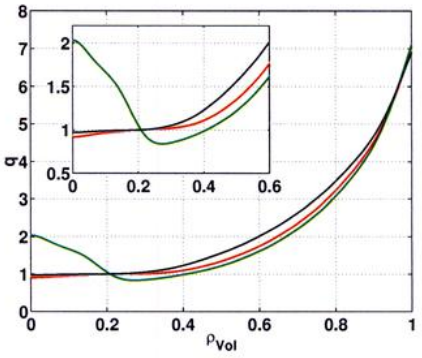

Fig. 7 *safety factor profile from PRETOR*
black : ohmic
read : pre-heat (off-axis ECH)
green : combined ECH & CNTR-CD

High central electron temperatures of 10 keV and above have already been observed during earlier experiments on TCV using only central power deposition in counter current drive orientation [5]. However, it has been found that in all of these cases the appearance of MHD activity leads to a sudden collapse reducing both electron temperature and energy confinement time. Fig. 8 gives an example comparing the temperature evolutions for a typical ICEC shot (TCV-# 19421, red trace) and a shot without off-axis heating (TCV-# 19420, blue trace). In both cases central counter CD was applied during the time interval from 0.7 to 1.8 s.

Fig. 8
Variation of central T_e (from Thomson scattering) for different heating scenarios
red : combined off-axis ECH & central CNTR-CD
blue : central CNTR-CD only

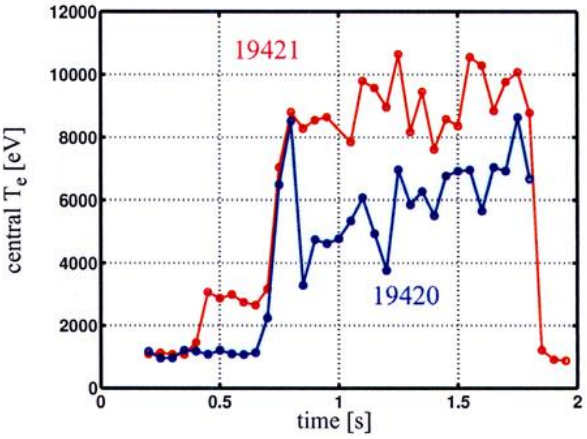

The development of strong m=2 mode activitity after 0.8s for shot 19420, is clearly visible in the signals of magnetic probes and in the soft X-ray emissivity (fig.10). The mode structure has been identified by SVD analysis. Further investigations have revealed that the amplitude of these modes increases gradually with increasing ratio of central to off-axis power deposition. As illustrated by the results of shot 19421, the mode activity is suppressed by balanced off-axis heating before and during central power deposition. Therefore, stabilisation of these modes appears to be a prerequisite for a quasi-stationary phase of improved confinement.

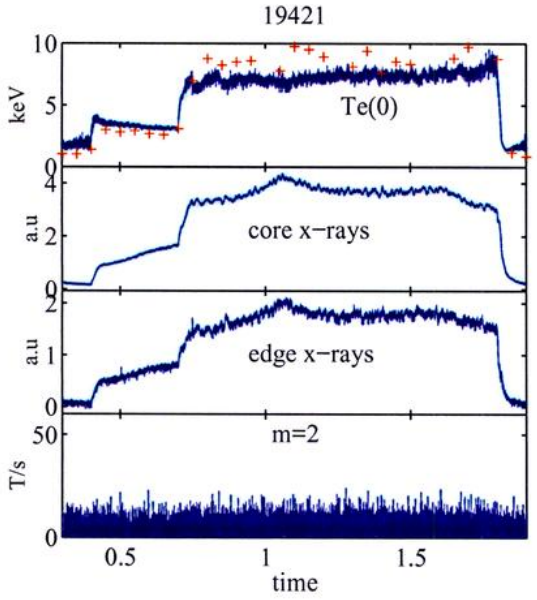

Fig. 9
Combined off-axis EC & CNTR-ECCD in the centre :

Small amplitude relaxation oscillations
traces top to bottom :
T_e from soft X-ray emissivity
red crosses : $T_e(0)$ from Thomson scattering
X-ray emissivity along 2 different chords
signal from magnetic probe

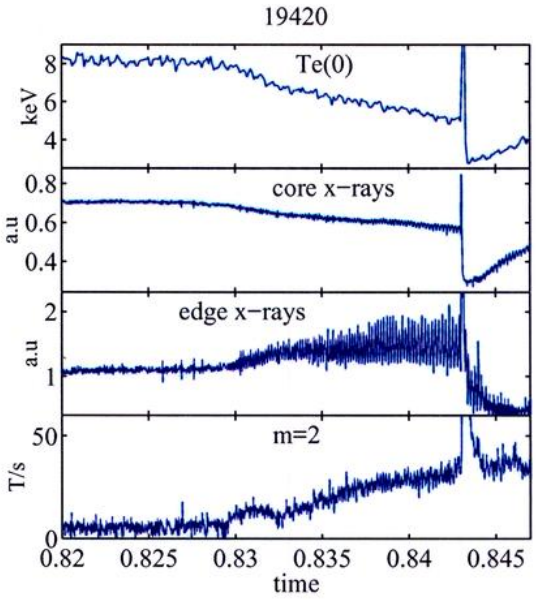

Fig. 10
Central counter ECCD only :

Growing m=2 mode followed by major relaxation event

Another important factor in the optimisation of the ICEC scenario is the exact orientation of the beams for central counter CD. Results from a series of experiments, during which the orientation of the 2 beams used for central counter-ECCD has been varied by a small amount (a few degrees in the poloidal launching angle), are presented in the following figures. This study was made possible by the flexibility of the beam launching system installed on TCV, which permits exact and reproducible control of the poloidal and toroidal launching angles. Fig. 11 shows profiles of the EC power density (from TORAY) and fig. 12&13 the effect on the central electron temperature and energy.

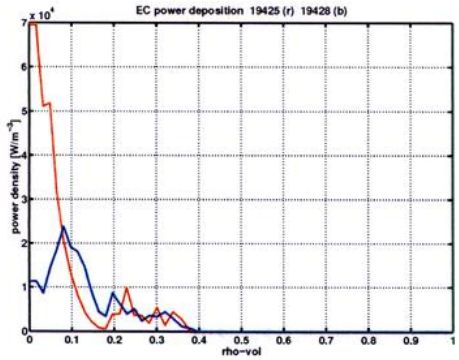

Fig 11 *Profiles of EC power deposition as obtained from TORAY*
blue : TCV-# 19428, off-centre
red : TCV-# 19425, optimized for central power deposition

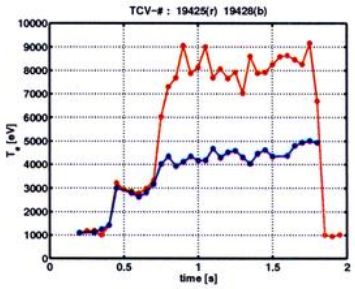

Fig. 12
Central T_e
blue : TCV-# 19428
red : TCV-# 19425

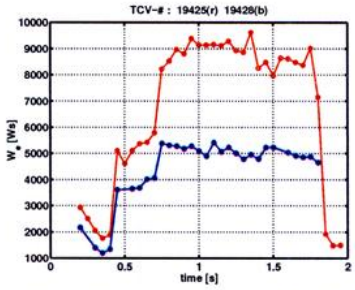

Fig. 13
Electron energy content
blue : TCV-# 19428
red : TCV-# 19425

These cases have also been analyzed using the PRETOR code. A substantial reduction in transport and a transition to improved confinement has only been found for central power deposition. The ratio in the global electron energy confinement times is close to 2. Taking the EC-driven current density as given by TORAY and assuming spatial uniform Z_{eff} and E_{ll}, the various contributions to the total steady-state current profile has been calculated. The results are given in figs. 14 &15 showing that already a small deviation from central power deposition prevents the formation of a current profile with a central minimum and reversed shear.

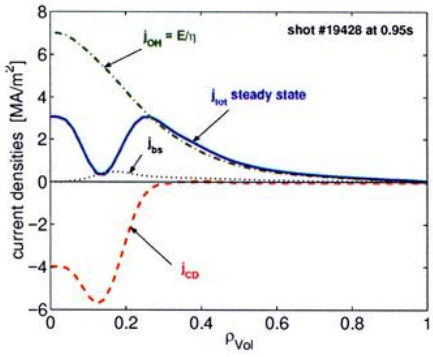

Fig. 14 *(left) contributions to j(ρ) for de-centered counter-ECCD*

Fig.15 *(right) same, but for optimized central counter ECCD*

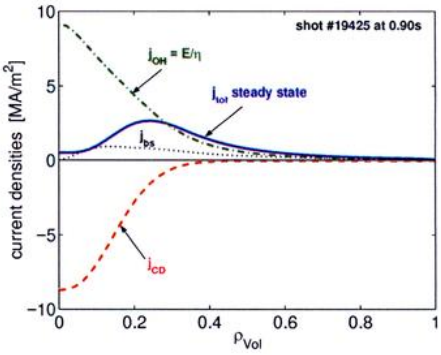

This confirms conclusions of earlier studies concerning the ICEC regime, namely : off-axis power deposition already during a preheating phase is beneficial for stabilisation of MHD activity; precise adjustment of the central ECCD component is essential to obtain reversed shear, which appears to be the key to improved electron energy confinement in the core region.

This work was partially supported by the Swiss National Science Foundation.

[1] *Z.A. Pietrzyk et al. Phys.Rev.Lett. 86 (8), 1530-1533, 2001*
[2] *Z.A. Pietrzyk et al. Phys. Plasmas, 7 (7), 2909-2914, 2000*
[3] *A.H. Kritz et al. Symp. on Heating in Toroidal Plasmas, 1982, Proc. vol.II, p.707*
[4] *C. Angioni et al. Theory of Fusion Plasmas, Varenna, 2000, (ed. compositori, Bologna)*
[5] *R. Behn et al. Proc. 26th EPS Conf. on Contr. Fusion & Plasma Physics, Maastricht, 1999*

Measurements of Electron Cyclotron Emission From Non-Maxwellian Electron Distributions in TCV Plasmas With ECH and ECCD

P. Blanchard, H.Weisen, S.Alberti, S.Coda, P.Gomez, T.Goodman

Centre de Recherches en Physique des Plasmas, Association EURATOM - Confédération Suisse, EPFL, CH-1015 Lausanne, Switzerland

e-mail adress of main author: Patrick.Blanchard@epfl.ch

Abstract: Electron Cyclotron Emission (ECE) measurements from the high field side (HFS) of the TCV tokamak have been obtained from plasmas heated by second and third harmonic X-mode ECH and ECCD. Suprathermal ECE is detected in the presence of X2 ECCD and of X3 ECH. The ECE temperature increases sharply with the toroidal launch angle of the X2 EC power with a maximum observed at +/- 20°. The results are modelled using the bi-Maxwellian approximation.

Introduction

The TCV tokamak (R=0.88 m, a<0.24 m, B_T<1.54 T, Ip<1.2 MA) is equipped with six 0.5 MW gyrotrons at the second electron cyclotron harmonic and three 0.5 MW gyrotrons at the third harmonic. Essential information on the behaviour of suprathermal electrons and wave absorption physics can be obtained by a High Field Side (HFS) ECE measurement. Suprathermal electrons are produced in many experimental conditions, in particular with X2 ECCD and X3-ECH[1] . Since June 2000, the TCV Tokamak is equipped with a X-mode ECE radiometer with antennae placed at the HFS of the vessel. This configuration give access to the relativistically downshifted ECE, since it is not reabsorbed by the thermal population, as it is with Low Field Side observation.

Experimental setup

The ECE radiometer used in the TCV tokamak is a X-mode 24 channel super-heterodyne radiometer. It covers the frequency range from 78.5GHz to 114.5GHz, corresponding to the second harmonic of the electron cyclotron frequency at the HFS. It features a choice of two horizontal lines of sight perpendicular to the magnetic field, placed at Z=0m and Z=0.21m. The frequency bandwidth of each channel is 750 kHz, corresponding to a spatial resolution between 0.4 (edge) and 1 cm (center) for the cold resonance. The signals are acquired at a frequency of 100 kHz. The radiometer is cross calibrated from Thomson scattering measurements during the ohmic phase of the discharge, prior to ECH and ECCD.

The flexibility of the EC heating system allows both the toroidal and the poloidal injection angles to be adjusted[1]. The target plasmas used in the experiments reported here have the following parameters: I_p=200kA, q_{95}=3.8, κ=1.31,δ=0.16, B_T = 1.42T, $n_e(0)=2.5\times10^{19}m^{-3}$. All the plasmas have an ohmic phase of about 0.3s followed by a X2 'preheating' phase with constant

power (P_{X2}=0.47 MW) from 0.3s to 1.3s, whereas the X3 power is applied from 0.5s to 1.2s. The X3 power (P_{X3}=0.47 MW) and the launching angles (ECH heating) are kept constant, whereas the toroidal and poloidal launching angles of the X2 ECH/ECCD are varied.

EC emission and absorption

For typical densities and temperatures of TCV ($n_e(0)$~2.5x10^{19}m^{-3},$T_e(0)$~2keV), the plasma is optically thick (the bulk optical depth $\tau_b>10$) and the ECE radiometer provides a measurement of the electron temperature profile if the distribution function is Maxwellian. The ECE from suprathermals is frequency-downshifted by the relativistic factor γ (γ=1.05 @ 10 keV). If the radiation is observed from the HFS, this downshifted radiation does not pass through the EC cold resonance and is unaffected by the bulk absorption. At any given observation frequency, the intensity of the EC radiation is then the result of a sequence of emission and absorption by electrons from different populations, occurring in different plasma regions. We may define the radiative temperature T_r by[2]

$$I_\omega = \frac{\omega^2}{8\pi^3 c^2} T_r \left(1 - e^{-\tau_0}\right) \quad (1)$$

where I_ω is the intensity of the EC radiation at the frequency ω and τ_0 is the total optical depth. For a Maxwellian plasma, T_r=T_e. Under the assumption of a bi-Maxwellian (bulk+suprathermal) distribution, an expression for the local intensity can be obtained as[2]:

$$I_\omega = \frac{\omega^2}{8\pi^3 c^2}\left[T_b\left(1 - e^{-\tau_b}\right)e^{-\tau_s} + T_s\left(1 - e^{-\tau_s}\right)\right] \quad (2)$$

with T_b and T_s the bulk and suprathermal temperature, τ_b and τ_s the respective optical depth. If $\exp(-\tau_s)$<<1, the plasma radiates like a blackbody at the suprathermal temperature. We will refer to the directly measurable quantity $T_{ece}=8\pi^3c^2I_\omega/\omega^2$ as the (apparent) ECE temperature.

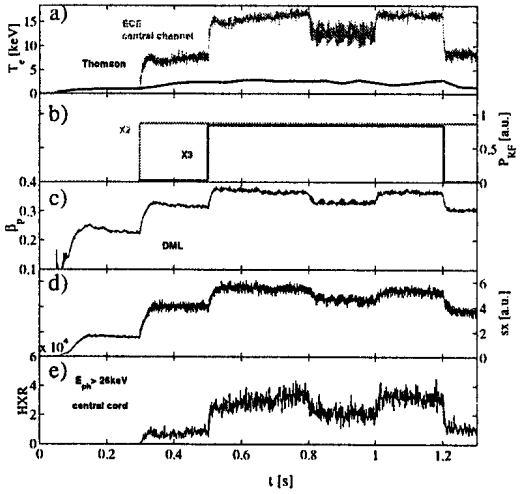

Fig.1 Suprathermal emission with X2 ECCD and X3 ECH. a) central channel of the ECE (red) and central Thomson temperatures, b) RF power for X2 (CO-ECCD 20°) and X3 ECH, c) poloidal beta, d) soft x-ray signal (central chord), e)hard x-ray signal (central chord).

EC emission on TCV

Typical ECE results for combined X2 ECCD and X3 ECH are shown in Fig.1a. The traces show the temporal evolution of the ECE temperature from the central channel (ρ_ψ=0.1) of the ECE radiometer as well as the electron temperature from Thomson scattering. X2 power is injected in CO-ECCD (toroidal launching angle +20°) whereas X3 is in ECH (Fig.1b). With ECCD only (from 0.3 to 0.5s) the ECE temperature exceeds the

electron temperature by a factor of three. The X3 heating phase starts at 0.5s and features a period of power modulation (0.8-1s) during which an absorption measurement was obtained using a fast response diamagnetic loop (DML), which showed that in this discharge all of the X3 ECH power was absorbed (fig1.c[5]). With X3 ECH, T_{ece} increases by a factor of two, demonstrating that the X3 power is absorbed by the suprathermals generated by X2 ECCD. This interpretation is corroborated by results from a hard X-ray camera[4], which shows a strong increase of suprathermal X-ray emission with combined X2 ECCD and X3 ECH (fig.1e), while the thermal soft X-ray emission only increases moderately (fig.1d). The sensitivity of the ECE on the injection angles of the EC power is shown in Fig.2. In this experiment the plasma was heated with X2 ECH for 50ms before the X3 ECH was added at 0.4s and after X3 switched-off at 1.2s. During the X2 ECH only phases the ECE temperature profile agrees with the profile from Thomson scattering, demonstrating that no suprathermals are generated. The addition of central X3 ECH produces suprathermals, although T_{ece} is lower than with X2 ECCD. The DML measurement during the modulated phase (0.5-0.7s) of this shot shows that only 30% of the X3 power is absorbed. A poloidal scan of the X3 launching angle is then performed from 0.8s to 1.15s from the center to r/a=0.7. All the ECE channels show the same behaviour, including those corresponding to the X3 cold resonance. The emission is maximum at 0.8s when X2 and X3 power are deposited on the same, near central, flux surfaces and then decreases until the X3 deposition is near r/a=0.3. At the same time the hard X-ray emission is strongly reduced and the bulk temperature measured by Thomson scattering diminishes by 30%, also demonstrating reduced X3 absorption. Due to the particular geometry, the X3 EC beam is reflected from the inner wall tiles and returns to the plasma core when the first pass resonance is beyond r/a=0.3. This explains why the T_{ece} and T_e increase again for t>0.9 on Fig.2.

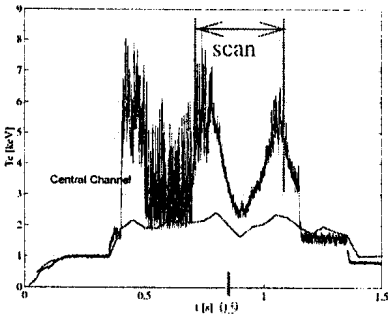

Fig.2 Temporal evolution of the central channel of the ECE (blue) with a X2 ECH preheating followed by a X3 central ECH. Between 0.8s and 1.15s a poloidal scan of the X3 launcher is done. The red line is the central Thomson temperature

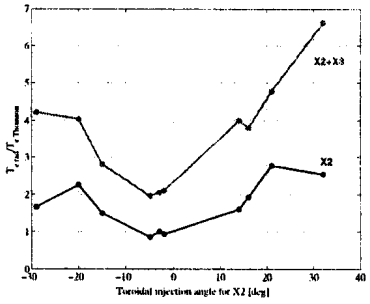

Fig.3: Central temperature comparison for a toroidal preheating X2 injection scan. The blue line is the ratio of the ECE temperature @ρ=0.1 and central Thomson temperature during the X2 phase of the shot. The red line is the same ratio during the X2+X3 phase.

The dependence of the ECE on the toroidal launching angle of the X2 power is shown in Fig.3. Typical bulk temperatures in this shot-to-shot scan are 2keV with X2 only and 2.5keV with combined X2/X3 heating. The ECE temperature is highest for X2 injection angles of +/- 20° with X2 heating only. During the combined heating phase the radiative temperature increases with the injection angle up to at least 33°. These observations are consistent with hard X-ray measurements, which show that the hard X intensity is highest for X2 ECCD or counter ECCD at 20° launching angle.

Interpretation

The bi-maxwellian approximation (eq.2) is used to get a rough idea of the suprathermal population by adjusting n_s and T_s such as to reproduce the observed emission. Fig. 4 shows the result of the calculation (blue curve) for a shot with +15° of X2 preheating plus X3 ECH, $T_e(0)$=3.3keV, $n_e(0)$=2.5e19m^{-3}, together with the measured apparent ECE temperature profile and the temperature profile from Thomson scattering. A suprathermal temperature T_s=7.4T_e and corresponding density n_s=0.01n_e were assumed over the interval R=[0.76-0.89]. The resulting calculated temperature is very close to the experimental result. The calculated profiles depend sensitively on the shape of T_s and n_s profiles and of the value of $T_s(0)$. A similar agreement can be nevertheless obtained by assuming suprathermal temperatures up to 20% higher (lower) if the corresponding densities are assumed to be 30% lower (higher).

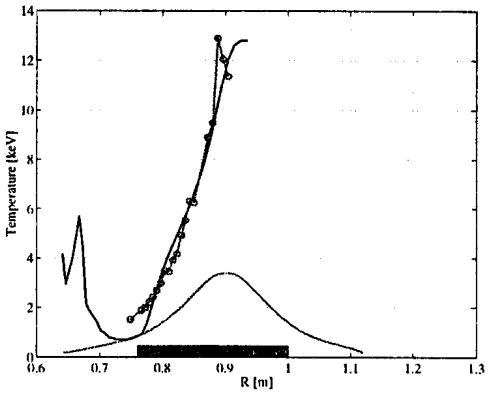

Figure 4: Modelling of the ECE profile.
Green line: Thomson Scattering temperature, red line: ECE temperature, blue line: Calculation with a bi-maxwellian distribution function with Ts/Tb=7.4 and ns/nb=1%.

The suprathermal optical depth for X2, which is proportional to the product n_sT_s of the suprathermal population, can be significant. For the example shown τ_s~1.1 (for $n_s(0)$=2.5e17m^{-3} and $T_s(0)$=25keV) and hence the local radiation temperature is larger than the measured ECE temperature, in closer agreement with the hard X-ray photon temperature (T_{hx}=20keV).

The experimental results clearly show non-thermal EC radiation over a region which is larger than expected from deposition at the cold X3 resonance location. Two factors are likely to produce this effect. With electron energies up to a few tens of keV, the relativistic downshift allows electrons distant by more than 10cm from the cold resonance to be heated. The very presence of such electrons far away from the cold resonance suggest that transport of suprathermals may also be important and may have to be taken into account in Fokker-Planck ECH simulation codes.

Acknowledgments

This work was partly funded by the Swiss National Science Foundation.

References

[1]S. Alberti et al., 18th IAEA Fusion Energy Conference, Sorrento, 2000 IAEA-CN-77/PD/2

[2]R. Bekefi., Radiation Processes in Plasmas John Wiley & Sons New-York 1966

[3]M.Bornatici & F.Engelmann, Phys Plasmas 1 (1994) 189-198

[4]S.Coda et al., This conference, P1.75

[5] A.Manini et al. to be submitted to Plasma Phys. Contr. Fusion

CHARGE EXCHANGE RECOMBINATION SPECTROSCOPY OPTIMISATION WITH THE TCV DIAGNOSTIC NEUTRAL BEAM

P. Bosshard, B.P. Duval, J. Mlynar, H. Weisen
Centre de Recherches en Physique des plasmas
Association EURATOM - Confédération Suisse
Ecole Polytechnique Fédérale de Lausanne, CH-1015 Lausanne EPFL, Switzerland

1. INTRODUCTION

A Diagnostic Neutral Beam Injector (50kV extraction voltage, 0.8A effective current) has been installed on the TCV Tokamak for ion temperature and impurity density profile measurements. Initial measurements of visible carbon CVI($n=8 \rightarrow 7$) transition at λ=5291Å showed that the DNBI signal is only 25% of the measured signal at an average plasma density of $1\text{-}2.10^{19}m^{-3}$ and ~5% at $5.10^{19}m^{-3}$. The passive plasma emissivity profile, measured by inverting a vertical multi-chord view of the plasma, was highly peaked at the plasma edge corresponding to a thermal hydrogen neutral density of $\sim 10^{-4}\text{-}10^{-5}.n_e$. A model used to calculate the DNBI and background emissivity along the diagnostic lines of sight show that in order to obtain an ion temperature measurement from the DNBI, the collection efficiency of the optical system must be increased to improve the photon statistics and the DNBI neutral density in the observation region must be increased by a factor of 3-10.

2. THE TCV DIAGNOSTIC NEUTRAL BEAM INJECTOR [1]

The charge exchange cross-section for carbon is maximum for a 50kV extraction voltage. The effective beam current is ~0.8A, (73% are H_1^+, 20% H_2^+ and 7% H_3^+) and the ~40kW injected power is small compared to the TCV ohmic power (250kW - 1MW). The extraction grid can accept full power for the complete 2s TCV pulse duration. The beam is normally pulsed with a 2 - 100ms duty period. The beam has a divergence of 0.6° and a gaussian cross section with a FWHM of ~7cm at the DNBI ion source focus at the TCV centre. The beam is injected at a toroidal angle of 11.25° to avoid creating trapped particles.

The beam dimensions and alignment were verified inside the TCV vessel by an array of thermocouples on the central column facing the DNBI entrance port. The relative intensities of the Doppler-shifted H_α lines from the beam correspond to the expected DNBI component fractions.

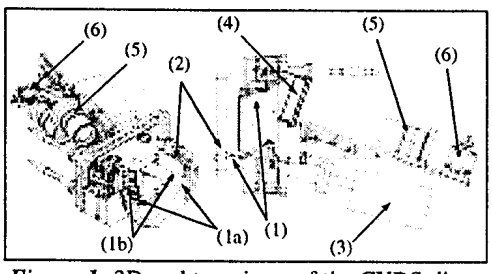

Figure 1: 3D and top views of the CXRS diagnostic head. (1) plane mirrors of the periscope (vacuum side) (1a) plasma bulk system (1b) plasma low-field side edge system (2) shutter (3) shutter movement (4) air-vacuum interface (5) objectives (6) fibre holders.

3. THE CXRS DIAGNOSTIC ON TCV

Direct observation of the DNBI-plasma interaction is not possible with the TCV port geometry. A diagnostic camera head was constructed inside the vacuum chamber composed of two sets of two stainless-steel plane mirrors. Observation of the full (~60cm) DNBI path through the plasma was achieved by using one set to observe the plasma bulk and the other the low field side plasma edge.

The mirror closest to the plasma is used as a shutter to protect the optical surfaces during machine wall boronisation and all mirrors have a BERAL reflection coating, a Be-Al alloy which showed no obvious deterioration after exposure to plasma [2]. Spatial resolution, determined by the viewing chords-flux surfaces intersection at the beam position, is ~1.5cm in the plasma centre and ~3cm at the edge. C/X light from the beam is focused by two F3 aperture lenses onto two bundles of 16 optical fibres with a core diameter of 600μm and a numerical aperture of 0.16. The fibres are placed vertically at the entrance slit of two astigmatically corrected Czerny-Turner spectrometers with a focal length of 0.75m and an aperture of f/8.5 @5300Å. The diffraction gratings have 2400g/mm, giving a spectral dispersion of ~4.65Å/mm at this wavelength. The spectra from the 16 fibres are simultaneously imaged onto a 2D detector equipped with a front-illuminated EEV CCD with 1152x298 square 22.5μm pixels. The minimal readout time for the CCD region which collects the spectra is ~10ms.

4. CXRS MEASUREMENTS

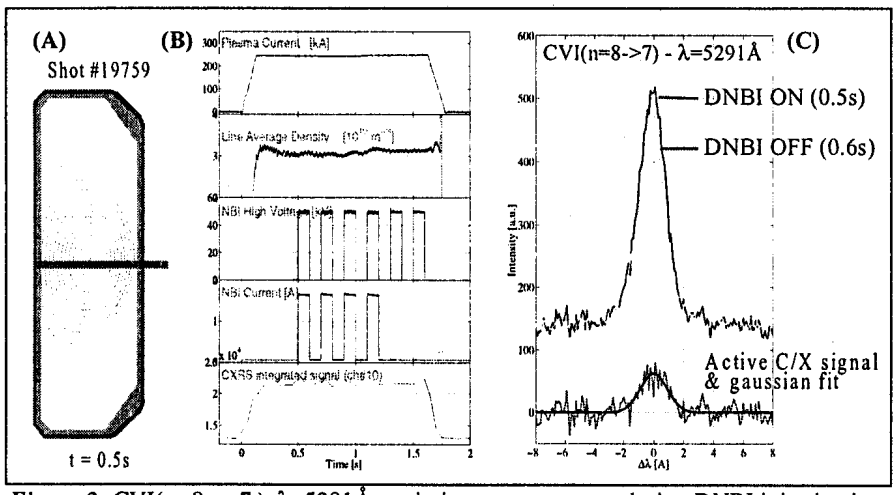

Figure 2: CVI(n=8 → 7), λ=5291Å, emission measurements during DNBI injection into an ohmic low density plasma.**(A)** Plasma poloidal cross section and neutral beam position. **(B)** Time evolution of Ip (250kA), $\bar{n}_e$ ($3.10^{19}m^{-3}$), DNBI accelerating grid high voltage (50kV) and source current (1.7eq-A), wavelength integrated CXRS signal (integrating time: 50ms). The DNBI pulse duration is 50ms and the duty cycle 50%. **(C)** CXRS spectra at 0.5s (DNBI "on" phase) and 0.6 (DNBI "off" phase). The DNBI signal, given by the difference, represents in this case ~10-15% of the measured signal. Estimated ion temperature: 520eV @ρ~0.6.

Fig.2 shows the CVI(n=8 → 7) emission at λ=5291Å detected by the CXRS diagnostic during a low density ($\bar{n}_e$~$3.10^{19}m^{-3}$) ohmic TCV shot with DNBI neutral injection (E_0=50keV/amu, I=1.7eq-A, pulse length: 100ms). DNBI pulses are visible in the time evolution of the wavelength integrated CXRS signal shown in fig.2-(B). The DNBI signal is given by the difference of the signals detected with and without beam injection (integration time: 50ms). In this case, beam C/X intensity is 10-15% of the detected signal (see fig.2-(C)). The ratio between this active signal and the background plasma emission (A/P ratio) is plotted as a function of the average plasma density in fig.3, showing that A/P is limited to ~25% at 1-1.5.$10^{19}m^{-3}$ and decreases to only a few percent at $5.10^{19}m^{-3}$. A/P is similar for the CVI(n=7 → 6) transition at 3433Å despite an effective C/X cross-section which is ~2 times larger than for CVI(n=8 → 7) since

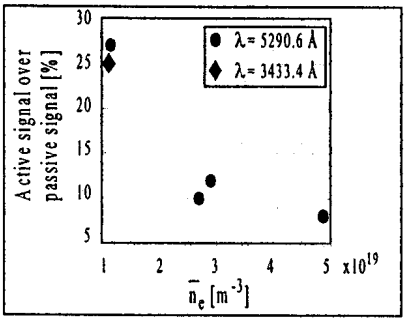

Figure 3: A/P ratio measured as a function of the average plasma density for the carbon transitions CVI(n=8 → 7) at 5291Å and CVI(n=7 → 6) at 3433Å.

the thermal neutral cross sections for these transitions are in the same ratio. For low A/P, measurement of T_i is impeded by the high signal noise (S/N~1.5-2). It has been verified that T_i measurements are dominantly limited by low photon statistics, as shown in fig.5, where the fluctuations of the active C/X signal (λ=5291Å) are compared to the statistical fluctuations, $\sigma_{phot} = \sqrt{2.S_{CXRS}}$, where S_{CXRS} is the intensity (in photons) of the total CXRS signal.

This CXRS diagnostic has two limitations: (1) low active C/X emissivity compared to the plasma background C/X emissivity which can only be improved by increasing the beam neutral density in the observation volume (see section 6). (2) Low photon statistics. The overall efficiency of the CXRS optical system has to be improved to increase the S/N ratio.

5. PLASMA BACKGROUND EMISSIVITY

The emissivity profile of the passive C/X has been estimated by inverting a vertical multi-chord measurement of the background CVI(n=8 → 7) radiation. Fig.4 shows the reconstructed "two-step" profiles for an ohmic plasma (#19479) and a plasma with ECH Counter Current Drive (#19419). The profiles are highly peaked at the plasma edge (ρ≥0.8), where the emissivity is over 20 times higher than in the centre and reaches 20-30% of the DNBI emissivity (~10^{18}m^{-3}s^{-1}). Since C/X cross-section for Δn=1 transitions are much higher than for e^--collision or recombination reactions, this emissivity is ascribed to C/X reactions between fully ionised plasma impurities and thermal neutrals. The estimated thermal neutral density at the plasma edge is of the order of 10^{-5}-10^{-4}.n_e which is comparable with numerical estimations of the Monte-Carlo linear transport code B2-EIRENE [4].

6. DIAGNOSTIC OPTIMISATION

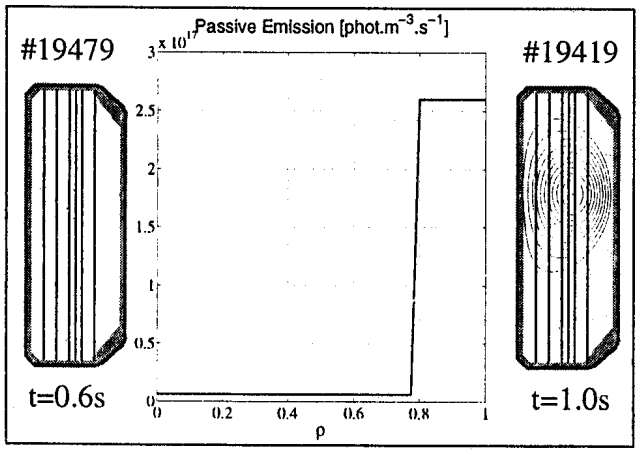

Figure 4: Background emissivity profile (λ=5291Å) estimated by inverting a vertical multi-chord view of the plasma. Shot #19479: standard shot, $\bar{n}_e$~3.5.10^{19}m^{-3}. Shot #19419: ECH Counter Current Drive shot, $\bar{n}_e$~1.5.10^{19}m^{-3}.

Since background emissivity is concentrated at the plasma edge, its contribution to the measured signal cannot be reduced significantly by changing the observation geometry. The active emissivity must be increased by raising the beam neutral density in the beam-spectrometer line-of-sight intersection volume. This may be achieved either by improving the beam focus or increasing the injected current. The plasma emissivity along the spectrometer line of sight has been modelled including the

local plasma density, temperature, background neutral density and beam neutral density, given by a beam attenuation code. The background brilliance was adjusted to match experimental values of A/P and the beam current was modified for reaching A/P from 25% up to 75% at $\bar{n}_e$~$5.10^{19}m^{-3}$. This implies that the beam density in the observed plasma-beam interaction region must be increased 3-10 fold to obtain reliable T_i measurements. Immediate upgrades of the TCV DNBI will result in an increase of the active signal by a factor of ~2 by increasing the injected current and by increasing the full energy component fraction from 70% to 80% by slightly increasing the beam voltage (up to 55kV), which improves the beam penetration.

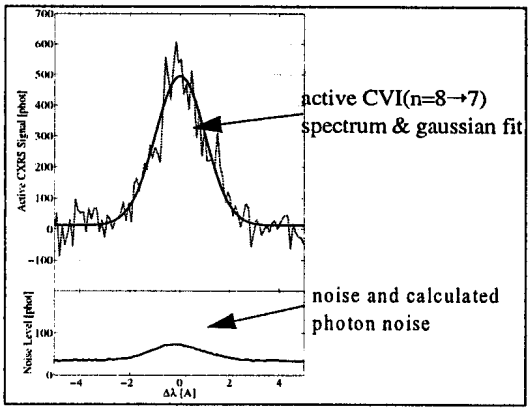

Figure 5: Measured and fitted CXR active spectrum (CVI(n=8 → 7) transition at 5291Å) for shot #19773 (integration time: 50ms). The noise intensity corresponds to the calculated photon noise.

A complete analysis of the CXRS optical system has identified modifications to the optical system that will increase the collection efficiency: (1) The observation etendue has been increased by ~3. (2) Two optical fibres superposed in the vertical direction are used to observe one radial position. (3) The low spectrometer etendue currently limits the total efficiency. Two F6 astigmatically corrected Czerny-Turner spectrometers will be purchased, giving a signal increase of the order of $\left(\frac{f/8.5}{f/6}\right)^2$ ~2. The spectral dispersion for these 0.66m instruments will allow an entrance slit width of ~300μm yet permit the measurement of T_i down to 100eV. (4) Two back-illuminated CCDs with a quantum efficiency of ~85% at 5300Å, are being constructed. Together, these changes will result in a signal level increase >15, improving the S/N of ~4.

7. CONCLUSIONS

Although neutral beam C/X spectroscopy has given extremely useful impurity temperature and density profiles on many machines, its implementation on modest sized machines is hampered by relatively high thermal neutral densities in the plasma edge. In order to achieve the high quality results, most often obtained with high power heating beams, the beam density in the observation region must be increased without significantly changing the plasma power balance. The challenge in constructing these beams, and the efficient optics that observe them, will require considerable optimisation.

Acknowledgments

This work was partly funded by the Swiss National Science Foundation.

References

[1] J. Mlynar et al., proceedings of WDS'01, MFF UK Prague (to be published)
[2] P. Gohil and al., GA-A20652, 1991
[3] EEV #CCD05-10, www.marconitech.com
[4] http://www.eirene.de

SUPRATHERMAL X-RAY EMISSIVITY WITH 2ND AND 3RD HARMONIC ELECTRON CYCLOTRON HEATING IN THE TCV TOKAMAK

S. Coda, Y. Peysson[a], S. Alberti, T.P. Goodman, M.A. Henderson, P. Nikkola, O. Sauter

Centre de Recherches en Physique des Plasmas
Association EURATOM-Confédération Suisse
Ecole Polytechnique Fédérale de Lausanne, CH-1015 Lausanne, Switzerland

[a]Département de Recherches sur la Fusion Contrôlée, Association EURATOM-CEA, CEA/Cadarache, 13108 Saint Paul-lez-Durance Cédex, France

1. Introduction

A multichordal, multichannel hard X-ray (HXR) pinhole camera, on loan from Tore Supra, is used on the TCV tokamak to study the spatial and spectral distribution of bremsstrahlung emission in the 10-200 keV range. Photon detection is effected by a linear array of CdTe detectors [1] with an intrinsic energy resolution of ~7 keV. Eight energy channels, with adjustable thresholds, are available for each of 14 vertical viewing chords, which span the outboard half of the plasma cross section with partially overlapping étendues and a radial resolution of approximately 2 cm on the midplane (see Fig. 1).

Hard X-ray radiation in the energy range under consideration is emitted by suprathermal electrons, and can thus be used to diagnose their spatial distribution and temporal dynamics; indirect information on the energy distribution of the fast electron population can also be gleaned from the HXR spectrum. In TCV, substantial HXR emission is generated when high power electron cyclotron waves are injected in the plasma with a finite parallel wave number; this injection scheme, which is used for electron cyclotron current drive (ECCD), creates measurable non-thermal photon distributions for injection angles deviating by more than 4-5° from the normal to the magnetic field [2]. For smaller angles, when the applied power is sufficient to raise the electron temperature above ~4 keV, the HXR diagnostic detects only the emission from the tail of the bulk Maxwellian distribution.

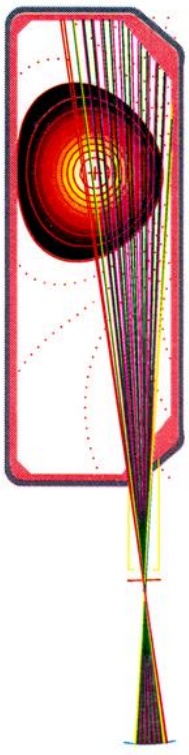

Fig. 1 *Geometry of hard X-ray camera. The chords are partially overlapped.*

The results presented in this paper pertain to the first set of experiments carried out with 470 kW third harmonic X-mode (X3) electron cyclotron heating (ECH) at 118 GHz [3]. The power was applied through a lateral launcher to the plasma center after a second harmonic X-mode (X2) preheating phase. The target plasmas has major radius R=0.88 m, minor radius

a=0.25 m, elongation κ=1.31, magnetic field B_T=1.42 T and central density $n_{e0}=2.5\times10^{19}$ m^{-3}. The X2 and X3 cold resonance locations are separated by ~5 cm and are distributed symmetrically on the high and low field sides of the magnetic axis, respectively. Both the X2 and X3 waves are launched from the low field side of the torus. The X2 power and launching geometry, as well as the plasma current, were selectively varied over a set of discharges in order to characterize the X3 absorption efficiency under a variety of conditions.

2. Dependence of suprathermal emission on X2 injection angle

The primary result of the X2-X3 experiments is that the absorbed X3 power fraction, measured by a diamagnetic loop (DML), is larger than the value predicted by linear calculations based on a Maxwellian distribution function [3]. In particular, a scan of the X2 toroidal injection angle, for constant 200 kA current and 470 kW X2 power, has revealed that the absorption has two maxima at $\phi\sim\pm20^o$ (where ϕ=-arcsin[$\mathbf{k}\cdot\mathbf{B}/(kB)$] at the absorption location, $\mathbf{k}$ is the wave vector, and the sign of ϕ is positive for co-current drive). The two peaks are asymmetric, the positive one being larger and reaching ~100%.

The HXR energy channels in this experiment were set at 8 keV intervals from 8 to 64 keV. In general, the logarithms of the spectra reveal the presence of two features: a low energy component with a slope consistent with the bulk temperature, and a higher energy component with lower amplitude but a lesser slope. By excluding the first two energy channels, a satisfactory linear fit can generally be obtained for the suprathermal part; the fit is robust in that the resulting photon temperature is insensitive to the elimination of additional channels. The result of the fit can be written as $d\gamma/dE=Ae^{-E/T}$, where γ is the emissivity; we can then characterize the suprathermal population by the temperature T_{ph} and the total emissivity $\gamma_{tot}=AT_{ph}$ for a central chord, i.e. for emissivity line-integrated over the entire plasma cross section. These two parameters are shown in Fig. 2 as functions of ϕ, for both the preheating X2 phase and the combined X2-X3 phase; the X3 absorbed power fraction is also plotted for comparison. The HXR signal was integrated over 0.2 s. The photon temperature during X2 heating increases indefinitely with $|\phi|$, confirming earlier results [2]; by contrast, the total emissivity peaks at the angles

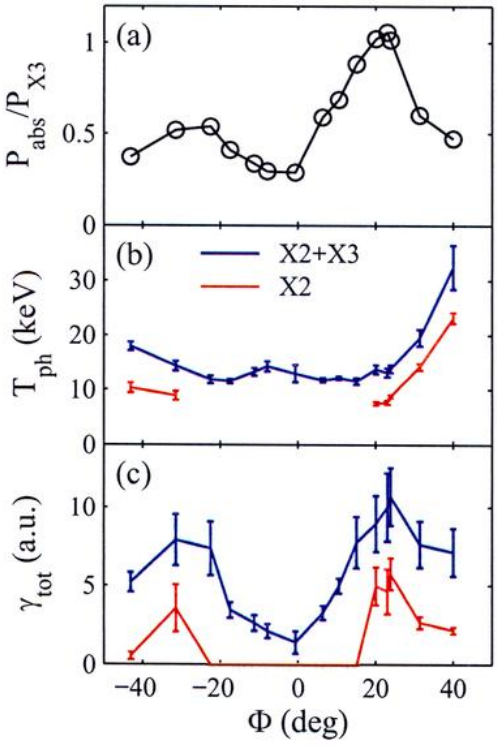

Fig. 2 *(a) X3 absorbed power fraction, (b) HXR suprathermal photon temperature, (c) integrated HXR emissivity, vs. ϕ (complementary to the angle between X2 wave vector and magnetic field). The suppressed points correspond to cases in which only the thermal spectrum is measurable.*

for which the X3 absorption is maximized. When X3 is applied, the emissivity increases further in all cases and the dependence on ϕ remains qualitatively similar. The photon temperature during X2+X3 is approximately 12-14 keV with little dependence on ϕ except at the highest angles, where an increase with $|\phi|$ is observed.

These results strongly suggest that the anomalously high absorption efficiency of X3 ECH is related to the presence of a suprathermal electron population in the plasma, which lies outside the scope of linear calculations in ray tracing codes. The further acceleration of these fast electrons by the X3 waves leads to a further increase in the emissivity. The final photon temperature, and indeed the form of the HXR spectra on all the chords, are only weakly dependent on ϕ. This suggests that the intrinsic efficiency of X3 absorption by the fast electron population is relatively insensitive to the detailed spectrum of the initial "seed" distribution, and that the ultimate distribution is primarily determined by the characteristics of the X3 waves. Only for the highest toroidal angles, at which the X2 waves are able to significantly populate energy levels in excess of 50 keV, does the final distribution retain a measurable memory of the seed distribution. The most significant factor influencing the X3 absorption thus appears to be the total density of fast electrons rather than their energy distribution.

3. Spatial distribution of hard X-ray emissivity

The spatial distribution of the local HXR emissivity is reconstructed by assuming poloidal homogeneity and performing profile inversions with the Fischer regularization method. The spatial profiles, normalized to a maximum of unity, are shown for both the X2 and X2+X3 phases for several values of ϕ in Fig. 3. The 40-48 keV energy range has been chosen to prevent pollution of the signal by the thermal bulk. The location of the primary peak can be taken to be at $\rho=0$ in all cases, as the shift to $\rho\sim0.1$ seen in some discharges is not significant within the accuracy of the equilibrium reconstruction (ρ is the square root of the normalized poloidal flux). The width of the X2 profiles is an increasing function of $|\phi|$, consistent with the

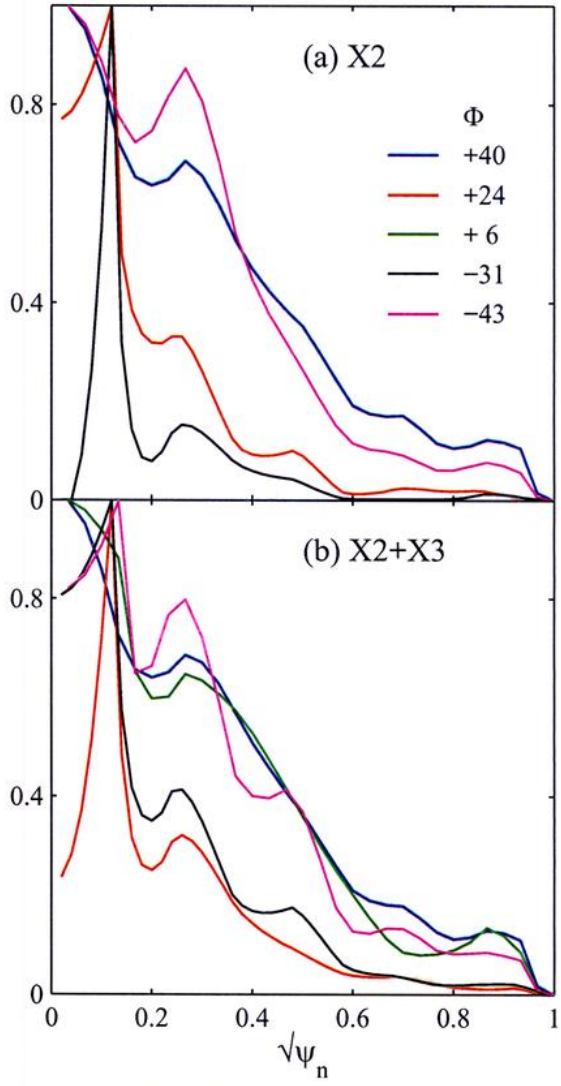

Fig. 3 *Profiles of local HXR emissivity in the 40-48 keV range for (a) X2 and (b) combined X2 and X3 heating, vs. normalized radial coordinate, for 5 values of the angle ϕ.*

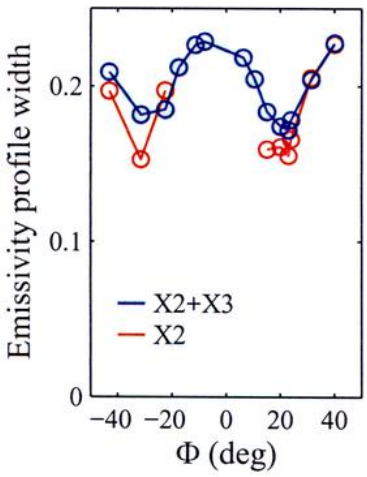

Fig. 4 Root mean square width (in units of $\psi_n^{-1/2}$) of the HXR emissivity profile, in the X2 and X2+X3 heating phases, vs. X2 resonance angle ϕ.

increasing spread of the absorption region towards the low field side caused by Doppler shift of the resonance frequency. The X2+X3 profiles are close to their X2 counterparts for angles at which there is a measurable suprathermal signal during X2; at lower values of $|\phi|$, the X2+X3 profiles become broader and essentially independent of ϕ. This is exemplified by Fig. 4, which shows the rms profile width as a function of ϕ. It may be speculated that X3 absorption, and the attendant fast electron acceleration, occurs preferentially in the spatial region occupied by the seed suprathermal electrons; at the smallest angles, for which the seed population is negligible, the X3 absorption coefficient is smaller and the damping profile appears to be determined by the properties of the X3 wave alone.

In spite of the strong variation of the absolute emissivity across the plasma cross section, the form of the spectrum is essentially constant in space, as illustrated in Fig. 5 by the spatial distribution of the photon temperature. This is true in a wide variety of conditions and suggests that the radial diffusion rate of suprathermal electrons may not depend significantly on energy.

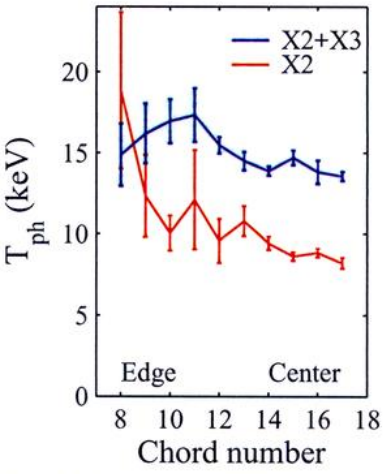

Fig. 5 Suprathermal photon temperature from line-integrated HXR emission vs. chord number, in the X2 and X2+X3 phases of a shot with ϕ=+24°.

Acknowledgments

The loan of the HXR camera and associated electronics by the CEA is gratefully acknowledged. Thanks are due to L. Delpech for technical support and to the entire TCV team for the operation of the tokamak and of the auxiliary heating systems. This work was supported in part by the Swiss National Science Foundation.

References

[1] Y. Peysson, S. Coda and F. Imbeaux, Nucl. Instrum. and Methods in Phys. Res. A **458** (2001) 269; Y. Peysson and F. Imbeaux, Rev. Sci. Instrum. **380** (1999) 3987.

[2] S. Coda et al., Proc. 26th EPS Conf. on Controlled Fusion and Plasma Physics (Maastricht 1999), Europhys. Conf. Abstr. **23J** (1999) 1097.

[3] S. Alberti et al., Proc. 18th Int. Conf. on Plasma Physics and Controlled Nuclear Fusion Research, Sorrento, Italy, 2000 (IAEA, Vienna, to be published).

[4] R.W. Harvey and M.G.McCoy, in Proc. IAEA TCM/Advances in Simulation and Modeling in Thermonuclear Plasmas, Montreal (1992)

Characterisation of impurities in L and H modes created by divertor biasing and plasma triangularity in TdeV

I. Condrea[1,2], E. Haddad[1,3], C. Côté[1] and B. C. Gregory[1]

[1]Centre Canadien de Fusion Magnétique, Varennes, Québec J3X 1S1, Canada
[2]Centre de Recherche en Physique des Plasmas, Association EURATOM- Confédération Suisse, EPFL, CH-1015 Lausanne, Switzerland
[3]MPB Technologies, Dorval, Canada

ABSTRACT

A characterisation of the H mode in Tokamak de Varennes (TdeV), combining results obtained from spectroscopic measurements with observations of global plasma parameters is presented. Controlled L and H modes are obtained by applying an external biasing on the divertor plate and/or by varying the plasma triangularity using similar steady-state discharges with ECRH heating. The poloidal velocities are small with no significant variations with respect to the plate biasing, EC power and plasma triangularity. Toroidal rotation velocities show more consistent trends and have larger values in the H modes with respect to the L modes. No significant shear in the radial electric field is observed between the H and L modes. Differences in the electric field and in the ExB shear are observed for several discharges but they are not consistent overall. The energy confinement time decreases with the ELM severity and consequently with the neutral fluxes. The presence of a toroidal torque which affects the particle transport inside the plasma plays an important role in the TdeV H modes.

1. Introduction

In this paper we present results of H modes compared with L modes created in TdeV (divertor single null configuration tokamak). Two methods were used to achieve well controlled stationary H modes exhibiting type III ELMs in addition to auxiliary heating (ECRH and LH): varying the plasma lower triangularity and applying a biasing between the divertor plates and the vacuum chamber. H and L mode TdeV discharges with similar parameters were chosen: B_T = 2 T, I_p = 160-220 kA, $\langle n_e \rangle$ = 2- 5 x 10^{19} m^{-3}, R=0.83 m, a = 0.21 m, with the $B \times \nabla B$ drift both towards (more favourable to H modes) and away from the X point but different plasma triangularities (0.1-0.24), biasing voltage (-310 to 250V) and deposited EC power (150-480 kW). The edge density was fixed during the discharge (slightly higher than the L-H density threshold in order to pass easily from an L to an H mode), leaving the central density free to vary. The machine walls were boronised, reducing the oxygen and carbon impurities. Spectroscopic measurements of the rotational velocities are presented and discussed together with more general results on the plasma parameters during the L and H modes. As the temporal resolution of our spectroscopic system is low (200 ms), these results characterize the steady-state H and L mode phases rather than the L-H transition, and are averaged over ELMs.

A typical H mode observed in TdeV is shown in Figure 1: a drop in the D_α radiation with a presence of ELM activity, a rise in the total stored energy and energy confinement time, and a rise in the line-averaged electron density. The electron density (measured with a 9-channel submillimeter interferometer) and temperature radial profiles (measured with a 8-channel infrared Thomson scattering diagnostic) in H modes obtained by varying the triangularity and the divertor plate bias (not

shown here) readjust such that the local pressure remains approximately constant. Unfortunately the spatial resolution for both the interferometer and Thomson scattering diagnostics is too low to clearly see the presence of a pedestal inside the separatrix. The electron density profile around the separatrix measured by the reflectometer (33-75 GHz), is observed to be steeper in the H mode than in the L mode (see Figure 2). In TdeV, the normal direction of the plasma current, I_p^+, refers to the clockwise direction looking downwards ($B \times \nabla B$ drift away from the divertor). The central ion temperature, the total radiated power and Z_{eff} were measured respectively with the charge-exchange analyser, bolometer system viewing the whole poloidal section of the hot plasma, and visible Bremsstrahlung radiation.

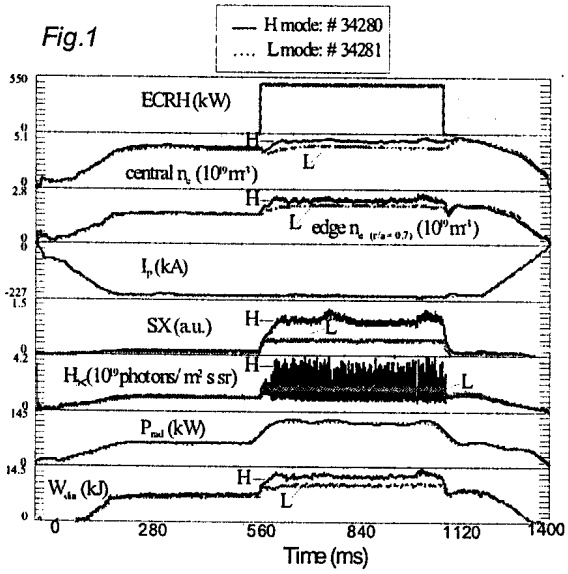

Fig.1

Two calibrated soft X-ray spectrometers viewed radially the central and half-radius plasma. Reference [1] provides more details of these diagnostics. The emissivities, the poloidal and toroidal velocities and the ion temperature profiles were measured simultaneously with a spectroscopic set-up[2] observing the plasma both poloidally and tangentially using chords in the vertical plane (see Figure 3).

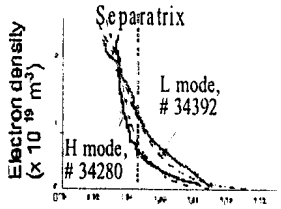

Fig. 2

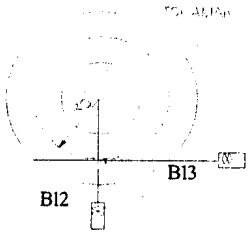

Fig. 3

The line integrated signals deduced from the Doppler shifts and broadenings of BV (at 494.4 nm) and CIII (at 464.7 nm) emission lines were inverted using a matrix inversion method where the real flux lines were deduced from experimental coil currents and a (MHD) magnetohydrodynamic equilibrium code[3].

2. Results

Considering that the maximum emission of CIII and BV is localised in the region r/a = 0.6-1.2 , only profiles within this range are available. In Figure 4 is shown the dependence of the rotation velocity of the applied bias for discharges with H and L modes. Averaged velocity values around r/a = 0.85 (0.8 < r/a <0.9) and 1.0 (0.95 < r/a < 1.05) are considered for bottom and top poloidal and toroidal velocities. The biasing is applied between the upper divertor plate and the wall and one would expect to see a stronger effect in that region. The poloidal velocity is generally low with small differences between the values in the H and L modes. The error bars are high due to the low brightness in the poloidal view. The biasing does not seem to affect the poloidal velocities at both locations (inside and around the separatrix) whereas it clearly affects the toroidal velocities, more prominently inside the separatrix. This means that the biasing has an effect deeper inside the plasma even if it is applied in the SOL. There is a threshold in both top and bottom toroidal velocity when passing from L to H

mode (Δv –4-6 km/s). The CIII poloidal velocity is also weak (see Figure 5). The toroidal velocities see an effect of the biasing, more prominent in the upper part, for both plasma currents. This observation is similar to the one observed for BV around r/a =1 but with larger velocities. The radial profile of the electric field (E_r) was calculated with the momentum balance equation from the BV line, for the discharges with I_p^- at 160 kA and 220 kA respectively. The BV ion density profile was

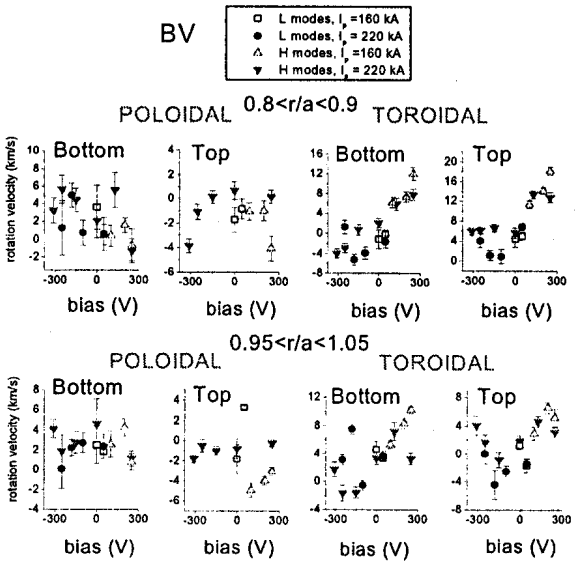

Fig. 4

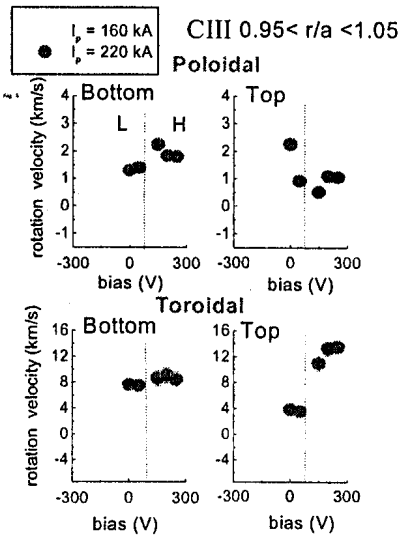

Fig. 5

calculated using the transport code MIST. The $v_\theta B_\phi$ and $v_\varphi B_\theta$ terms dominate over the pressure gradient term (the differences between the temperatures in H and L mode are only 15-20%).
Inside the separatrix (region where the difference in the electron density gradient between the L and H modes is observed), the contributions from the poloidal and toroidal velocities are comparable;

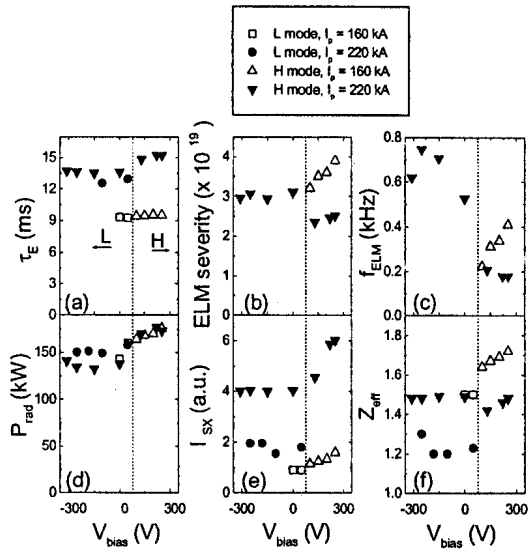

Fig. 6

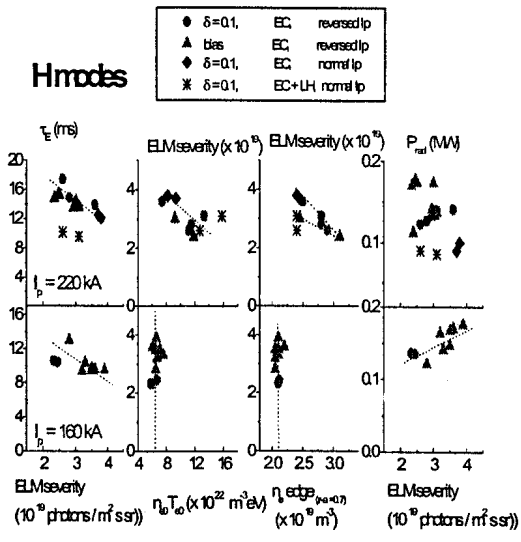

Fig. 7

differences in the profiles of the E_r are observed between different biasing voltages (more prominent further inside the separatrix at r/a<0.9). Unfortunately, the error bars associated to E_r are high due to the errors in the poloidal velocity. A similar behaviour in the E_r calculated using CIII (not shown) for r/a > 0.95 was observed, confirming the absence of a strong shear in that region.

As can be seen from Figure 6 (a) there is a jump in the energy confinement time, ELM severity[4] (b), ELM frequency (c), radiated power(d), SX radiation (e) and Z_{eff} (f) when passing from negative to positive biasing. This behaviour is similar to that observed in the toroidal velocities inside the separatrix. H mode discharges obtained with different discharge scenarios are plotted in Figure 7. A general tendency in the energy confinement time to decrease with the ELM severity is seen for both 220 and 160 kA. A correlation between the ELM severity and the electric pressure and the edge electron density is observed only at 220kA, with no substantially change at 160 kA. Lower ELM severity is observed for higher edge electron density (which is the parameter used to control the L-H transition).

3. Discussions and conclusion

As a general observation, the poloidal velocities in TdeV remain relatively small during the steady-state phases of both H and L modes. The experimental uncertainties are high for this parameter but we conclude that there is no significant poloidal rotation in the H mode. Even if there is rotational shear during the L-H transition (which we cannot measure), the velocity returns to low values. The weak poloidal velocities might not be the crucial factor in the evolution of the TdeV H mode.

The ion temperature in the H mode is slightly higher than in the L mode but only by 10-20%. No important shear is observed in the electric field even if there are differences in the electric field itself and its shear between the H and L modes. The toroidal velocities are higher in the H mode than in the L mode. This behaviour has been seen consistently for the H modes obtained using different methods. The divertor bias and the plasma triangularity have a clear effect on the toroidal velocities which seem to be a key parameter in the H modes in TdeV. The energy confinement time decreases with the ELM severity and consequently with the neutral fluxes. The fact that the toroidal velocity has high values and depends on the majority of the plasma parameters in the H modes[5], suggests that the presence of a toroidal torque which affects the particle transport inside the plasma may play the primary role in the TdeV H modes.

REFERENCES

[1] The TdeV team, CCFM internal report, CCFM RI 450f, (1994).

[2] I. Condrea, E. Haddad, B. C. Gregory, D. Lafrance, J.-L. Lachambre, G. Pacher, F. Meo and H. H. Mai, Rev. Sci. Instrum. **70**(1), 387 (1999).

[3] I. Condrea, E. Haddad, B. C. Gregory and G. Abel, Physics of Plasmas, 7 (9) (2000).

[4] W. Zhang, B. J. Tubbing and D. J. Ward, Plasma Phys. Control. Fusion 40 (1998) 335-346.

[5] I. Condrea, E. Haddad, C. Côté, B.C. Gregory, Plasma Phys. Control. Fusion 43 (2001) 71-98.

DYNAMICS OF EDGE LOCALISED MODES ON TCV

A W Degeling, Y R Martin, P E Bak[1], J B Lister, X Llobet

Centre de Recherches en Physique des Plasmas, Association EURATOM-Confédération Suisse, Ecole Polytechnique Fédérale de Lausanne, 1015 Lausanne, Switzerland

[1]JAERI Naka Fusion Research Establishment, Naka-machi, Naka-gun, Ibaraki-ken 311-0193, Japan

1. Introduction

Recent work on JT-60U [1] and JET [2] indicates that ELM occurrences sometimes exhibit behaviour that is characteristic of a deterministic, non-linear dynamical system in a chaotic state. The ELM time-series of some discharge were found to contain a specific type of short sequence known as an Unstable Periodic Orbit (UPO). This result opens the door to a new way of characterising the dynamics of ELMs, and also is extremely encouraging from the point of view of controlling the ELM amplitudes by controlling the ELM period. We extend this previous work by examining the ELM time-series from a large number of ELMy H-mode discharges from the TCV tokamak for occurrences of UPOs. Further, we investigate how the properties of UPOs found vary with plasma parameters, pointing the way to establishing the necessary requirements for candidate models of ELM dynamics.

2. The search for chaos in ELM time-series

The repetitive occurrences of ELMs strongly suggest the existence of a cyclic dynamical system, like a relaxation oscillator. If this is the case then the observed D_α emission reflects the time variation in one of, or a combination of, the dependent variables of the dynamical system. Generally, cyclic dynamical system may have families of periodic solutions (called fixed points). Chaos ensues when a cyclic system is bounded, yet all of these fixed points are unstable to small perturbations. A UPO occurs when the state of the system momentarily approaches, and then exponentially diverges from one of these unstable solutions. During this brief time, the system behaves in a linear way, and gives rise to a characteristic signature in the time-series of each of the dependent variables. This may be detected by monitoring variations in consecutive periods ΔT_i of one of these variables about the period of the fixed point ΔT^*. These variations give rise to short strings of consecutive points (at least 3) that lie in a straight line of slope s on the return map (a scatter plot of ΔT_i versus ΔT_{i+1}), and intersect the diagonal at ΔT^*. The D_α time-series for each ELMy H-mode discharge on TCV was reduced to a sequence of inter-ELM periods

(ΔT), and each sequence was searched for UPOs using a set of selection rules. Figure 1 shows the appearance of 2 UPOs in the ELM time series, the sequence of ΔTs, and on the return map. A total of 241 TCV ELMy H-mode discharges with up to 400 ELMs per discharge were examined, of which 143 discharges were found to contain 536 occurrences.

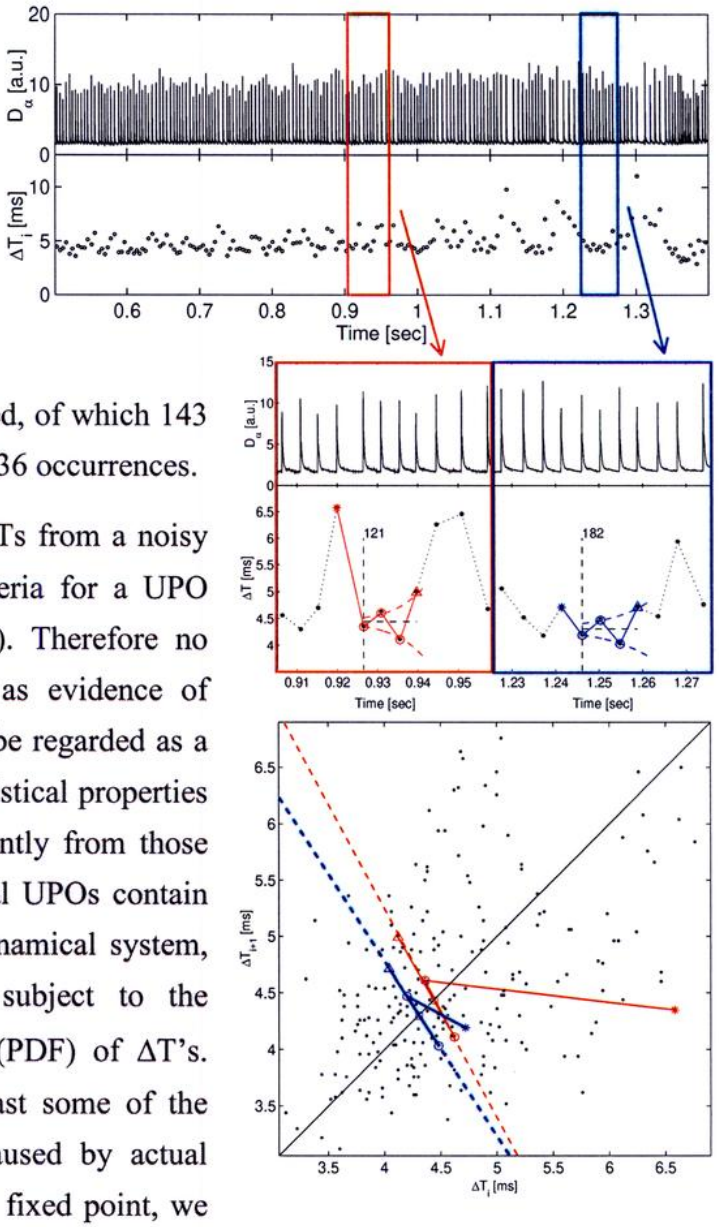

Figure 1: Example of UPO detection showing the original D_α time-series, the sequence of ΔTs and the return map.

It is also true that sequences of ΔTs from a noisy system may fit the selection criteria for a UPO simply by chance ("fake UPOs"). Therefore no single occurrence can be taken as evidence of chaos, and each sequence should be regarded as a UPO candidate. However, the statistical properties of real UPOs will differ significantly from those that occur by chance, because real UPOs contain specific information about the dynamical system, whereas fake UPOs are only subject to the probability distribution function (PDF) of ΔT's. To test the hypothesis that at least some of the observed UPO candidates are caused by actual close encounters with an unstable fixed point, we consider the null hypothesis: that ELM dynamics are always random or noise dominated, and that all the UPO candidates fake. If this is the case, then no information is carried in the particular ordering of the ELM time-series. Any random re-ordering of a given time-series, called a surrogate set, should be equivalent to the original, and have the same probability of giving rise to a fake UPO with a particular ΔT^*, because the PDF is unchanged. One hundred such surrogate sets were generated for each of the 241 ELMy H-mode discharges and each was searched for UPO candidates using the same algorithm employed on the original data. Summing over the 241 discharges and computing the mean and standard deviation over the 100 surrogate series, we should expect a total of 393 ± 16 UPO signals if the null hypothesis is true. Our finding of 536 UPOs is 8.9 standard deviations larger than this

value, hence we reject the null hypothesis and conclude that ELM occurrences are the result of a deterministic process.

Before we can examine how UPO properties vary with plasma parameters, we must separate the real UPOs from any fake ones in our experimental data. We accomplish this by using the surrogates to define the statistical properties for fake UPOs. Each UPO is characterised by its fixed point value ΔT^* and the rate of exponential divergence of ΔT from ΔT^*, which appears on the return map as a sequence of points with constant slope s. We examine the re-occurrence properties of these parameters for UPOs by plotting the histograms for $\delta T = |\Delta T^* - \Delta T^*_1|$ and $\delta s = |s - s_1|$, where ΔT^*_1 (with slope s_1) is the nearest neighbour to ΔT^* (with slope s) from the same discharge. As shown in figure 2a., the experimental data shows a clear peak above the surrogate data for lower values of δT and δs, while the real and surrogate distributions are indistinguishable for higher values of δT and δs. We therefore filter the data, removing all UPOs with $\delta T < 0.05$ ms and $\delta s < 0.5$ (shown by the vertical lines in the figure 2a. to give figure 2b.). A total of 168 UPO candidates from 39 discharges passed this filter, compared to only 10±3 fake UPOs from their corresponding surrogates, hence each of these candidates has greater than a 90% chance of being a real UPO. In figure 2c., the experimental and surrogate data rejected by the filter are in-distinguishable, indicating the efficiency of the filter in separating the real and fake UPOs.

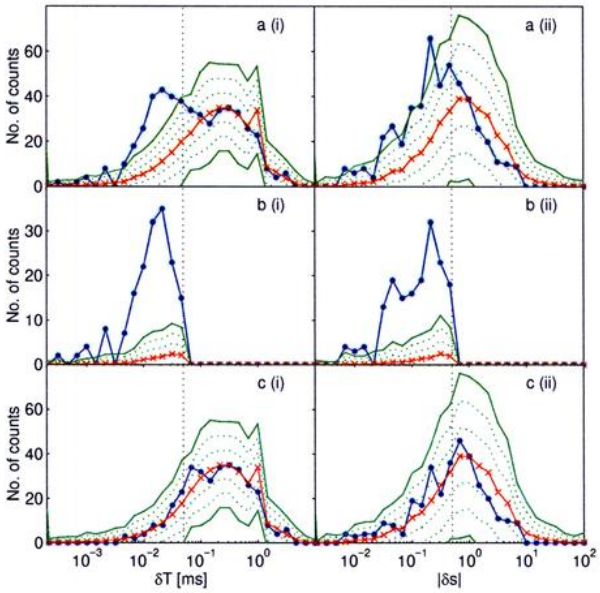

Figure 2: (i) and (ii) : The distributions of δT and δs for: experiment data (blue), mean of surrogates (red) ± 3 standard deviations (green), a) raw data, b) filtered data, c) data rejected by the filter

3. Unstable Fixed Point Dependence with Plasma Parameters

Variations of ΔT^* with the plasma parameters were investigated to search for any systematic behaviour. The method of analysis was to choose a specific parameter, and remove points from the database that vary by more than a given tolerance in each of a number of other key parameters, defining a small multi-dimensional parameter window for examination. In so doing, the variation of ΔT^* with the parameter of interest in each case was estimated, keeping the other parameters roughly constant, within the tolerance in

each parameter. Figures 3a – c. show the variation in ΔT^* with I_p, the plasma – inner wall distance, and n_e respectively obtained by this method. These figures show generally increasing trends of ΔT^* with these three parameters, and are consistent with known scalings of the ELM frequency. This comes as no surprise, since ΔT^* must lie within the distribution of ΔTs, however our interpretation is the reverse: These known scalings arise *because* of movements in ΔT^* in the underlying dynamical system. Another interesting feature in figures 3b. and c. is the development of an upper and lower trend for ΔT^*, although the scattering of points is sparse. Figure 3c. shows repetitions of these upper and lower trends in three separate parameter windows.

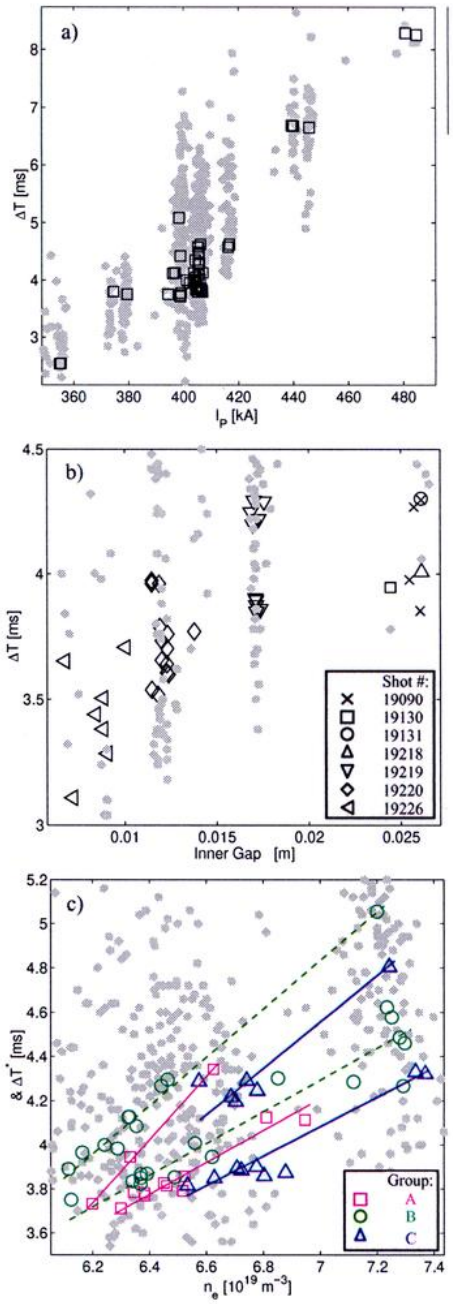

Figure 3: variation of ΔT^* with a) I_p, b) inner plasma - wall gap, and c) n_e.

4. Discussion

Techniques exist for controlling chaotic dynamical systems by means of small feedback corrections. These algorithms are designed to stabilise a UPO and obtain regular behaviour by locking onto a desired fixed point. The implications for the control of ELMs are by analogy with other chaotic systems. By choosing a fixed point with a low ΔT^*, such control minimises the probability of large inter-ELM periods, and hence large ELMs. To do this, a control parameter must be found that influences ELM dynamics near the fixed point. The search for a suitable parameter continues.

The authors sincerely thank the TCV Team, without whom these experimental results would be unavailable. This work was partly supported by the Swiss National Science Foundation.

[1] Bak P. E., Yoshino R., Asakura N., Nakano T., 1999 Phys. Rev. Lett. **83** 1339

[2] Bak P. E., 1999, PhD Thesis, University of London

COMPARING DINA CODE SIMULATIONS WITH TCV EXPERIMENTAL VDE RESPONSES

J-Y. Favez[1], R.R. Khayrutdinov[2], J.B. Lister[1], V.E. Lukash[3]

[1] *Centre de Recherches en Physique des Plasmas, Association EURATOM-Confédération Suisse, EPFL, 1015 Lausanne, Switzerland.*
[2] *TRINITI, Troitsk, Russia.*
[3] *RRC Kurchatov Institute, Moscow, Russia.*

1 Introduction

The DINA free-boundary equilibrium simulation code [1] has been implemented for TCV, including the full TCV feedback and diagnostic systems. First results showed good agreement with control coil perturbations and correctly reproduced certain non-linear features in the experimental measurements [2]. The latest DINA code simulations, presented in this paper, exploit a set of 14 discharges with different cross-sectional shapes (δ) and different vertical instability growth rates of about $200\,rad/s$ which were subjected to controlled Vertical Displacement Events (VDE). They were carried out on limited plasmas in the TCV tokamak to validate a deformable plasma model of the vertical instability [4], extending previous work with the DINA code on the DIII-D tokamak [3]. The height of the TCV vessel allows observation of the non-linear evolution of the VDE growth rate as regions of different vertical field decay index are crossed. This work focuses on the comparison of the most common equilibrium parameters like the vertical position z, the plasma current I_p, the elongation κ, the triangularity δ and the safety factor q, between the TCV experiments and the DINA simulations. Additionally, the evolution of the growth rate γ of both DINA and TCV is estimated and compared with the evolution of the closed loop growth rate calculated with the RZIP linear model [6].

2 Experimental conditions

In the TCV experiment the VDE was initiated by interrupting the control of the radial and vertical position at $t = 0.45\,s$. Because of the plasma disturbances and noise, mainly generated by the power supply and the diagnostics, and due to the fact that the plasma is unstable in vertical direction, the VDE is immediately initiated. For DINA we modeled such disturbances and noise by injecting an antisymmetric trapezoidale shaped voltage pulse on the E1 and E8 coils.

In general, it is obvious that we cannot expect a perfect agreement between the TCV experiments and the DINA simulations. There are several possible reasons for any disagreements of the responses between the TCV experimental results, obtained with the LIUQE code [5], and the DINA simulations.

1. The LIUQE code reconstructs the plasma evolution of a discharge by means of a parameterised function set for current and pressure profiles and a fitting algorithm calculating the parameter-values of these functions. This reconstruction method leads

to results that mainly follow the experiment but cannot show all details of the plasma evolution.

2. When starting the simulations with badly chosen initial states, a significant transient is observed before the simulation settled down to reproduce the TCV time traces more or less accurately [2]. This transient can be due to the different equilibrium parametrisation used by the LIUQE inverse equilibrium code and the DINA simulation code and can lead to an offset between the responses of the experiment and the DINA simulation.
3. The electronics, particularly the amplifiers and integrators implemented in the diagnostics to evaluate the magnetic fields and the fluxes, may have small offsets. This adds offsets and constant slope drift errors to the measurements of the fields and fluxes.

3 Comparison between TCV and DINA

Figure 1 shows, for the 5 most representative discharges, the evolution of the vertical position z, the plasma current I_p, the elongation κ_{95}, the triangularity δ_{95} and the safety factor q_{95}, the last three parameters estimated at 95 % flux surface. We limit the comparison to the time before the final disruption occurs. To distinguish the instant of the final disruption we used the H_α signal, illustrated in the last row. The time when the disruption occurs is approximately determined by identifying the maximum value of H_α, marked by a vertical line in the other plots of figure 1.

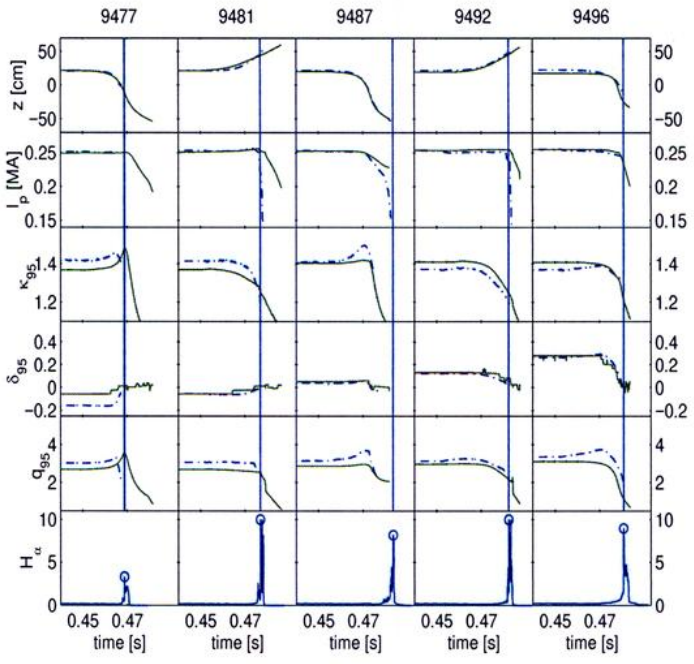

Figure 1: Comparison of the vertical position and the equilibrium parameters. (solid: DINA, dashed: LIUQE)

For the discharges 9477, 9481 and 9492, we observe a delay between the DINA simulations and the experiments (see for example I_p and κ_{95}). This may be due to difficulties reconstructing the plasma evolution correctly as the disruption approaches.

The most striking feature of this comparison is that all experiments with the plasma position z going downwards have an S-like shape consisting of a fast exponential-like movement at the beginning and a slowing down part at the end just before the disruption occurs. Since the z position at equilibrium is located at $+20\,cm$ from the vessel centre, the distance the plasma can move, before the disruption, is shorter for the experiments

with an upward going vertical displacement. These experiments therefore only show the initial exponential shape. The correct reproduction of the S-like shape is a strong point for a non-linear code like DINA. It should be borne in mind that such behaviour cannot be modeled by linear time-independent models because of the predominant exponential shape of the vertical instability if the growth rate is fixed.

For the TCV experiments, we observe a peak in the elongation κ_{95} and in the safety factor q_{95} when the plasma current decreases slowly (discharges 9477 and 9487). DINA reproduces this peak only for discharge 9477. This is the most important disagreement and could not be explained so far. The offset, which can be noticed for almost all discharges, is typically due to the problem of determining the right initial conditions for the simulations discussed before.

The agreement of the triangularity δ_{95} is excellent for all discharges, except for discharge 9477. Despite the fact that for this discharge the initial values start at $t = 0.3\,s$ with approximately the same values as the TCV experiments, the system relaxes to a DINA equilibrium, which induces a huge offset of δ_{95}. Like for κ_{95}, this belongs also to the problem of determining the right initial conditions for the simulations.

4 Comparison of the growth rate

In this section we compare the growth rate evolution of the TCV experiments, the DINA simulations and the RZIP linear model, based on the assumption of rigid displacement of the current distribution [6].

The growth rates of RZIP are established by calculating the eigenvalues of the RZIP linear model in closed loop (with the feedback loops closed, except for the vertical and radial positions). For the TCV experiment and the DINA simulations, the growth rates are calculated using the vertical plasma position data $z(t)$. This calculation is based on the assumption that $z(t)$ can be modeled by the function

$$z(t) = z_0 + \delta z\, e^{\int_{t_0}^{t} \gamma(\tau) d\tau} \qquad t \geq t_0 \tag{1}$$

where the time t_0 is the time where the VDE is initiated, in our case $t_0 = 0.45\,s$. We furthermore assume that z_0 and δz are constant in time and the growth rate γ is a function of time.

This assumption allows us to estimate the growth rate simply from the evolution of the vertical plasma position. We used the following method to estimate $\gamma(t)$:

$$\frac{d}{dt} \ln |z(t) - z_0| = \frac{d}{dt} \ln \left(|\delta z| e^{\int_{t_0}^{t} \gamma(\tau) d\tau} \right) = \frac{d}{dt} \left[\ln |\delta z| + \int_{t_0}^{t} \gamma(\tau) d\tau \right] = \gamma(t) \tag{2}$$

The comparison of the growth rate is shown in figure 2. The first and second rows illustrate $z(t) - z_0$ and $\ln |z(t) - z_0|$ of the LIUQE and the DINA data. The third row shows the evaluated growth rates for LIUQE, DINA and RZIP. We clearly see, especially

for LIUQE, the noisy results in the initial phase where the growth rate is assumed to be constant. This is due to the noisy $z(t)$ data which is amplified by the derivative of $\ln|z(t)-z_0|$ in equation 2. By inspecting the RZIP growth rate, we see that the assumption of a constant γ in the initial phase appears valid.

Comparing the LIUQE and RZIP growth rates we can see good agreement, except for some discharges with downward going displacements. For these discharges, we observe a delay when γ suddenly decreases rapidly in the final phase (discharges 9480 and 9493). Despite this, the good agreement seems to be obvious, since the RZIP code uses LIUQE results to elaborate a model.

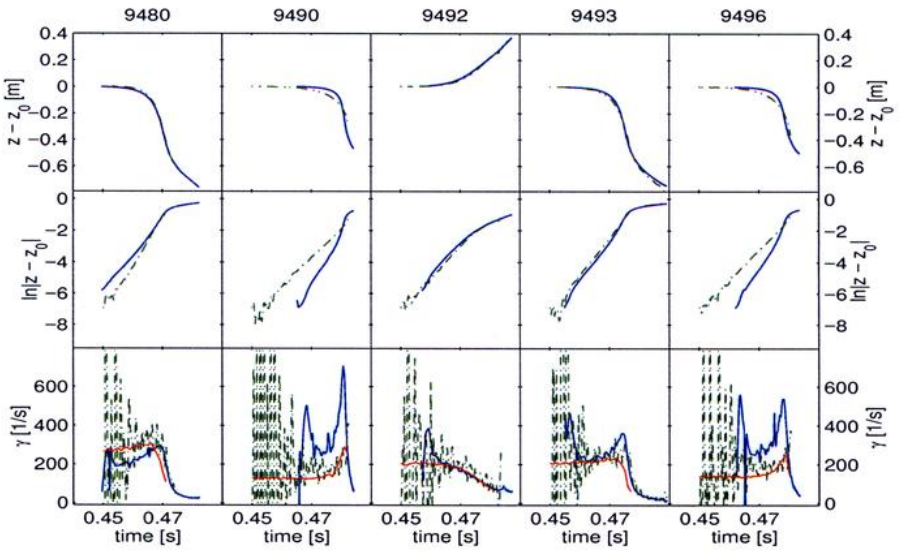

Figure 2: Comparison of the growth rate between DINA (solid blue), LIUQE (dashed green) and RZIP (solid red).

For the comparison between the LIUQE and DINA results, we can state that the agreement is as good as the agreement of the vertical position $z(t)$ (see section 3). By inspecting the discharges 9490 and 9496 we observe a discrepancy of $\ln|z(t)-z_0|$ which is a result of a small disagreement of $z(t)$. We cannot therefore expect such a good agreement of the growth rates for these discharges.

This work was partly supported by the Swiss National Science Foundation.

References

[1] Khayrutdinov R.R., and Lukash V.E., J. Comp. Physics 109 (1993) 193

[2] R.R. Khayrutdinov, J.B. Lister, V.E. Lukash, J.P. Wainwright, "Comparing DINA code simulations with TCV experimental plasma equilibrium responses", Plasma Physics and Controlled Fusion, 43 (2001) 321.

[3] Humphreys, D.A., Khayrutdinov, R.R., Lukash, V.E., "Time-Dependent Simulation of DIII-D Plasma Evolution and Control Scenarios", APS, v. 40 (1995) 1191

[4] Hofmann F. et al., Nuclear Fusion 37 (1997) 681

[5] Hofmann F. and Tonetti G., Nuclear Fusion 28 (1988) 1871

[6] Coutlis A., Bandyopadhyay I., Lister J.B., Vyas P., Albanese R., Limebeer D.J.N., Villone F., Wainwright J.P., Nuclear Fusion 39 (1999) 663

THE ROLE OF NON-MAXWELLIAN ELECTRON DISTRIBUTION FUNCTIONS IN 2ND AND 3RD HARMONIC ELECTRON CYCLOTRON ABSORPTION IN TCV

T.P. Goodman, S. Alberti, P. Blanchard, S. Coda, P. Gomez, M.A. Henderson, P. Nikkola, O. Sauter

Centre de Recherches en Physique des Plasmas
Association EURATOM-Confédération Suisse
Ecole Polytechnique Fédérale de Lausanne
CH-1015 Lausanne, Switzerland

1. Introduction

TCV [1] is a moderate-size tokamak (R=0.88 m, a = 0.25 m) with a highly elongated vacuum vessel allowing the creation of plasmas up to $\kappa \sim 3$ (κ=2.8, achieved [2]). The sole auxiliary heating system on TCV is ECH [3], consisting of 6 X2 (82.7GHz) gyrotrons and 3 X3 (118GHz) gyrotrons. The complete X2 system has been in operation since 1999 and the first of the 3 X3 gyrotrons was used for absorption experiments for the first time in 2000 [4] by installing a microwave switch in one of the X2 evacuated transmission lines. Thus, either X2 or X3 power can be launched from the X2 antenna of that line (i.e. the frequency from that antenna can be changed from shot to shot).

All X3 power is intended to be launched from one antenna at the top of the machine in order to take advantage of the increased optical depth resulting from propagation along the elongated length of the resonance in high elongation plasmas. The standard low field side (LFS) launch used for the X2 power would, for a Maxwellian electron distribution function, result in only ~ 60% X3 absorption for even the hottest [5] TCV plasmas. Nevertheless, LFS launch of the X3 has resulted in up to 100% absorption when the plasmas are pre-heated with X2 ECCD. A vertically-viewing 14 chord hard X-ray camera [6] and 21-channel high field side (HFS) electron cyclotron emission (ECE) diagnostic [7] provide evidence of the strong non-maxwellian nature of electron distribution function during both X2 ECCD pre-heating and later, additional, X3 heating. This suggests that the excess X3 absorption is on the non-Maxwellian part of the electron distribution.

2. Experiments and Setup

The typical launch configuration is shown in fig. 1. One sees that because the frequency ratio of X3 to X2 is less than 3/2, the X3 resonance is to the LFS of the X2 resonance. The two cold resonances span the plasma axis at nominal field (B=1.43 T). The X3 power is always launched in ECH from one upper lateral launcher while the X2 power is launched from one or more of the remaining (3 upper lateral and 2 lower lateral) launchers. For the toroidal scan, one X2 launcher is used; similar results are found using either an upper or lower launcher

For the first absorption measurements, the hottest plasmas were chosen. These are created with X2 counter-ECCD on axis [5]. The DML measured absorption larger than expected during mECH of the X3. Several experimental scans were carried out to identify the source of the excess absorption [4].

The experiments are divided into 5 categories: 1) X3 polarization scans aimed at distinguishing the role of first pass versus multipass absorption, 2) X2-pre-heating power scans in co/counter/ECH configurations, 3) X2 pre-heating toroidal scans at the lowest X2 power level yielding ~100% absorption in co-ECCD, 4) a scan of I_p to study the role of $E_{//}$ in the X3 absorption (not shown) and 5) modulated-ECH (mECH) diamagnetic loop (DML) tests including mECH frequency scans [8] (not covered here).

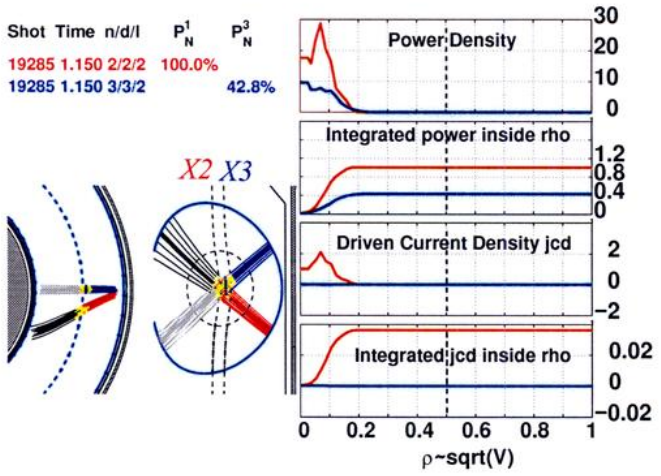

Fig. 1 Typical launch configuration for co-ECCD X2 pre-heating and ECH X3 absorption. Grey rays indicate incomplete absorption on a maxwellian plasma (blue - launcher 3 X3; red - Launcher1 X2 preheat).

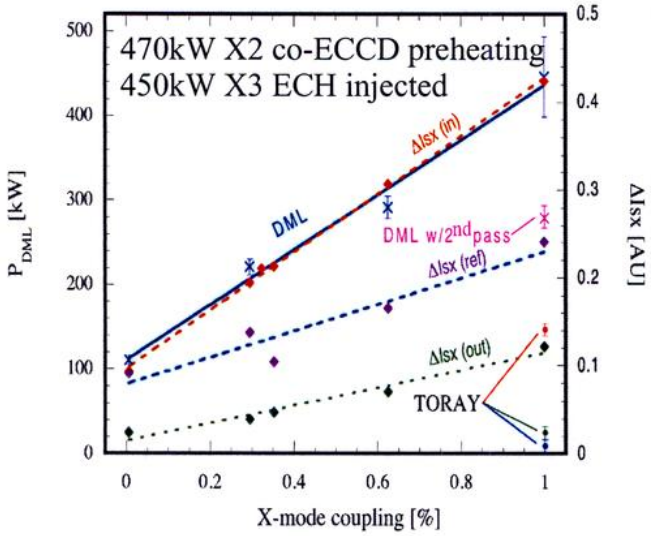

Fig. 2 The DML measured X3 absorbed power and change in pressure derived from the soft x-ray signal, ΔIsx, as a function of the X-mode coupling fraction. The X3 beam was swept off axis at the end of each shot. The ΔIsx gives an indication of the off-axis power absorption (out) and the second pass HFS launch absorption by inner wall reflection of the beam (ref) (see also DML w/2nd pass).

3. X3 absorption measurements

The mECH modulation frequency was 237Hz such that the modulation period was longer than the expected pitch angle scattering time and shorter than the electron energy confinement time [8]. The phase of the reconstructed signal was always found to be near 90 as expected for these conditions. The DML also measures correctly the X2 power (100% absorption) using the mECH technique with an X2 gyrotron. TORAY calculations are performed using time-averaged Thomson profiles to eliminate the influence of sawtooth fluctuations (typically over 200ms, i.e. 4 Thomson profiles).

In fig.2, the X3 absorption is shown to decrease approximately linearly with the fraction of X-mode coupling for the 3rd harmonic even though the total input power remains the same; indicating that the DML measured absorption is dominated by first pass absorption in spite of the global nature of the DML measurement. Secondly, since the co-ECCD X2 power remains essentially 100% absorbed at all times, the absorption effect is not significantly non-linear in X3 power at the injected power level of 470kW; or else, any non-linearity is saturated at even the lowest first-pass absorbed powers and the saturation mechanism is linear in power.

The X3 beam was swept off-axis at the end of each shot, after the mECH phase. The change in the density-normalized line-integrated soft X-ray signal is also shown in the figure and gives a rough indication of the on-axis first pass absorption, off-axis power absorption and on-axis second pass absorption (after reflection from the inner wall of the tokamak). This interpretation of the signal is supported by the mECH DML measurement for one polarization (see fig. 2) in which the mECH phase was moved to a later time in a second shot. This corresponds, essentially, to a HFS launch of the X3 beam since the first pass absorption at the launch angle is negligible (assuming $n_e T_e^2$ scaling of the optical depth for X3 using the local values of the Thomson profiles at the resonance).

Figure 3 shows the X3 absorption when increasing the X2 heating power. Three scans were performed: in co-ECCD, counter-ECCD and ECH X2. The power was varied (for P_{X2}>0.5MW) by increasing the number of gyrotrons. The temperature and density at the

absorption location varied accordingly. A clear excess in absorption is seen relative to the TORAY calculation; especially for co-ECCD X2 pre-heating. Nearly 3 times as much counter-ECCD X2 power is required to reach the same X3 absorption level as with co-ECCD X2. The minimum X2 input power necessary to provide 100% X3 absorption was somewhat less than the power of one X2 gyrotron.

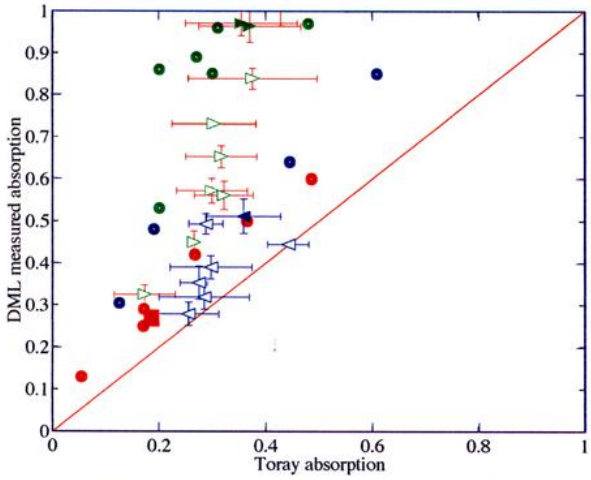

Fig. 3 DML measured X3 absorption versus TORAY (maxwellian) calculated absorption during co-ECCD (~20), counter-ECCD (~-20) and ECH power scans. Measured absorption is ~100% and exceeds TORAY calculations by up to a factor of 4 for co-ECCD X2 heating (for triangles - see text).

A scan of the X2 toroidal injection angle, with equal X2 and X3 powers (~470kW) was performed. The triangles in fig. 3 show the absorped powers for this scan. The filled points correspond to the shots of the toroidal angle scan which were at the same toroidal angles used in the power scan. They are seen to reproduce well the power scan data. It should be noted that during the toroidal scan the same X2 launcher was used for all angles, however the results at the optimum angles are quite reproducible using an upper lateral launcher.

In fig. 4a, the temperatures measured by Thomson scattering, T_e, the HFS ECE diagnostic, T_{ece}, and the hard x-ray camera, T_{photon}, are shown, during X2 heating alone (lower panel) and when X3 is added (upper panel). The photon temperature is calculated using a bi-maxwellian fit to the energy spectrum for a central chord of the camera: only the tail temperature is shown. For near ECH heating, all three diagnostics give similar results corresponding to the bulk electron temperature in X2; however, when X3 is added, the temperatures diverge indicating a non-maxwellian electron distribution. For counter- and especially co-ECCD, the temperatures are already divergent during the X2 only phase.

Figure 4b shows the energy integrated hard X-ray emission of the tail [4,6] and the fractional absorption of X3 during the same toroidal scan. A peaking of both measurements occurs near 22and there is a clear asymmetry of the peaks in the toroidal angle of X2. Full absorption of the X3 occurs during X2 co-ECCD while only about half of the X3 power is absorbed with optimum X2 counter-ECCD. The asymmetry is not as strong for the hard x-ray emissivity.

It is tempting to suggest that the electric field may play a role in the absorption of X3 in addition to the X2 injection angle. Asymmetric transmission has been observed on RTP [9] during incomplete absorption of first harmonic O-mode ECH, launched from the low field side, at similar densities and temperatures. In that experiment, Fokker Planck calculations showed symmetric peaking of absorption for ECH alone, with reduced absorption at near perpendicular angles (0 in our figures), and asymmetric peaking with the electric field added. The experimental data were in qualitative agreement with the asymmetry but no reduction of absorption was observed.

Nevertheless, it should be noted that the present experimental conditions are very different. Besides the obvious difference in propagation mode, here the X3 power is insufficient to produce a strong non-linear effect without X2 preheating; so, the X3 absorption is independently controlled by the X2 injection angle. Fokker Planck calculations including both frequencies are in progress; however, preliminary calculations suggest a subtle effect of the current drive on the profiles leading to an asymmetry, rather than a direct effect of the electric field.

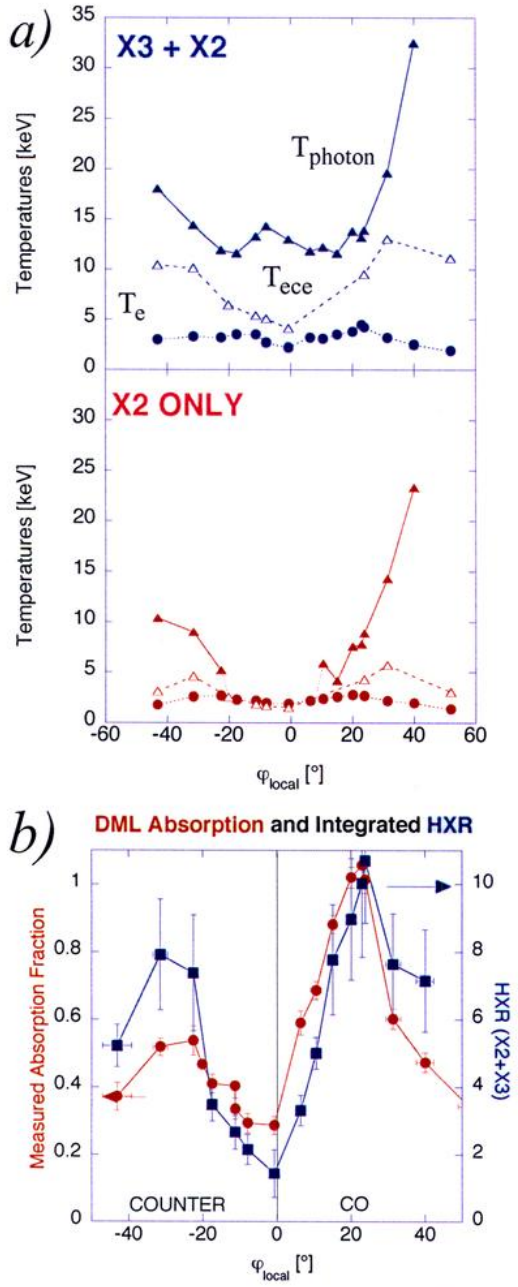

Fig. 4 a) Temperatures measured by Thomson scattering (dots), ece (open triangles) and a central chord of the hard x-ray camera (filled triangles) during a scan of the toroidal injection angle of 1 X2 gyrotron (P_{X2} = 470kW). b) Measured X3 absorbed power fraction (P_{X3} = 470kW) and the hard x-ray emissivity [6] for the same scan. The DML asymmetry is larger than for the hard x-rays; although, both peak near 22 . The X2 absorption is 100% except at largest angles.

4. Conclusions

X3 LFS launch provides new opportunities for heating of higher density plasmas in TCV if the hot electron tail of the distribution created by the X2 co-ECCD preheating can be maintained as the density rises past the X2 density cutoff; i.e., if the X3 absorption is sufficiently non-linear to self-sustain the tail. It should be noted that since the X2 launchers allow toroidal injection, the self-generation of the hot-electron tail with X3 alone may be possible and for strong enough X3 absorption with toroidal injection, X3 ECCD becomes a possibility. The mismatch in resonance location between the X2 and X3 and the fact that the X3 is not fully absorbed by the bulk allows the selection of the energy range over which the remaining X3 is absorbed. A similar situation should exist using only one frequency but 2 resonances in the plasma (e.g. 2^{nd} and 3^{rd} harmonics). With one resonance to the HFS of the magnetic axis and the other to the LFS, a magnetic field sweep will move the 2^{nd} harmonic resonance located at ρ_2 outward in ρ and the 3^{rd} harmonic resonance at ρ_3, inward. If ECCD is being used, when the field approaches the appropriate value such that ρ_3 ρ_2, there should be a transfer of the absorption from the HFS 2^{nd} to the LFS 3^{rd} harmonic. If in addition, the power is high enough to give non-linear 3^{rd} harmonic absorption then the density can be ramped to a higher value than previously possible. Since the poloidal location of absorption will change to the LFS, particle trapping should change suddenly and drastically providing a method for testing trapped particle effects (for example, on the efficiency of ECCD) in one shot.

Acknowledgment: This work was partly supported by the Swiss National Science Foundation.

[1] HOFMANN, F. and TONETTI, G., Nucl. Fusion **28** (1988) 1871.
[2]HOFMANN, F., et al., invited talk, this conference
[3]GOODMAN, T.P., et al., in Proc. 19th SOFT, Lisbon, (1996) 565.
[4] ALBERTI, S., et al., 18 IAEA Fusion Energy Conference, Sorrento, Italy 4-10 October 2000.
[5] PIETRZYK, Z.A., et al., Phys. of Plasmas 7 (2000) 2909
[6] CODA, S., This conference
[7] BLANCHARD, P., This conference
[8] MANINI, A., et al., CRPP Internal Report LRP 664/00 March (2000)
[9] PEETERS, A.G., et al., Plasma Phys. Control. Fusion **37** (1995) 525-540.

A SEMI-LAGRANGIAN METHOD FOR THE RESOLUTION OF A DRIFT-KINETIC EQUATION APPLIED TO ITG STUDIES

V. Grandgirard, P. Bertrand[1], G. Depret[2], X. Garbet[2], A. Ghizzo[1], G. Manfredi[1], O. Sauter, T.M. Tran[3], J. Vaclavik, L. Villard

CRPP, Association Euratom-Confédération Suisse, EPFL, 1015 Lausanne, Switzerland.
[1]*LPMIA, Université Henri Poincaré-Nancy 1, BP 239, 54506 Vandoeuvre-les-Nancy, France.*
[2]*DRFC, Association Euratom-CEA, CEA Cadarache, 13108 St Paul-lez-Durance, France.*
[3]*SIC, EPFL, 1015 Lausanne, Switzerland.*

1 Introduction

Ion turbulence is presumed to play a non negligible role in anomalous transport. Several gyrokinetic Particle-In-Cell (PIC) codes [1] have already been developed to study the plasma instabilities caused by ion temperature gradients (ITG). The drawback of this kind of codes is the numerical noise. In this paper we solve a 4D non-linear drift-kinetic Vlasov problem by using a noiseless approach, called semi-Lagrangian method [2], which has already been applied to passing ion driven modes [3] in 2D and linear trapped ion modes [4]. We present the physical model used, the basics of the method coupled with a time-splitting algorithm and the first results obtained.

2 Drift kinetic model : global description

Let the cylindrical coordinates be $(r, \theta, z) = (\vec{R}, z)$. The ion distribution function f should normally depend on these three space variables and three velocity variables. We consider a uniform magnetic field : $\vec{B} = B_z \vec{e_z}$. Besides, we neglect the Larmor radius and so the particle trajectories are identical to the guiding-center trajectories. Then f becomes a 4D function and the particle motion can be simply described by the following equations :

$$\dot{\vec{R}} = v_{\vec{GC}} = \frac{\vec{E} \times \vec{B}}{B^2} \quad ; \quad \frac{dz}{dt} = v_{\parallel} \quad ; \quad \dot{v_{\parallel}} = \frac{q}{m} E_z \tag{1}$$

The drift-kinetic equation which couples the $\vec{E} \times \vec{B}$ motion across the magnetic field to the motion parallel to the magnetic field reads :

$$\frac{\partial f}{\partial t} + v_{\vec{GC}} \cdot \vec{\nabla}_{\perp} f + v_{\parallel} \frac{\partial f}{\partial z} + \dot{v_{\parallel}} \frac{\partial f}{\partial v_{\parallel}} = 0 \tag{2}$$

We assume that there is no fluctuating magnetic field and we use the electrostatic approximation to compute the electric field : $\vec{E} = -\vec{\nabla}\Phi$ where the scalar Φ represents the electric potential. This electric potential is determined by using the quasi-neutrality equation : $n_e - \langle \delta n_e \rangle_z = Z(n_i - \langle \delta n_i \rangle_z)$ where n_i and n_e are respectively the ion and the electron density, the symbol δ denotes a perturbation and $\langle . \rangle_z$ represents the average on the magnetic field lines. The ion density is given by : $n_i(r, \theta, z, t) = \int dv_{\parallel} \, f(r, \theta, z, v_{\parallel}, t)$ and in a first approximation we assume that the mobile electrons respond adiabatically

to the low frequency micro-instabilities and therefore follow a Boltzmann distribution, i.e : $n_e = n_0 \exp\left(e\frac{\Phi-\langle\Phi\rangle_z}{T_e}\right) \approx n_0\left(1+e\frac{\Phi-\langle\Phi\rangle_z}{T_e}\right)$ (with $e\Phi$ assumed $\ll T_e$). If we write f like $f = f_M + \delta f$ where δf is the perturbation and f_M a Maxwellian chosen such that $\int f_M\, dv_{\|} = n_0$, then by using the previous n_e adiabatic expression, the electric potential Φ can be written like :

$$\Phi(r,\theta,z,t) = \frac{T_e(r)}{e\, n_0(r)}\left[\int (f - \langle f\rangle_z)\, dv_{\|}\right] \tag{3}$$

The drift-kinetic model is thus given by the three previous non-linear equations.

3 Semi-Langrangian method

The semi-Lagrangian method couples the Lagrangian and the Eulerian point of view. Indeed this method consists, like the Eulerian method, in the direct solving of the Vlasov equation and to use, like a Lagrangian method, the fact that the distribution function f is constant along its characteristics.
Let $\vec{\Gamma}(t)$ be a particle position at the time t, then $\frac{df}{dt}\left(\vec{\Gamma}(t),t\right) = 0$ according to the characteristic equation definition (1) and the drift-kinetic equation (2). So the distribution function can be computed at each time step on the same fixed grid, by using : $f\left(\vec{\Gamma}_i(t_n+\Delta t), t_n+\Delta t\right) = f\left(\vec{\Gamma}(t_n,\vec{\Gamma}_i,t_n+\Delta t),t_n\right)$ where $\vec{\Gamma}(t_n,\vec{\Gamma}_i,t_n+\Delta t)$ represents the solution of the characteristic at the time step t_n and whose value is equal to $\vec{\Gamma}_i$ at the time $t_n+\Delta t$. So the method consists first in finding the foot of the characteristic at the time t_n : $\vec{\Gamma}(t_n,\vec{\Gamma}_i,t_n+\Delta t)$. Then to compute $f\left(\vec{\Gamma}(t_n,\vec{\Gamma}_i,t_n+\Delta t),t_n\right)$ by interpolation (performed in our case with cubic splines), because at this time the distribution function is known over the whole fixed grid. The fact of keeping a fixed grid avoids the numerical noise which appears in PIC codes due to the finite number of particles. In contrast to most of PIC methods the semi-Lagrangian resolution is made on the full f, but the resolution of the 4D drift-kinetic equation can be simplified.

4 Time splitting method

In this uniform field case, the Liouville theorem, which characterizes the incompressibility of the gyrocenter orbits, is verified, i.e. : $\vec{\nabla}\cdot v_{\vec{GC}} + \frac{\partial v_{\|}}{\partial z} + \frac{\partial \dot{v_{\|}}}{\partial v_{\|}} = 0$. With this property the drift-kinetic equation (2) can be written in its conservative form:

$$\frac{\partial f}{\partial t} + \vec{\nabla}\cdot(v_{\vec{GC}} f) + \frac{\partial}{\partial z}\left(v_{\|} f\right) + \frac{\partial}{\partial v_{\|}}\left(\dot{v_{\|}} f\right) = 0 \tag{4}$$

This allows us to use a time-splitting method, i.e solving (2) in 3 steps, by splitting between space and velocity coordinates into the 2D advection equation $\frac{\partial f}{\partial t} + \vec{\nabla}\cdot(v_{\vec{GC}} f) = 0$ and the two 1D advection equations $\frac{\partial f}{\partial t} + v_{\|}\frac{\partial f}{\partial z} = 0$ and $\frac{\partial f}{\partial t} + \dot{v_{\|}}\frac{\partial f}{\partial v_{\|}}$. Let $\hat{r\theta}$ denotes the shift operator in (r,θ) direction over a full time step Δt, corresponding to the 2D advection resolution, and let $\hat{z}$ and $\hat{v_{\|}}$ denote the shift operators respectively in z and $v_{\|}$

directions, corresponding to the 1D advections in z and $v_{||}$ directions. To conserve a second order scheme it is necessary to keep the symmetry in the splitting algorithm. In our case the most efficient algorithm in terms of number of operations can be summarized by $\hat{v_{||}} \frac{\hat{z}}{2} \hat{Q} \hat{r\theta} \hat{Q} \frac{\hat{z}}{2} \hat{Q}$, where the term $\frac{1}{2}$ denotes that the shift is effected over half a time step and where $\hat{Q}$ denotes symbolically that at this point the quasi-neutrality equation is solved to compute the electric potential and then the electric field.

5 Results

In the following, the temperature is normalized to T_{e0}, where T_{e0} is defined such that $T_e(r_0)/T_{e0} = 1$ (with r_0 a reference point). The time is normalized to Ω_0^{-1}, where $\Omega_0 = \frac{q_i B_0}{m_i}$ is the ion cyclotron frequency. The velocity is normalized to the sonic velocity $c_s = \sqrt{\frac{T_{e0}}{m_i}}$ and the electric potential to $\frac{T_{e0}}{q_i}$. The initial distribution function is given by : $f(r, \theta, z, v_{||}, 0) = f_M(r, v_{||}) \times (1 + \epsilon \cos(k_z z + m\theta))$ where ϵ is the perturbation amplitude. We assume no perturbation at the boundaries in r and $v_{||}$ directions and periodic conditions in θ and z directions. The electron temperature is fixed constant while the ion temperature (fig 1.a) and the density profiles (fig 1.b) are chosen such that the $\eta_i = d\log T_i / d\log n_0$ is superior to 2 in a sufficiently large region to develop instabilities (fig 1.c).

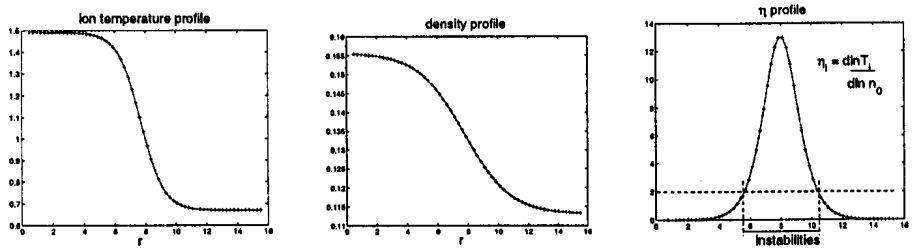

(a) (b) (c)

Figure 1: (a) Ion temperature profile : $T_i(r)$. (b) Density profile : $n_0(r)$. (c) η_i profile.

The results presented here correspond to a simulation with a (32 × 32 × 32 × 64) discretisation, with $2 \leq r \leq 16.5$, $0 \leq \theta \leq 2\pi$, $0 \leq z \leq 1500$ and $-6\, v_{Thi} \leq v_{||} \leq 6\, v_{Thi}$ (where v_{Thi} is the ion thermal velocity). The modes in θ and z directions are initialized to $m = 4$ and $n = 1$, with a perturbation amplitude $\epsilon = 10^{-4}$.

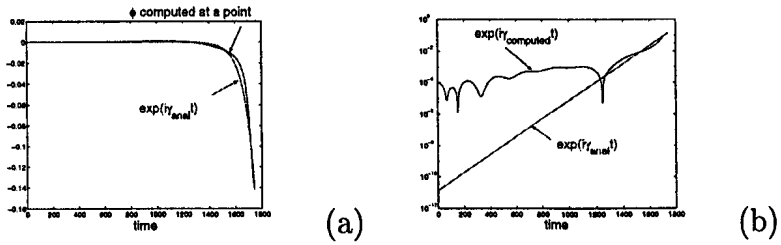

(a) (b)

Figure 2: Computed and analytical γ : (a) linear scale, (b) semi-logarithmic scale .

If we consider the time evolution of Φ at a fixed point, we notice an exponential increase in the linear phase (fig 2) which is in a good agreement with the analytical growth rate

: $\gamma \sim \left[(k_z v_{thi})^2 \omega_T^\star\right]^{1/3}$. But if we continue the simulation, we do not succeed in obtaining a saturation in the non-linear phase.

If we examine the solution at different times (fig 3), we see that it is due to the fact that the mode $m = 4$ peaks more and more with the tendency to converge to a radial δ function (fig 3.d), for which it is difficult to have a sufficient discretization after a certain time.

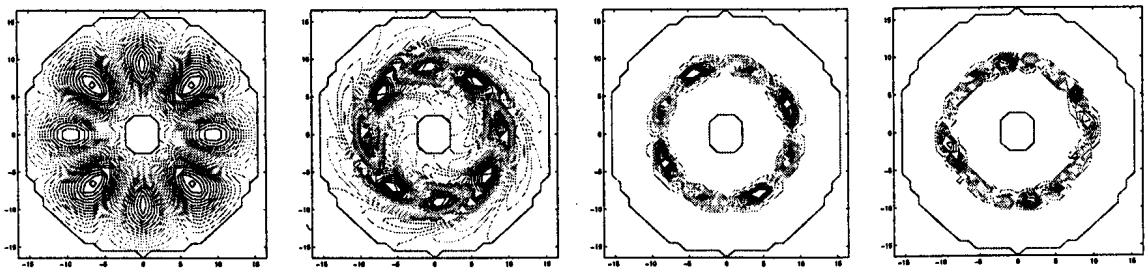

(a) (b) (c) (d)

Figure 3: Evolution of the electric potential in (x, y) cross-section : (a) initial time, (b) $t = 232$, $t = 1480$ and $t = 1530$.

However, preliminary results show that taking into account the polarization term in the quasi-neutrality equation ensures a regularization of the solution. In this case Φ is no more computed with the analytical expression (3), but by solving (Fourier in the 2 periodic directions and finite difference in r) the following Poisson equation : $-\nabla_\perp \cdot \left[\frac{n_0(r)}{B\Omega_0}\nabla_\perp \Phi\right] + \frac{e\, n_0(r)}{T_e(r)}\Phi = n_i - n_0$. If we compare the Φ map at the time 1530 (fig 4) with the one previously obtained (fig 3.d), we notice that the mode width stays finite.

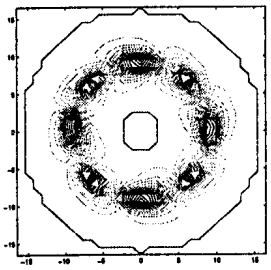

(a)

Figure 4: $\Phi(x, y)$ at time $t = 1530$

6 Conclusion

We have shown that a semi-Lagrangian method can correctly describe the linear phase of ITG for a cylindrical plasma column confined by a uniform magnetic field, even with relatively few grid points. However some problems are still present in the non-linear phase, which prevent the reliable computation of the saturation phase. In the future, we plan to address this issue in greater depth and then to improve this model to a gyro-kinetic model and to take into account a non-uniform magnetic field.

References

[1] T.M. Tran et al., 1999 *Proc. Varenna-Lausanne Int. Workshop*, ISPP-18.

[2] Manfredi G et al., 1996 *Phys. Plasmas*, **3** 202.

[3] Sonnendrücker E. et al., 1999 *Journal of Comput. Phys.*, **149**, 201-220.

[4] Depret G. et al., 2000 *Plasma Phys.*, **42** 949.

THEORETICAL MHD LIMITS IN TOKAMAKS WITH A SEPARATRIX

S.Yu.Medvedev[1], T.C.Hender[2], O.Sauter[3], L.Villard[3]

[1]*Keldysh Institute, Russian Academy of Sciences, Moscow, Russia*
[2]*Euratom/UKAEA Fusion Association, Culham Science Centre, Abingdon, UK*
[3]*CRPP, Association Euratom-Confédération Suisse, EPFL, Lausanne, Switzerland*

1 Numerical modelling The presence of a magnetic field separatrix influences tokamak stability in the framework of ideal MHD. Full separatrix geometry divertor tokamak plasmas and doublet configurations with internal separatrices have been the subject of intensive numerical studies during the last seven years using the KINX equilibrium and stability code family [1] developed for this purpose.

The finite element formulation used in the KINX code allows for a consistent treatment of the full separatrix geometry, including the case of doublet configurations having two magnetic axes and an internal separatrix. Numerical destabilization elimination and ballooning factor extraction [2] recently specialized to the separatrix case considerably improve the code convergence properties, especially when there are many rational surfaces in plasma.

2 Beta limit The limiting beta values in tokamaks are well described by the theoretical Troyon-Sykes scaling [3, 4] $\beta[\%] = \beta_N I_N$, $\beta_N \simeq 4$, where $\beta = 2\mu_0 \int pdV/(VB^2)$, $I_N = I[MA])/(a[m]B[T])$, I is the plasma current, a the plasma minor radius and B the vacuum toroidal field in the plasma center $R = R_c$.

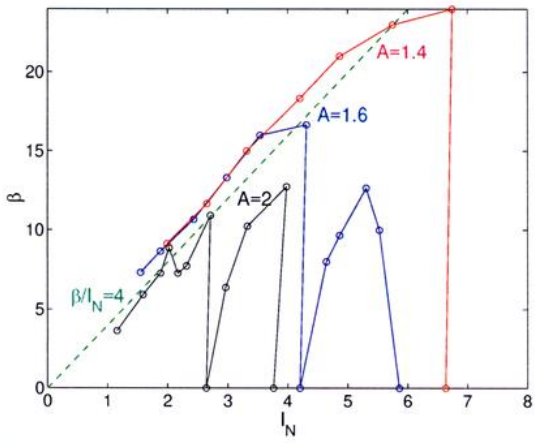

Fig.1 Combined ballooning mode and $n = 1$ external kink limiting β for different aspect ratios, elongation $\kappa = 1.6$, triangularity $\delta = 0.3$, $q_0 > 1$

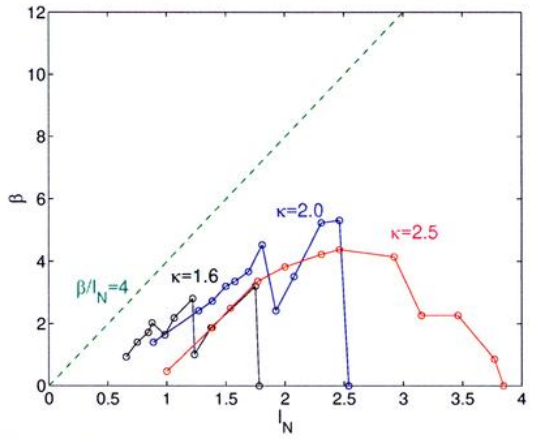

Fig.2 Combined ballooning mode and $n = 1$ external kink limiting β for different elongations, aspect ratio $A = 4$, triangularity $\delta = 0.3$, $q_0 > 1$

In Fig.1 limiting values of β for the aspect ratio range from 2 to 1.4 with conventional shape, elongation $\kappa = 1.6$ and triangularity $\delta = 0.3$ are presented [5]. The axial safety factor value $q_0 > 1$ was assumed. The "ravines" in the $\beta(I_N)$ dependence are characteristic to the limiter plasma shape for the aspect ratio values $A \gtrsim 2$. They are connected with the values of the boundary safety factor q_s just below the integers $2, 3, 4 \ldots$, where external $n = 1$ kink mode become unstable especially if current density is high near the boundary.

Taking into account the separatrix at the boundary gives more realistic beta limit predictions without this artificial behavior. There is also an overall beta limit enhancement due to separatrix stabilizing influence connected with the presence of rational magnetic surfaces in plasma without decreasing the total current. The detailed calculations of β limits for L-mode and H-mode ITER configurations [6] showed that external kink modes are less sensitive to the plasma profiles when the plasma boundary is close the separatrix.

For all cases the beta limits are higher with separatrix at the boundary. From $\beta = 5.8\%$ for a plasma boundary defined by $\psi_{boundary}/\psi_{separatrix} = 0.95$ the limit raises to $\beta = 6.3\%$ for $n = 1$ external kink mode in the L-mode equilibrium. The difference is higher for the H-mode case with higher current density near the boundary: 5.0% vs. 6.8%.

In Fig.2 the limiting β versus I_N are also shown for the conventional limiter plasma shape with elongation κ from 1.6 to 2.5 [7]. These results are also consistent with the experimental data and the numerical results from [8]. Both for low aspect ratio $A \lesssim 1.5$ and higher elongation $\kappa \gtrsim 2$ cases the "ravines" are less pronounced and even absent due to higher shear at the boundary – the effect similar to the stabilizing separatrix influence. However an enhancement of the current limit, which is set by external kink modes at low q_s at the boundary, can be expected for the separatrix plasma.

3 Current limit For high aspect ratio circular cross-section plasma the following sufficient condition for the external kink mode instability can be written [9]: $m-1 < nq < m$ everywhere in plasma. For $n = 1, m = 2$ and $q_0 > 1$ it gives the current limit defined by $q_s = 2$. For low aspect ratio and/or high elongation the maximal current corresponds to $q_s > 2$ for the limiter plasma case.

However for plasma with separatrix at the boundary, $q_s \to \infty$, the results of the computations give the limiting current values quite close to the limits for equivalent conventional shape plasmas provided that $q_0 > 1$. In particular it means that the enhancement of I_N with decreasing aspect ratio is reduced from a $1/(A-1)$ dependence when $q_0 > 1$ [5]. On the other hand the results from START spherical tokamak [10] demonstrated values of $\beta > 35\%$ and $I_N \simeq 8$ for $A \simeq 1.4$, which are higher than the theoretical limits at $q_0 > 1$ but consistent with the β and current limit predictions for $q_0 < 1$ with separatrix at the boundary [12].

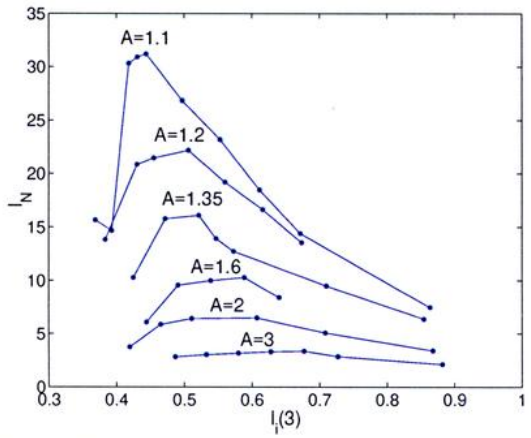

Fig.3 External kink limiting normalized current for different plasma profiles at $\beta = 0$; $\kappa = 1.8$, $\delta = 0.5$ with separatrix

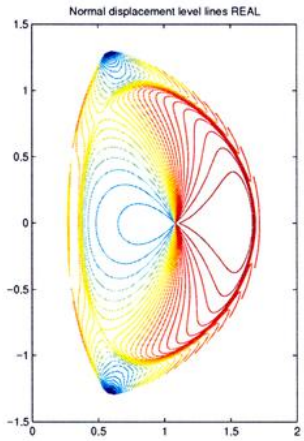

Fig.4 Toroidal $n = 1$ kink mode normal displacement level lines. $l_i = 0.57, I_N = 14.3$, $q_0 = 0.8, q_{95} = 1.33$, $\omega^2/\omega_A^2 = -3.0 \cdot 10^{-3}$

For $q_0 < 1$ toroidal $n = 1$ kink modes set a current limit due to the coupling of surface wave mode with $m = [q_s] + 1$ to the internal $m = 1$ mode [11]. The presence of the separatrix eliminates this resonant toroidal feature and opens the way to increase the normalized current in configurations with $q_0 < 1$. Fig.3 shows the results of the computations of the $n = 1$ current limit varying the internal inductance $l_i(3) = 2\int B_p^2 dV/(R_c I^2)$ of the current profiles in low β equilibria for different aspect ratios and the same separatrix cross section. The increase of the limiting normalized current values is quite strong compared to the $q_0 > 1$ case (Fig.1). The maximal current corresponds to $q_0 < 1$ and is set by the non resonant analog of the toroidal kink mode (Fig.4).

The results of the computations seems (provided not very strong dependence on the current profile family [12]) to suggest the restoration of the convenient scaling for the maximal current $I_N \simeq 5/2(1+\kappa^2)/q(A-1)$, $q = 2$ [5]. However the current limit for

very low aspect ratio $A = 1.1$ is behind such a scaling. Moreover recent computations indicate that the maximal current values from the Fig.3 does not significantly change for elongations κ from 1.5 to 2.5 (at least for low aspect ratio $A \lesssim 2$) reflecting the toroidal kink stability deterioration with increasing elongation [11].

4 Low aspect ratio For low aspect ratio plasmas the current limit scaling with aspect ratio implies very high β limits provided that the ballooning stability limit $\beta_N \simeq 4$ holds also for $q_0 < 1$.

Optimization of the pressure profile to ballooning modes at all radii, keeping the q profile constant, demonstrated that ballooning stable equilibria with $\beta_N \gtrsim 4$ can be obtained even at very low q_{95} with p' localized near the boundary [12]. An example of such equilibrium profiles are presented in Fig.5. Internal pressure driven kink modes are stable because of low pressure gradient inside the $q = 1$ surface. This equilibrium is unstable against external $n = 1$ kink mode (Fig.6) which can be stabilized by with the wall at $a_w/a = 1.6$. It corresponds to higher current limit taking into account the wall stabilization. Reducing the value of I_N, which is close to the $\beta = 0$ current limit (Fig.3), it is possible to achieve low-n stability with no wall at $\beta = 107\%$, $I_N = 24.1$ [13].

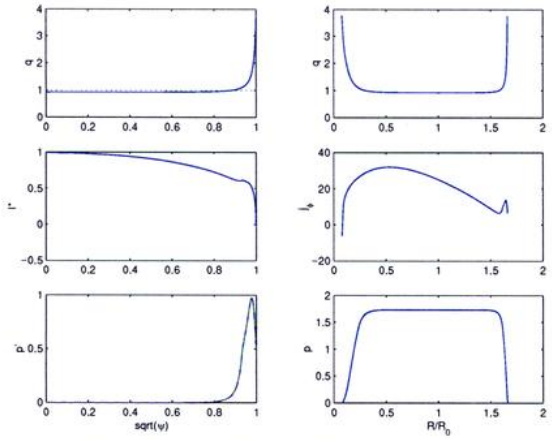

Fig.5 Profiles of the ballooning marginally stable equilibrium. $A = 1.1$, $\beta = 167\%$, $I_N = 30.2$, $l_i = 0.41$, $q_0 = 0.93, q_{95} = 1.61$

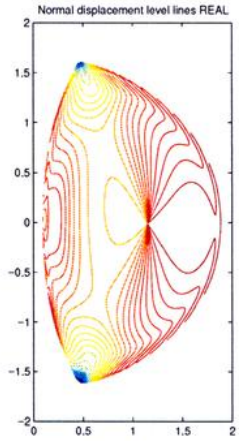

Fig.6 External $n = 1$ *kink mode normal displacement level lines for the equilibrium corresponding to Fig.5.* $\omega^2/\omega_A^2 = -5.0 \cdot 10^{-2}$

The free boundary equilibrium and stability studies were also performed for the high $\beta_N \simeq 8$ bootstrap current driven equilibria in the second ballooning stability regime. Conducting wall is needed to maintain the external kink stability of such equilibria. Proximity of the separatrix to the plasma boundary and increased triangularity were found to be stabilizing for external kink modes, though both these effects are decreasingly pronounced for higher-n modes, which usually set the limiting wall position [14].

5 Doublets The stabilizing influence of the separatrix on external kink modes applies also to doublet plasmas. However no significant changes both in β and current limits were found for low current density outside the separatrix compared to the single magnetic axis plasma with the separatrix at the boundary [15]. In particular no substantial stabilizing influence of the current-less mantle plasma outside the separatrix on the external kink limits was found [16]. The reason for that could be very high values of q in the mantle with higher order rational surfaces having a weak effect on external kink stability.

The vertical stability of a doublet configuration is close to a single axis equilibrium equivalent to one half of the doublet both in terms of marginal wall position and resistive wall growth rates.

Doublet configurations provide the unique opportunity of self-consistent treatment of the finite current density at the separatrix and the plasma outside separatrix in the framework of ideal MHD. In [17, 18] the case of H-mode pressure profile having a maximal gradient at the separatrix was considered and the KINX code was extended to the divertor configurations with open magnetic field lines. For the doublet configurations current

density and pressure profile variation in relatively thin plasma layer outside the separatrix can influence global external kink mode stability and considerably change the β limit. The conclusions for the divertor configurations strongly depend on the choice of boundary conditions at the open field lines.

Acknowledgements This work was partly funded by the UK Department of Trade and Industry and EURATOM. The CRPP authors were supported in part by the Swiss National Science Foundation.

References

[1] L.Degtyarev *et al.*, *Comput. Phys. Comm.* **103**(1997)10

[2] R.Gruber *et al.*, *Comput. Phys. Commun.* **24**(1981)363

[3] F.Troyon *et al.*, *Plasma Phys. and Contr. Fusion* **26**(1984)209

[4] A.Sykes *et al.*, *Proc. of the 11th Europ. Conf. on Contr. Fusion and Plasma Phys.* **2**(1983)363

[5] S.Bespoludennov *et al.*, *Sov. J. Plasma Phys.* **12**(1986)771

[6] M. Rosenbluth *et al.*, *Proc. 5th Int. Conf. on Plasma Phys. and Controlled Nuclear Fusion Research, Sevilla, Spain, September-October 1994* , IAEA, Vienna (1995) Vol.2, 517

[7] L.M.Degtyarev *et al.*, Numerical modelling of equilibrium and stability of toroidal plasma, Ed.: V.D.Shafranov, Moscow 1989

[8] F.Hofmann *et al.*, Phys. Rev. Lett. **81**(1998)2918

[9] L.E.Zakharov, In: Reviews of Plasma Physics, Ed.: B.B.Kadomtsev, Consultants Bureau, N.Y., vol.7, p.18, 1981

[10] M.Gryaznevich *et al.*, *Proc. of the 24th Europ. Conf. on Contr. Fusion and Plasma Phys.* **21A** Part I (1997)245

[11] A.D.Turnbull, F.Troyon, *Nuclear Fusion* **29**(1989)1887

[12] S.Medvedev *et al.*, Proc. 25th EPS Conference on Controlled Fusion and Plasma Physics,Praha, ECA Vol. 22C, page 2022 (1998)

[13] T.C.Hender *et al.*, *Phys. Plasmas* **6**(1999)1958

[14] S.Medvedev *et al.*, Proc. 27th EPS Conference on Controlled Fusion and Plasma Physics, Budapest, P4-076 (2000)

[15] L.Degtyarev *et al.*, 21th EPS Conf. on Controlled Fusion and Plasma Phys., Montpellier, Proc. Contrib. Papers vol.II (1994)556

[16] L.Degtyarev *et al.*, 22th EPS Conf. on Controlled Fusion and Plasma Phys., Bournemouth, Proc. Contrib. Papers vol.I (1995)217

[17] L.Degtyarev *et al.*, 23th EPS Conf. on Controlled Fusion and Plasma Phys., Kiev, Proc. Contrib. Papers vol.III (1996)1191

[18] L.Degtyarev *et al.*, 23th EPS Conf. on Controlled Fusion and Plasma Phys., Berchtesgaden, Proc. Contrib. Papers vol.II (1997)845

[19] S.Medvedev *et al.*, Proc. 26th EPS Conference on Controlled Fusion and Plasma Physics, Maastricht, ECA Vol. 23J (1999)141 ; (http://epsppd.epfl.ch)

Topology of Magnetic Field Strength Surfaces and Particle Confinement in Mirror-Type Stellarators

M.I.Mikhailov[1], M.Yu.Isaev[1], J.Nührenberg[2], A.A.Subbotin [1], W.A.Cooper[3], M.F.Heyn[4], V.N.Kalyuzhnyj[5], S.V.Kasilov[5], W.Kernbichler [4], V.V.Nemov[5], M.A.Samitov[6], V.D.Shafranov[1]

[1] *Russian Research Centre "Kurchatov Institute", 123182, Moscow, Russia*

[2] *Max-Plank-Institute für Plasmaphysik, Teilinstitut Greifswald IPP-EURATOM Association, D-17491 Greifswald, Germany*

[3] *Centre de Recherches en Physique des Plasmas, Association Euratom-Confédération Suisse, Ecole Polytechnique Fédérale de Lausanne, PPB, 1015 Lausanne, Switzerland*

[4] *Institut für Theoretische Physik, Technische Universität Graz, Graz, Austria*

[5] *Institute of Plasma Physics, National Science Center "Kharkov Institute of Physics and Technology", 61108, Kharkov, Ukraine*

[6] *Moscow State Engineering and Physics Institute, Moscow, Russia*

Abstract. Helical magnetic systems in which the lines of the modulus of the magnetic field strength B remain constant in the direction of the poloidal angle variable are investigated to clarify in more detail the connection between the shape of the magnetic surfaces and the topology of the B = constant surfaces on one the one hand and particle confinement on the other. The possibilities to fulfill the pseudosymmetry condition as well as the condition that the second adiabatic invariant $J_{||}$ forms closed contours are investigated numerically for almost zero and finite β values.

1. Introduction. As was shown in Ref. [1], the fulfillment of the quasi-isodynamicity (qi) condition in configurations for which the lines B=constant align with those of the direction of variation of the poloidal angle on magnetic surfaces leads to good particle confinement. Only the particles that are near trapped-transition boundaries can leave the plasma volume after a large number of changes of direction in the motion. The existence of such particles is closely connected with the presence of local maxima of B, i.e. islands of lines B=constant on the magnetic surfaces. The possibility to eliminate such particles is investigated numerically in the present paper. As a first step, the optimisation of the configuration with respect to pseudosymmetry (ps) [2] is undertaken and the confinement properties of the ps configuration is studied through the calculation of the second adiabatic invariant contours and more directly with the computation of the collisionless α-particles lost. It is shown that the fulfillment of the ps condition itself is not sufficient for good particle confinement. Therefore, as a next step, the optimisation toward the poloidal closure of the $J_{||}$ contours is performed. In addition, the effect of finite β on the shape of the magnetic field strength surfaces and the particle confinement is studied. Some results on calculations of neoclassical diffusion are presented for the configurations considered.

2. Optimisation toward pseudosymmetry. The initial boundary for the optimisation toward ps was obtained from that of W7-X [3] by changing the number of periods from $N = 5$ to $N = 6$ and by exchanging the six-period bumpy magnetic field component with a three times periodic term. In this case the extrema of the magnetic

field strength should be located at equivalent positions, all exhibiting small curvature of the magnetic axis. The pressure gradient was taken to be very small, $\beta \approx 0.05\%$. The behaviour of B=constant lines in Boozer coordinates at 1/3 and 3/4 of the minor plasma radius of the ps-optimised configuration is shown in Fig.1. Direct calculations of collisionless α-particle loss have shown that the fulfillment of ps condition itself does not improve the particle confinement: the bulk of the reflected particle fraction is lost in a short time. Numerical calculations have shown that the contours of the second adiabatic invariant $J_{||} = \int v_{||} dl$ are open which leads to the particle loss. Line 1 in Fig. 2 shows the radial (with s the normalixed flux variable) dependence of the coefficient $\epsilon_{eff}^{3/2}$ for the ps-optimised configuration. This quantity characterises the strength of the $1/\nu$ transport [4]. For a corresponding standard stellarator the $\epsilon_{eff}^{3/2}$ value turns out to be $0.01 \div 0.03$. So, the results obtained are only slightly better than those for the standard stellarator.

3. Optimisation toward closure of the $J_{||}$ contours and finite β effect. In addition to the ps condition, the requirement of closure of the $J_{||}$ contours was implemented in the optimisation procedure. As in the previous step, the β value was $\beta \approx 0.05\%$. Due to the different penalty function, the optimisation leads to a configuration with a dominating six-period bumpy component of the field strength and a different geometry of the magnetic axis (see Fig. 3). It is seen from Fig. 4 that in this configuration the lines B=constant have a similar form for almost all values of B, in contrast to the initial one (see Fig. 1). Fig. 5 demonstrates the behaviour of $J_{||}$ contours for trapped particles with different values of $B_{reflect}$ for that part of the period near the minimum of B. It is observed that the function $< J_{||} >_\theta$ has a minimum near the magnetic axis for this configuration with small β. This corresponds to convex B=constant surfaces, as is seen from Fig. 6. The minimum of $< J_{||} >_\theta$ is very shallow, so that small deviations from the qi condition can create open $J_{||}$ contours.

In Fig. 7, the contours of $J_{||}$ are shown for $\beta = 5\%$. It is seen that now $J_{||}$ has a maximum near the magnetic axis. It corresponds to the creation of an absolute minimum of B due to the diamagnetic effect and to the transition from convex to concave surfaces B=constant for moderate values of B (Fig. 8). Here, the maximum of $J_{||}$ is strong, so that even large deviations from qi can conserve the closure of the $J_{||}$ contours. The result of $\epsilon_{eff}^{3/2}$ calculations for $\beta = 5\%$ is shown in Fig. 2, too, line 2.

The transition from a minimum of $J_{||}$ near the magnetic axis for small β to a maximum of this quantity for $\beta \approx 5\%$ can lead to the deterioration of particle confinement for intermediate β values, when $< J_{||} >_\theta$ becomes independent of the plasma radius. This really occurs, as is seen from Fig. 9. Further optimisation is required for systems with finite β to clarify the possibility to confine all reflected particles in configurations without a local maximum of B on the magnetic surfaces.

Conclusions. Numerical investigations have shown that the ps condition can be fulfilled with high accuracy in the whole plasma volume. The fulfillment of the ps condition itself is not enough for improvement of particle confinement. The closure of the $J_{||}$ contours is defined both by radial dependence of $< J_{||} >_\theta$ and by the accuracy of the fulfillment of the qi condition.

Acknowledgements. This work was supported by INTAS Grant No 99-00592, by Russian-Germany agreement WTZ-V RUS-563-98, by Russian Federal program on sup-

port of leading scientific school, Grant No 00-15-96526, by Russian Fund for Basic Research, Grant No 00-02-17105, by the Fonds National Suisse de la Recherche Scientifique, by the Association EURATOM-OEAW and by Austrian Academy of Sciences.

References

[1] S.Gori, W.Lotz, J.Nührenberg *Theory of Fusion Plasmas (International School of Plasma Physics)*, Bologna: SIF, (1996) 335.

[2] M.I.Mikhailov, W.A.Cooper, M.Yu.Isaev , et. al., *Theory of Fusion Plasmas (International School of Plasma Physics)*, Bologna: SIF, (1998) 185.

[3] W.Lotz, J.Nührenberg, C.Schwab. *Plasma Phys. and Contr. Nucl. Fus. Res., Washington 1990,* IAEA, Vienna 1991, **2**, 603.

[4] V.V.Nemov, S.V.Kasilov, W.Kernbicheler, M.F.Heyn, *Phys. Plasmas* **6** (1999) 4622.

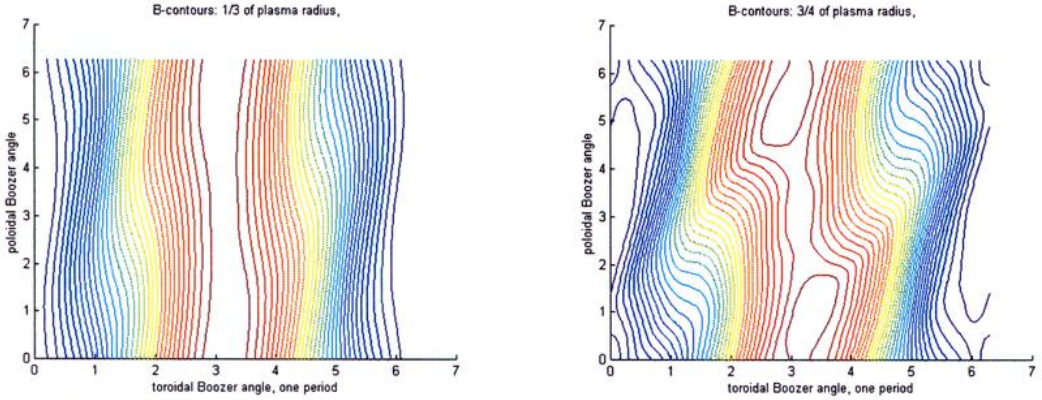

Fig. 1. B=constant lines on the inner (left) and outer (right) magnetic surfaces for optimized to PS configuration.

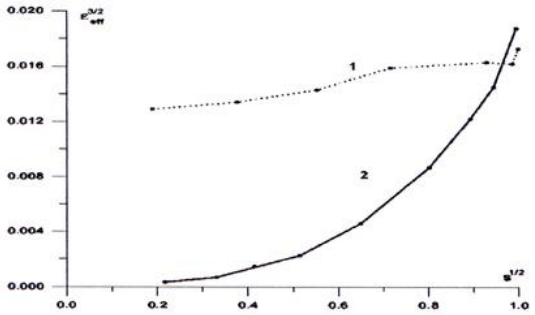

Fig. 2. Effective ripples amplitude for small β PS (line 1) and β=5% $J_{||}$ optimized configurations.

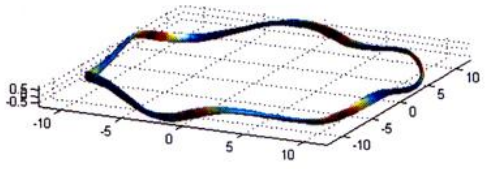

Fig. 3. Inner magnetic surface for optimized to PS and to closedness of $J_{||}$ contours configuration.

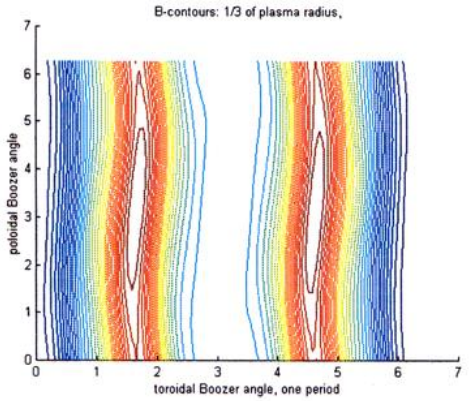

Fig. 4. B=constant lines on the inner magnetic surface for the configuration shown on Fig. 3.

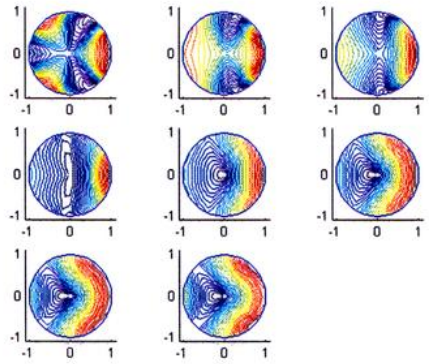

Fig. 5. $J_{||}$ contours for the configuration shown on Fig. 3 with low β. The value of $B_{reflect}$ increases from left top to right bottom diagrams. Closed $J_{||}$ contours are characterized by minimum near the magnetic axis.

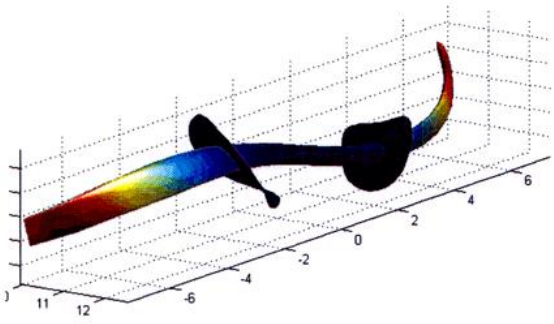

Fig. 6. Inner magnetic surface and surfaces B=constant for low β. The surfaces B=constant are slightly convex.

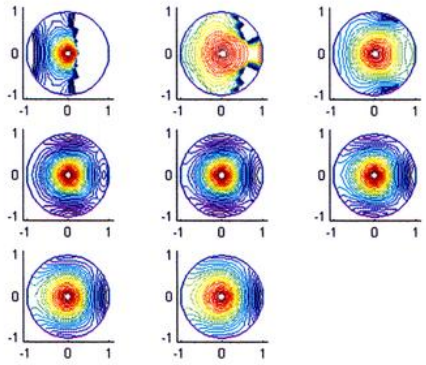

Fig. 7. $J_{||}$ contours for the configuration shown on Fig. 3 with β=5%. Closed $J_{||}$ contours are characterized by maximum near the magnetic axis.

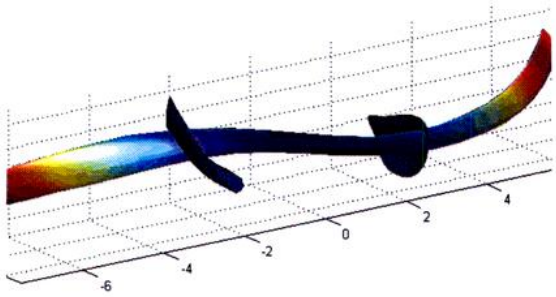

Fig. 8. Inner magnetic surface and surfaces B=constant for β=5%. The surfaces B=constant are concave.

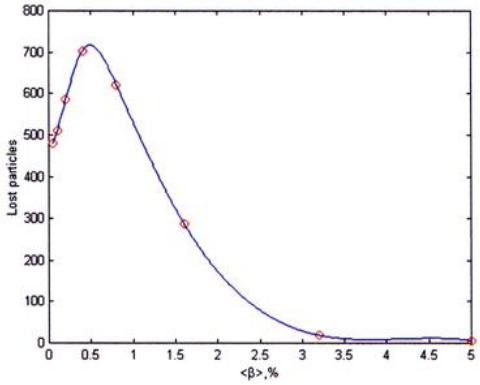

Fig. 9.Effect of β on the particles confinement. Increase of lost corresponds to the transition from minimum of $J_{||}$ near the magnetic axis to maximum.

SAWTOOTH STABILISATION BY NEUTRAL BEAM-INJECTED FAST IONS IN JET

A. Pochelon[1], C. Angioni[1], M. Mantsinen[2], N. Gorelenkov[3], K.G. McClements[4], R. Budny[3], P.C. de Vries[5], D.F. Howell[4], M.F.F. Nave[6], O. Sauter[1], S. Sharapov[4] and contributors to the EFDA-JET workprogramme[7].

[1]CRPP/EPFL, Association EURATOM-Confédération Suisse, 1015 Lausanne, Switzerland
[2]Helsinki University of Technology, Association Euratom-Tekes, Espoo, Finland
[3]Princeton Plasma Physics Laboratory, Princeton, N.J. 08543, USA
[4]EURATOM/UKAEA Fusion Association, Culham, Abingdon, OX14 3DB, UK
[5]FOM-Instituut voor Plasmafysica, 3430 BE Nieuwegein, Netherlands
[6]Associação Euratom/IST, Centro de Fusão Nuclear, 1096 Lisbon, Portugal

1. Introduction: Sawtooth instabilities are periodic relaxations of the plasma core parameters in standard tokamak scenarios. They have beneficial effects such as the ejection of impurities, the removal of Helium ashes, or can have negative effects such as the trigger of pressure limiting neo-classical tearing modes [1] or of other coupled MHD (e.g. X-event leading to disruption). The prediction of the sawtooth period or the possibility of controlling their amplitude in ITER is therefore of importance.

Energetic particles resulting from either ion cyclotron resonance heating (ICRH) [2] or fusion reactions are known to have a strong stabilising influence on the behaviour of sawtooth oscillations in tokamaks. The role of the lower-energy fast particles in neutral beam injection (NBI) is less apparent, although stabilisation was observed directly [3]. It has also been observed indirectly in tritium experiments in the Joint European Torus (JET) with (NBI), where an increase of the sawtooth period with tritium concentration was explained as a stabilising effect of NBI [4]. In such an interpretation the NBI fast ion energy content is changing due to the mass dependence of the slowing-down time.

2. Evidence of fast particle stabilisation effects: Recent discharges in JET have shown that ions arising from only deuterium NBI, with the beam injection energy of 80 and 140keV, can have similar effects. In pulses with NBI as the sole source of auxiliary heating an inverse correlation has been found between the sawtooth period τ_{saw} and the electron density n_e, as shown in **Fig 1**, for different plasma shape conditions. This inverse density scaling [5] is unlike the usual ohmic scaling laws for the sawtooth period, which show an increase in sawtooth period with density. Since the beam ion pressure is proportional to the slowing-down time, which varies as $T_e^{1.5}/n_e$, the observed anti-correlation with density suggests that beam ions have a stabilising effect. The strong T_e dependence suggested by collisionality arguments is confirmed by regression analysis over the sawtooth database, which yields $\tau_{saw} \sim T_e^{1.7} n_e^{0.23}$ [6].

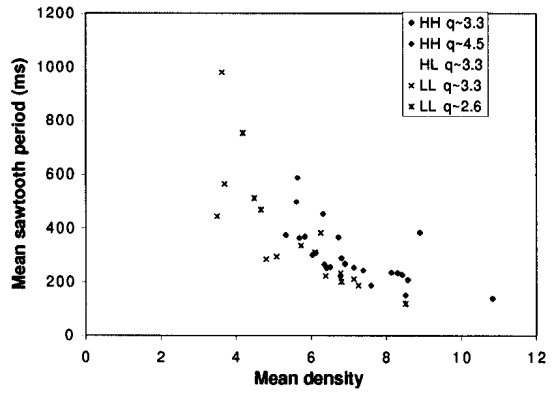

Fig. 1) Sawtooth period in NBI discharges decrease with density (different symbols indicated different plasma shapes).

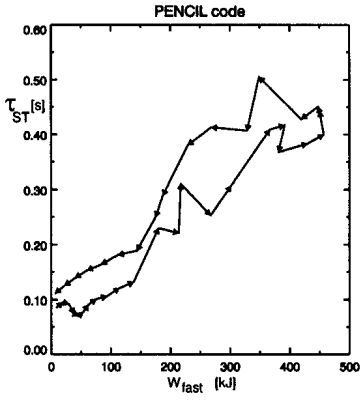

Fig. 2) The surface of the hysteresis $\tau_{saw}(P_{NBI})$ is somewhat reduced when $\tau_{saw}(W_{i,fast})$ is plotted, as shown here. Note the linear behaviour of $\tau_{saw}(W_{i,fast})$.

The linear relation between τ_{saw} and the fast ion energy content $W_{i,fast}$ calculated from the PENCIL post-processing code is shown in **Fig. 2**. This is a further indication pointing to the role of the fast particles. Also, when the evolution of τ_{saw} is plotted against NBI power (P_{NBI}), it exhibits hysteresis behaviour as P_{NBI} rises and decays, which is slightly reduced when plotted against $W_{i,fast}$ (the NBI waveform is an approximation of a trapeze as in **Fig. 3a**). This suggests that the changes in τ_{saw} are better correlated to the changes of $W_{i,fast}$ than to the ones of P_{NBI}. The hysteresis reduction is stronger when the time variation of the NBI power waveform is short and comparable to $\tau_{slow\text{-}down}$ (~50-100ms). In the experiments presented in this paper however, slow NBI ramp-up and ramp-down were made to improve on sawtooth statistics over a large power range (see **Fig. 3a**).

3. Sawtooth Model and Crash Regimes in JET: The sawtooth simulations presented in this paper are making use of a model introduced to predict the sawtooth period in ITER [7]. They include the stabilising effect of a beam ion contribution to the m=1 internal kink energy, the dimensionless energy functional $\delta\hat{W}_{fast}$, to $\delta\hat{W}_{core} = \delta\hat{W}_{MHD} + \delta\hat{W}_{KO}$, with

$$\delta\hat{W}_{fast} = -\frac{\beta_{0\,fast}}{\sqrt{2}s_1\varepsilon^{1/2}}\int_0^{r_1}\left(\frac{r}{r_1}\right)^{3/2}\frac{d\hat{p}_{fast}}{dr}dr$$

Note that the internal kink is unstable for $\delta\hat{W} = -\gamma\tau_A$. In the JET experimental cases analysed here, the ideal internal kink mode is always stable, since equations (1) and (2) are not fulfilled:

$$-\delta\hat{W}_{core} > c_h\omega_{Dfast}\tau_A \qquad (1) \qquad -(\delta\hat{W}_{core} + \delta\hat{W}_{fast}) > 0.5\omega_{*i}\tau_A \qquad (2)$$

The experimental conditions are such that the relevant crash physics always involves magnetic reconnection, and since $\rho_i > \delta_\eta > c/\omega_{pe}$, the relevant regime is the ion kinetic regime or semi-collisional regime. Equations (3a) represent the fast particle trigger and (3b) the critical shear

$$-c_\rho\hat{\rho} < -(\delta\hat{W}_{core} + \delta\hat{W}_{fast}) < 0.5\omega_{*i}\tau_A \quad (3a) \qquad c_* \max(\gamma_\eta, \gamma_\rho) > \sqrt{\omega_{*i}\omega_{*e}} \quad (3b)$$

trigger $s_1 > s_{1,crit}$, which need both to be fulfilled simultaneously to get a crash, where the second to be fulfilled actually triggers the crash. Note inclusion of frequency ω_{*_e} in addition to ω_{*_i} in (3b) to be able to describe both high T_i or T_e regimes, relevant to α- or ECW-heating [8,9]. The above crash criteria are implemented in the PRETOR transport code [9,10].

4. Comparison of Experimental Results with Modelling: A detailed analysis of a few discharges specially designed for this purpose has been performed. The approach is done in two steps. The first step is to assess the relevant instability thresholds using above crash criteria. This makes use of the experimental pressure profiles, of the fast particle energy from PENCIL code, the q profile from PRETOR equilibrium reconstructions constrained by the inversion radius and assuming $q_0 \sim 0.9$. This q profile compares well with the MSE profiles and is an average profile over the sawtooth ramp.

Figure 3d) shows that at low NBI power, below typically 1-2MW, we have the ion kinetic (reconnecting character) kink unstable with $-\delta\hat{W} > -\delta\hat{\rho}$, but the crash time is determined by the critical shear criterion (3b), the second to be fulfilled. At higher NBI power, we have stabilisation with $-\delta\hat{W} < -\hat{\rho}$ over most of the sawtooth period, except at the crash which is determined by this fast particle criterion (3a), the second to be fulfilled. The measured sawtooth period, **Fig. 3b)**, effectively starts to increase or decrease essentially from the time $-\delta\hat{W}$ crosses $-\hat{\rho}$, at the switching between the two crash criteria.

In a second step, the time evolution of the terms involved in the stability threshold is calculated with PRETOR, which yields a calculation of the sawtooth period. The latter agrees with measured values within 20%.

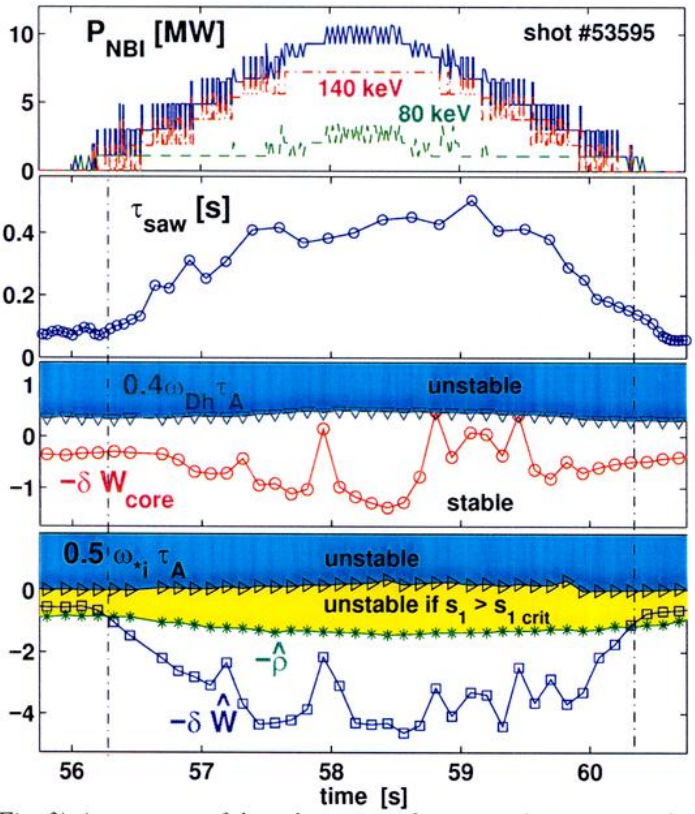

Fig. 3) Assessment of the relevant criteria (τ_{saw} averaged)
a) slow ramp trapeze-shaped NBI injection (8MW max)
b) obs. τ_{saw} increases once crit. (3a) no more fulfilled (Fig. 3d).
c) criterion (1) necessary for ideal internal kink stability,
d) criterion (2) necessary for ideal internal kink stability and τ_{saw} increases once criterion (3a) no more fulfilled.

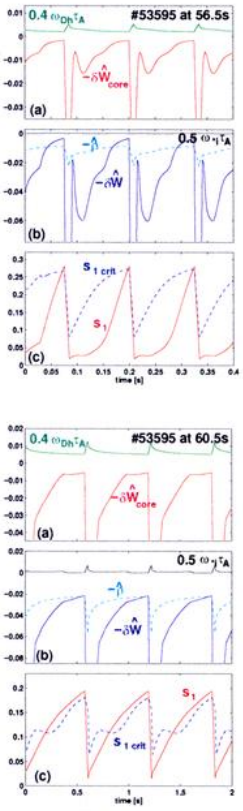

Fig.4a,b) PRETOR evolution of crash criteria: a) at low power: shear determines crash time, b) at high power: fast particles determine the crash time.

PRETOR uses the presented analytical expression for the fast particle energy functional $\delta\hat{W}_{fast}$, valid for isotropic distributions. Realistic distributions, as computed by TRANSP, are anisotropic. The effect of anisotropy on $\delta\hat{W}_{fast}$ has been computed with the NOVA-K MHD code [11], which takes as input the TRANSP distribution functions and properly describes the fast particle toroidal precession, considering the realistic geometry. The NOVA-K calculations of $\delta\hat{W}_{fast}$ have been found in very good agreement (errors within 15%) with the evaluations provided by the analytical formula used in PRETOR, whereas the same formula is found to generally under-estimate the fast particle contribution compared to numerical results obtained with isotropic distributions in NOVA-K. This validates the use of the analytical formula in PRETOR simulations of the present JET discharges. The beam ion contribution is found to be strongly stabilising, causing τ_{saw} to be much longer than it would otherwise be. When this contribution is not taken into account, the model predicts a sawtooth period, which, at full NBI power, is about two times lower than the experimentally observed period.

4. Further experimental observations: The possible role of other experimental variables in determining τ_{saw}, such as plasma rotation [11], requires further evaluation. The repetitive feature observed on the sawtooth period occurring at switch-on/-off, see Fig. 5, may give some clues. The τ_{saw} increases 0.2-0.3s after switch-on, then decreases. The rotation first gradually increases, as measured by magnetic coils, followed by a strong acceleration at 0.8s. One possible interpretation of the first peak in τ_{saw} is sawtooth stabilisation by the freshly injected non-thermalised fast particles which, when thermalisation occurs modifies both diamagnetic rotation and momentum transfer rotation, playing a role in the later transients. Note that at low power, rotation is a dominant ingredient of the crash trigger (equation 3b).

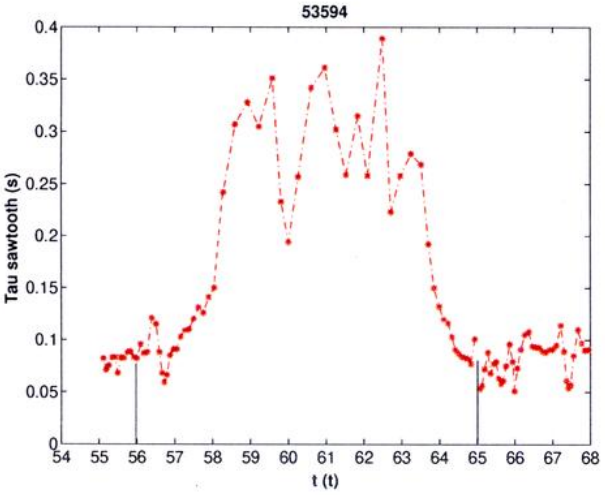

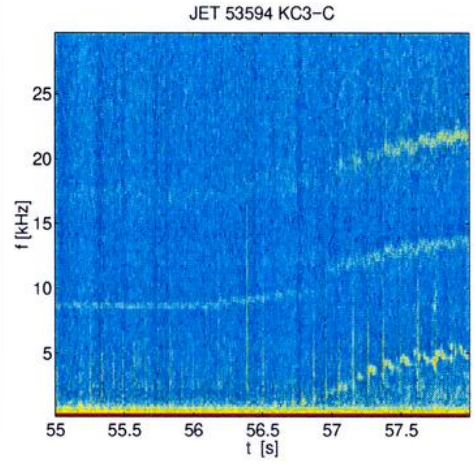

Fig 5

a) (top left) Sawtooth period transient at NBI power switch-on/-off (indicated by vertical lines)

b) (bottom right) Expansion of sawtooth period transient at NBI power switch-on, details of the NBI waveform

c) (top right) Spectrogram of magnetic coil indicating rotation changes (same time scale as in Fig. 5b)

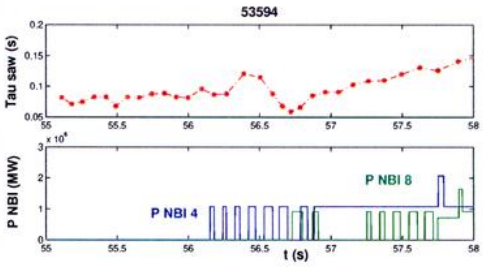

5. Conclusions: Several experimental observations point to the role of NBI fast particles in stabilising sawteeth in JET: the density behaviour of τ_{saw}, the hysteresis reduction, the linear relation of τ_{saw} versus $W_{i,fast}$. In the framework of a model introduced to predict the sawtooth period in ITER [7], we have included the stabilising effect of a beam ion contribution to the m=1 internal kink energy. This has been implemented in the PRETOR transport code [9], and a detailed analysis of a dedicated JET discharges has been performed. The beam ion contribution is found to be strongly stabilising, causing τ_{saw} to be much longer than it would otherwise be. The sawtooth trigger condition occurring in JET, namely excitation of the ion kinetic (also called semi-collisional, with reconnecting character) internal kink mode, was fou-nd to be the one most likely to be relevant to ITER, with the role of beam ions in JET played by α-particles in ITER [7]. The NBI discharges in JET thus allow us to study fast particle effects likely to play an important role in determining the performance of Next Step Devices.

Acknowledgements

This work has been performed under the European Fusion Development Agreement.

References

[1] O. Sauter et al., this Conference, Oral OT.08.

[2] D.J. Campbell et al. Phys. Rev. Lett. **60** (1988) 2148; F. Porcelli, Plasma Phys. and Contr. Fusion **33** (1991) 1601; J.P. Graves et al., PRL **84**, (2000) 1204.

[3] J. Ongena et al., Proc. of 17th EPS Conf. on Contr. Fus. and Plasma Heating, Amsterdam, Vol. 3 (1990) 155; P.-A. Duperrex et al., Nuclear Fusion 32 (1992) 1161.

[4] M.F. Nave, K.G. McClements et al., 25thEPS Contr Fus & PP, ECA Vol **22C** (1998) 365.

[5] R. Buttery, T. Hender, D. Howell et al., priv. com. 2000 (Sawtooth database 1999).

[6] P. de Vries et al., this Conf., Poster P5.001.

[7] F. Porcelli et al., Plasma Phys. Control. Fusion **38**, (1996) 2163.

[8] O. Sauter et al, Th. Fus Plasmas, Varenna 98, ISSP-18, Ed. Compos., Bologna(1999) 403

[9] C. Angioni et al., Th. Fus Plasmas, Varenna 00, ISSP-19, Ed. Comp., Bologna (2000) 73.

[10] D. Boucher, P.-H. Rebut, JET Pre-print JET-P (92) 51, p3 (1992).

[11] N. Gorelenkov, M.F. Nave et al., 27th EPS Contr. Fus. & Plasma Phys., P4 079 (2000).

[7] Contributor's list: see J. Paméla, Proc. of 18th IAEA FEC, Sorrento 2000, paper PD/1.

LOCALIZED BALLOONING MODES IN COMPACT QUASIAXIALLY SYMMETRIC STELLARATORS*

M. H. Redi[1], J. Canik[2], R. L. Dewar[3], **E. D. Fredrickson[1]**, W. A. Cooper[4], J. L. Johnson[1], S. Klasky[1]

[1] *Princeton Plasma Physics Laboratory, Princeton, NJ 08543*

[2] *Dept. of Electrical and Computer Engineering, University of Wisconsin, Madison, WI*

[3] *Dept. of Theoretical Physics, The Australian National University, Canberra, Australia*

[4] *Centre de Recherche en Physique des Plasmas, EPFL, Lausanne, Switzerland*

Introduction

Understanding of ballooning mode stability boundaries may lead to performance improvement of toroidal devices through control of disruptions. Toroidally localized ballooning modes have been found as precursors to high beta disruptions on TFTR[1] arising in conditions of n=1 kink mode asymmetry. Recent optimization has shown that magnetohydrodynamic stability as well as good particle confinement are likely to be achievable in the National Compact Stellarator Experiment (NCSX), a compact, quasiaxially symmetric stellarator (QAS) for values of the plasma near $\beta = 4\%$[2]. The configuration, with a major radius of 1.42 m, an aspect ratio of 4.4, a toroidal magnetic field 1.2-1.7 T and 6MW of neutral beam heating, is stable to MHD instabilities, and is expected to be limited by high-n kink and ballooning modes. This paper describes the ballooning eigenvalue isosurfaces for NCSX, the first step in an examination of the kinetic stabilization of the ballooning beta limit using a hybrid WKB approach[3].

Eigenvalue Isosurfaces of the Quasiaxially Symmetric Stellarator

The VVBAL module of the TERPSICHORE code suite[4] has been used to calculate the ballooning instability for several NCSX equilibria (Fig. 1) above the design point (β = 4.1%) with the VMEC code. The displacement of the flux surface grows with growth rate γ; $\xi \propto \exp(i\omega t) \propto \exp(\gamma t)$. We define the eigenvalue $\lambda = -\omega^2$; positive values of λ denote instability, while negative values denote stability. For $\beta = 4.3\%$ and $\beta = 6.8\%$ we have assembled a datacube of ballooning eigenvalues $\lambda(s,\alpha,\theta_k)$, of size (126,101,21). s is the toroidal flux, α is the field line variable. Roughly, within $\pm\pi$, the ballooning parameter θ_k determines where the eigenfunction is a maximum. Figure 2 shows the plasma iota of the two equilibria. These are weak shear plasmas, with vanishing shear near the edge.

The isosurfaces of λ describe the possible trajectories of rays of the ballooning equation. Consequently they characterize the quantization conditions that are used to find the maximum wave vector, and thereby kinetic stabilization of the ballooning beta limit. The QAS isosurfaces are found to exhibit unusual and unique topologies for the two configurations. Distinct structures occur in different ranges of λ in the stable spectrum: a) at $\lambda = -0.15$, a helical structure is found near the plasma edge, rotating about an axis nearly parallel to?the θ_k axis, with fins stretching toward the plasma center; b) at $\lambda = -0.45$, cylinders are found nearly constant in θ_k, localized in s and α. At $\beta = 6.8\%$, similar structures in the stable spectrum occur, although more global in extent.

The unstable spectra are less complex, consisting primarily of planes and topologically cylindrical and spherical isosurfaces near the outer edge of the plasma, where shear goes to zero and the instability is more easily driven. In general, there is a weak dependence on the ballooning angle θ_k, stronger dependence on the field line α and quite strong dependence on the radial parameter s. At $\beta = 4.3\%$ topologically spherical isosurfaces are found for the maximum eigenvalues, indicative of strong quantum chaos[3]. This description "quantum chaos" for the paths of rays of the ballooning equation does not mean that the plasma behavior is chaotic, but that the mathematics of a quantum chaotic scattering problem can be used for instabilities far above the marginal point of the equilibrium. At lower values of the eigenvalue, isolated unstable cylindrical and planar isosurfaces conjoin, as the eigenvalue λ drops to zero, and the isosurface is no longer simply connected. At $\beta = 6.8\%$ the bands break up at maximum eigenvalues. The configuration is Mercier stable at both values of β.

Comparison with a related axisymmetric tokamak shows that the structures of the stable and unstable spectra of the QAS arise from the complexity of the magnetic configuration.

Finite Larmor Radius Stabilization of the Beta Limit

In practice, only finite-*n* modes can be unstable due to finite ion Larmor radius (FLR) stabilization. Finite-*n* ballooning mode stability calculations with a three-dimensional, linear MHD code for a two-field period QAS configuration showed that the finite *n* ballooning modes ($n \sim 20$) are significantly more stable than the infinite-*n* results. For H1 and LHD finite *n* ballooning modes have been examined by applying the WKB ballooning formalism and semi-classical quantization or quantum chaos theory, depending on the

topology of the isosurfaces[3]. The validity of the hydrodynamic, fluid model for MHD breaks down and kinetic corrections are required if the condition $(k_\perp \rho_i)^2 << 1$ is not satisfied. Here $k_\perp$ is the wave vector perpendicular to the field line, and ρ_i is the ion Larmor radius, which for the QAS is ~1cm. Near the beta limit the ballooning rays at the marginal point ($\lambda=0$) will propagate on an isosurface having topology of conjoined cylinders, with axes parallel to θ_k. It does not appear that either the Einstein-Keller-Brillouin semiclassical quantization method or the quantum chaos approach applies.

Anderson localization

Symmetry breaking localization of the ballooning mode in stellarator plasmas has been identified for LHD, H1 and HSX[5] as analogous to Anderson localization[6] of electron eigenfunctions in condensed matter. Our calculations show that localization of the QAS eigenfunction increases for reduced plasma shear (Fig. 3). Each flux surface has a different shape, changing the poloidal angle at which the eigenfunction is maximized. Weak shear increases localization of the eigenfunction, in contrast to the tokamak case[7]. The most localized modes in this geometry occur in the region where global magnetic shear is weakest, including at the shear reversal surface itself, demonstrating the existence of Anderson localization in the QAS.

Conclusion

We find Anderson localization of the ballooning mode in the QAS and have obtained eigenvalue isosurfaces with which to examine kinetic stabilization of β. A new method of regularizing the eigenfunction to estimate $k_\perp$ will be needed for the QAS at the beta limit, since the topology of the marginal point isosurfaces is not simply connected.

1. E. Fredrickson, *et al.*, Phys. Plas. **3**, 2620 (1996).

2. A. H. Reiman, *et al.* Phys. Plas. **8**, 2083 (2001).

3. R. L. Dewar, P. Cuthbert, R. Ball, Phys. Rev. Lett. **86**, 2321 (2001).

4. D. V. Anderson, *et al.* in "Theory of Fusion Plasmas", I. F-E C. Bologna, (1988) p93.

5. C. Hegna, S. Hudson, to appear in Phys. Rev. Lett. (2001).

6. P. W. Anderson, Phys. Rev. **109**, 1492 (1958).

7. P. Cuthbert, R. L. Dewar, Phys. Plas. **7**, 2302 (2001).

* Research supported by U. S. DOE Contract DE-AC02-76CH03073. John Canik held a DOE National Undergraduate Fellowship at PPPL during summer, 2000

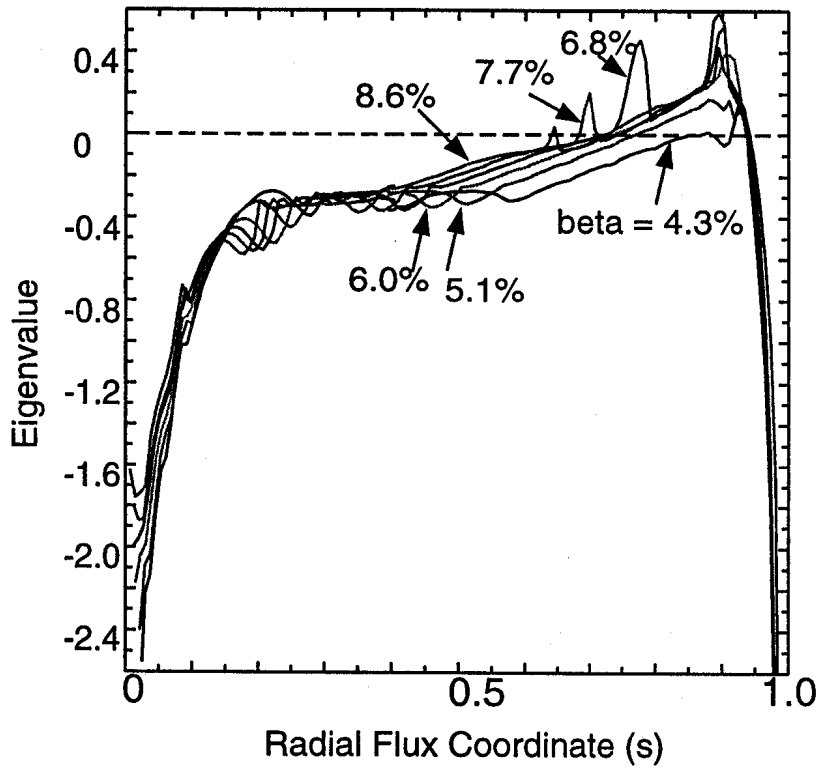

Figure 1. Ballooning eigenvalues for NCSX above the design point. α=0, θk=0.

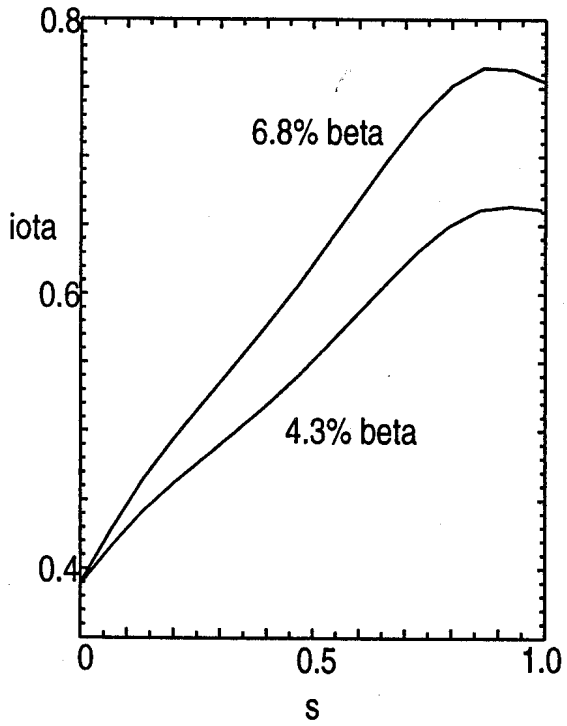

Figure 2. Iota profiles for equilibria above the design point beta.

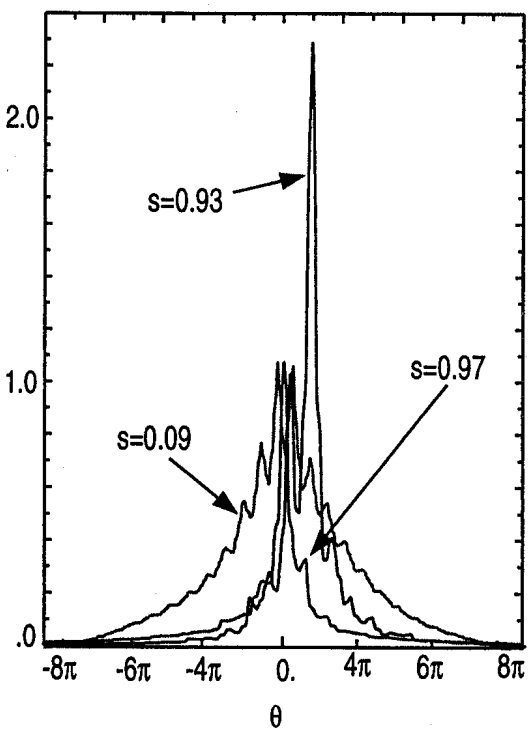

Figure 3. Eigenfunction localization in poloidal angle near the plasma edge, labeled by s, the edge normalized toroidal flux.

NEOCLASSICAL TEARING MODE SEED ISLAND CONTROL WITH ICRH IN JET

O. Sauter[1], E. Westerhof[2], M.L. Mayoral[3,4], D. F. Howell[3], M.J. Mantsinen[5], B. Alper[3], C. Angioni[1], P. Belo[6], R. Buttery[3], K.G. McClements[3], A. Gondhalekar[3], T. Hellsten[7,8], T.C. Hender[3], T. Johnson[8], P. Lamalle[7,9], F. Milani[3], M.F. Nave[6], F. Nguyen[4], A.-L. Pecquet[4], S. Pinches[10], S. Podda[11], J. Rapp[12] and contributors to the EFDA-JET workprogramme*

1) Centre de Recherches en Physique des Plasmas, Association EURATOM-Switzerland, EPFL, 1015 Lausanne
2) FOM-Instituut voor Plasmafysica "Rijnhuizen", TEC, Assoc. EURATOM-FOM, Nieuwegein, Netherlands
3) EURATOM/UKAEA Fusion Association, Culham Science Centre, Abingon, UK
4) DRFC, CEA de Cadarache, F-13108 St. Paul-lez Durance Cedex, France
5) Helsinki University of Technology, Association Euratom-Tekes, Finland
6) Centro de Fusao Nuclear, Instituto Superior Tecnico, P-1049-001 Lisboa, Portugal
7) EFDA-JET Close Support Unit, Culham Laboratories, Abingdon, United Kingdom
8) Association EURATOM-NFR, Royal Institute of Technology, Stockholm, Sweden
9) LPP/ERM-KMS, TEC, Association EURATOM-Belgian State, 1000 Brussels, Belgium
10) Max-Planck-IPP, IPP-EURATOM Association, Garching, Germany
11) Frascati, Association EURATOM-ENEA, Italy
12) Institut für Plasmaphysik, Forschungszentrum Jülich, TEC, EURATOM Association, Jülich, Germany
*See annex of J. Pamela et al, "Overview of Recent JET Results and Future Perspectives", Fusion Energy 2000 (Proc. 18th Int. Conf. Sorrento, 2000), IAEA, Vienna (2001)

Abstract

The destabilisation of neoclassical tearing modes (NTM) requires a finite size seed island which is often provided by sawtooth activity. It is shown that the beta value at the onset of NTMs can be significantly modified by altering the sawtooth period using ICRH in JET. Sawtooth stabilisation, leading to long sawtooth periods, enables NTMs to be triggered at low beta value, consistent with larger induced seed islands. By destabilising sawteeth, that is with a shorter sawtooth period, larger beta values are required to trigger NTMs. This is the first clear direct demonstration of the relation between sawteeth and NTMs and opens the possibility of increasing the beta threshold by sawtooth destabilisation. Adding a slow power ramp-down, after the mode onset, shows that NTMs are metastable as long as the discharge is in H-mode in JET, emphasising the role of seed island control to avoid NTMs.

Introduction

Neoclassical tearing modes (NTMs) are known to limit tokamak performance to normalized beta values, β_N, well below the theoretical ideal-MHD β-limit (β is the ratio of the total pressure p to the confining magnetic pressure $B_0^2/2\mu_0$, and $\beta_N=\beta[\%]/(I_p/aB_0)$, with I_p[MA] the plasma current, B_0[T] the magnetic field and a[m] the plasma minor radius). The destabilisation of NTMs requires the formation of a seed island of a finite size, larger than a critical island width [1]. This island can be triggered by sawtooth precursor or crash, edge localised modes (ELMs), fishbones or other perturbations like pellets [2]. Once the island is formed, the pressure profile flattens and the resulting perturbed bootstrap current drives the island to a usually much larger saturated width. Different methods have been applied to stabilise the mode once it is formed, by local current drive with ECCD or by global current drive with LHCD [3], for example. Here a new method is proposed consisting of preventing the mode formation by reducing the perturbations such that the islands triggered are smaller than the critical island width. The main source of perturbations in most tokamaks is the sawtooth activity. Avoiding sawtooth altogether has been shown to increase the beta limit for NTMs [4]. However this is difficult to keep in steady-state for standard type scenarios and one loses the beneficial particle control provided by regular sawteeth. The idea developed in these experiments is to destabilise the sawteeth such as to have short and regular sawtooth periods, assuming that it will lead to smaller perturbations and seed island sizes. It is well-known that sawtooth periods can be changed using ICRH [5] or ECCD [6] for example. Therefore the main scenarios of Refs. [5] have been used, that is changing the antenna phasing or the resonance location [7]. First we show the relation between long sawtooth periods and NTMs destabilisation at low beta. Sawtooth stabilisation is obtained mainly by

increasing the fast particle population in the centre. In this way, NTMs can be destabilised at any field in JET, even at β_N as low as 0.5-1. We shall also show that on the contrary, by destabilising sawteeth (in the sense that shorter sawtooth periods are obtained) enables to increase significantly the β_N and neutron rate at the NTM onset.

Results

We show in Fig. 1 the usual global plasma parameter domain, β_N versus ρ_*, at the m=3/n=2 NTM onset in JET. The blue symbols are NBI only discharges, red/pink those with ICRH. It shows that the cases with dominantly ICRH have much lower beta onset. The simplest explanation is that sawteeth are more strongly stabilised by the fast particles induced by ICRH than by NBI heating [8]. The solid blue circles are NBI only discharges which have a low beta onset. We have checked these cases and they all occur either after a sawtooth period of ~800ms or at the first measurable sawtooth crash out of the ohmic part, which is why they are marked differently. To directly test the effect of sawtooth, we compare discharges with 5MW of fundamental H minority ICRH and a power ramp-up of NBI power in order to trigger NTMs. The magnetic field is changed from shot to shot to span the resonance position from outside the inversion radius towards the centre of the plasma. The antennas have a +90° phasing such as to increase the fast particles pressure in the centre. With the resonance position moving inwards, the fast particle population inside q=1 increases [5b, 7] and so does the sawtooth stabilisation [9]. As can be seen on Fig. 2, small changes of 0.08T, leading to a 9cm shift of the resonance position, can change the sawtooth period from 440ms to 630ms. In these scenarios, all the discharges with sawtooth periods longer than approximately 600ms and $\beta_N \geq 0.8$-1 have triggered 3/2 NTMs at the sawtooth crash. On the contrary, as illustrated by the shot 51790 and 51792 in Fig. 2, discharges with sawtooth periods smaller than ~600ms have not triggered NTMs, even with more than 20MW of total power coupled to the plasma and β_N up to 2. It should be noted that the effect does not seem to be linear with sawtooth periods.

A further test is to change only the antenna phasing. The -90° phasing induces a drift of the trapped orbits outwards, reducing the stabilising term which results in much shorter sawtooth periods [5b]. Repeating the discharge 51794 at 2.49T with –90° phasing and otherwise similar parameters leads to regular sawtooth periods of about 200ms and no NTM are triggered even with 21MW total power coupled and $\beta_N \sim 2$. On the other hand, previously JET was unable to trigger NTMs with NBI alone at larger magnetic field ($B_0 \geq 1.7$T) because the maximum achievable β_N is too low. However, using fundamental minority H heating with +90° or dipole phasing of the antennas, long sawtooth periods are induced and NTMs can be triggered at low β_N. In this way NTMs are obtained at any field with standard type scenarios in JET, which is useful to study these modes in a wide plasma parameter domain. By adding a slow power ramp-down after the mode is triggered the critical beta limit can be determined, independently of the trigger mechanism. Two examples are shown in Fig. 3, at 1.4T/1.4MA and at 3.3T/3.3MA. The first case is a NBI heating only discharge, for which the mode is triggered at $\beta_N \sim 3$, while the second case has ICRH with the +90° phasing and the mode is triggered after a long sawtooth period, at $\beta_N \sim 1$. In both cases β_N slowly decreases and the mode is stabilised near or even after the H-L back transition, that is at $\beta_N \sim 1$ or 0.5 respectively. This has been confirmed at fields between 1T to 3.3T with discharges having similar $q_{95} \sim 3.4$. Therefore standard scenarios in H-mode in JET are metastable to 3/2 NTMs. Thus, once in H-mode, the only determinant factor to trigger the mode is the existence of a seed island with a width larger than the critical island width. This is why controlling sawtooth activity has such a dramatic effect on JET. In addition, rotation has a crucial role as discussed in Ref. [10]. The low NTM onset was also observed in NBI only cases, due to long sawtooth periods obtained by an inadequate power ramp-up [11].

The ultimate goal is of course to suppress or avoid these modes. As they are metastable in H-mode discharges, the best way to prevent these modes is to control the size of the seed islands, therefore of the plasma perturbations. The idea is to destabilise the sawteeth to shorten the sawtooth period. In this way one keeps the useful particle redistributions and avoids impurity accumulation, while reducing the plasma perturbations. In order to better demonstrate the effect, we need a test case of a NTM destabilised by NBI only and therefore

work at B_0<1.7T. In this case, only 2nd harmonic heating is possible to have power deposition and CD near or just outside the inversion radius. First we have studied the optimal position for sawtooth destabilisation as detailed in Refs. [7a, b]. Then we have fixed the magnetic field at an optimal value, such that the resonance position is just outside the inversion radius, and we have added a NBI power ramp to determine β_N at the onset of the mode. The result is shown in Fig. 4, where a NBI only case (in blue) and a 5MW ICRH + NBI case (in red) are shown. The total power is kept the same for both cases during the whole ramp. The discharge is at 1.2T/1.2MA, that is a very low magnetic field for JET, and the resonance position is just at the HFS of the inner inversion radius and moves towards the centre when beta increases. At 62.6s, a NTM is triggered at β_N ~3 and Ptot~8MW in the NBI only case. These values are typical for these scenarios. Note that β_N drops at the mode onset. However, the NBI+ICRH case reaches β_N of 3.8 without 3/2 NTMs, close to the ideal limit. The role-over in shot 51994 at 65.2s is due to a 5/4 mode and then a 4/3 mode. At 66.1s, a 3/2 mode is triggered and β_N drops even further. Note that by that time the resonance position has shifted to the inversion radius due to β effect, however at these high b values, fishbones are present and can trigger the mode as well [2a]. Thus up to about 20MW have been coupled to the plasma without triggering 3/2 NTMs. As the NTM is metastable for $\beta_N \geq 1$, at the L-H transition, the perturbations have to be kept smaller in order to reach higher β_N values. Note also that combined heating, NBI+ICRH, usually leads to much lower NTM threshold, as discussed in the introduction, Fig. 1, and in Ref. [10] in relation to rotation effects. In Ref. [10] similar plasmas as shown in Fig. 4 are discussed, except at 1.4T/1.3MA to have central ICRH. Note that in these cases, with combined heating, β_N~2-2.5 at the mode onset. It is only by a careful choice of the resonant position, such that it destabilises significantly the sawteeth, that we are able to increase β_N at the onset of the mode in ICRH+NBI cases.

Two other important results are shown in Fig. 4. First the increase in neutron rate is even more dramatic between the value at the mode onset for the NBI only case, ~1.2 $10^{15}s^{-1}$, and for the ICRH+NBI case, 3.8 $10^{15}s^{-1}$. This confirms that a much higher performance is obtained without triggering NTMs and is the relevant improvement obtained by destabilising sawteeth. The other important effect is that the island width, for the case 52712, first increases with β_N, but then saturates to a smaller value when $P_{NBI} \geq 15$MW. It follows that better confinement is recovered, which is why both discharges have similar β_N values at 65s, even though shot 51994 has no NTMs. We call this effect "self-healing" of the mode. It can be due to increased rotation, change of Δ' or global profile modification, and is probably related to interruptions of the mode as observed in AUG and JET [12]. Further detailed analyses are in progress to better quantify this effect. However one should note that the neutron rate is not fully recovered and is still 20-30% below the NTM free case. This is due to the fact that even a small island decreases the central density and temperature values, which contribute much more significantly to the neutron rate than to the global stored energy.

Conclusion

The main difference in β_N at the onset of 3/2 NTMs in JET between NBI and ICRH dominated discharges has been clearly related to the effects on sawteeth. Note that rotation also affects the NTM trigger [10]. Sawtooth stabilisation (long sawtooth period) has been shown to trigger NTMs at much lower β_N, as soon as $\beta_N > \beta_{Ncrit}$. Dedicated experiments have shown that JET standard discharges, with q_{95}~3.4, are metastable to NTMs as soon as they are in H-mode. Therefore better performance without triggering NTMs can only be obtained by controlling the seed island formation and minimising the perturbations. We have shown that by adding 2nd harmonic H minority ICRH and carefully positioning the resonance layer just outside the inversion radius, such as to destabilise the sawteeth, higher values of β_N and much higher neutron rates are obtained before the NTM is triggered. Therefore, on the one hand, we have confirmed that NTMs are most likely to occur at low β_N due to alpha particle stabilisation and long sawtooth periods in ITER like standard configuration, without sawtooth control. On the other hand, the possibility of avoiding NTMs by sawtooth destabilisation has been demonstrated with ICCD. Another method can be ECCD which is very efficient in modifying the sawtooth period. Its potential should be better evaluated for future experiments, in particular as its CD efficiency is much higher near q=1 than near q=1.5.

Acknowledgements

We are grateful to the UKAEA for the efficient operation of the JET-EFDA tokamak. This work was performed in part under the EFDA. OS and CA are supported in part by the Swiss National Science Foundation.

References

1. O. Sauter *et al*, Phys. Plasmas 4 (1997) 1654.
2. P. Belo *et al* and M. Maraschek *et al*, this conference
3. G. Gantenbein *et al*, Phys. Rev. Lett. 85 (2000) 1242; C. D. Warrick *et al*, Phys. Rev. Lett. (2000).
4. R. J. La Haye *et al*, Nucl. Fusion **40** (2000) 53.
5. V. P. Bhatnagar *et al*, Nucl. Fusion 34 (1994) 1579 ; L.-G. Eriksson et al., Phys. Rev. Lett. 81 (1998) 1231
6. M.A. Henderson *et al*, Fusion Engineering and Design 53 (2001) 241.
7. M. L. Mayoral *et al*, RF Topcial Conf. (2001) ; M. Mantsinen *et al*, F. Nguyen *et al*, this conference.
8. F. Nabais *et al*; A. Pochelon *et al*, this conference.
9. F. Porcelli *et al*, Plasma Phys. Contr. Fus. **38** (1996) 2163
10. R. Buttery *et al*, this conference
11. J. Ongena *et al*, this conference
12. S. Guenter *et al*, submitted to PRL

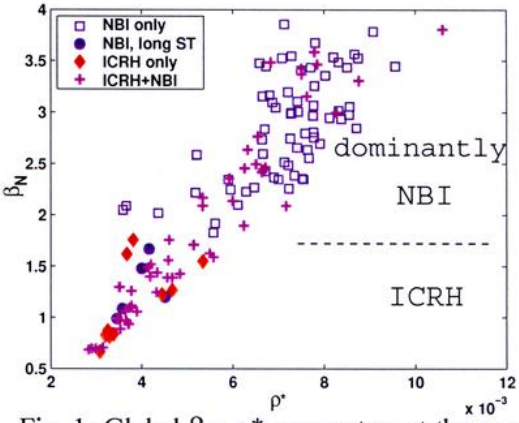

Fig. 1: Global β_N, ρ* parameters at the onset of 3/2 modes for NBI and ICRH dominated discharges .

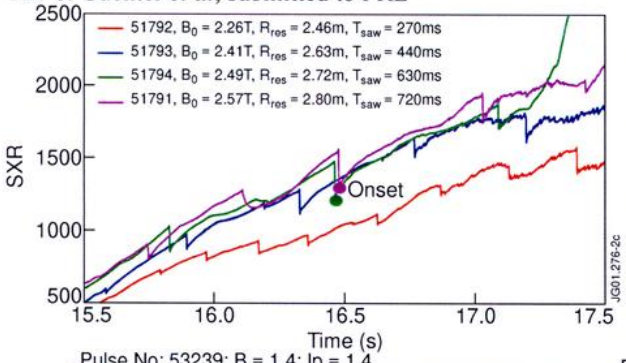

Fig. 2: SXR signals for similar discharges, changing only the ICRH resonance position. I_p/B_0 is kept fixed. The first two cases do not trigger NTMs even up to full power. The onset is marked for the other two cases (the HFS inversion is ~2.8m in JET)

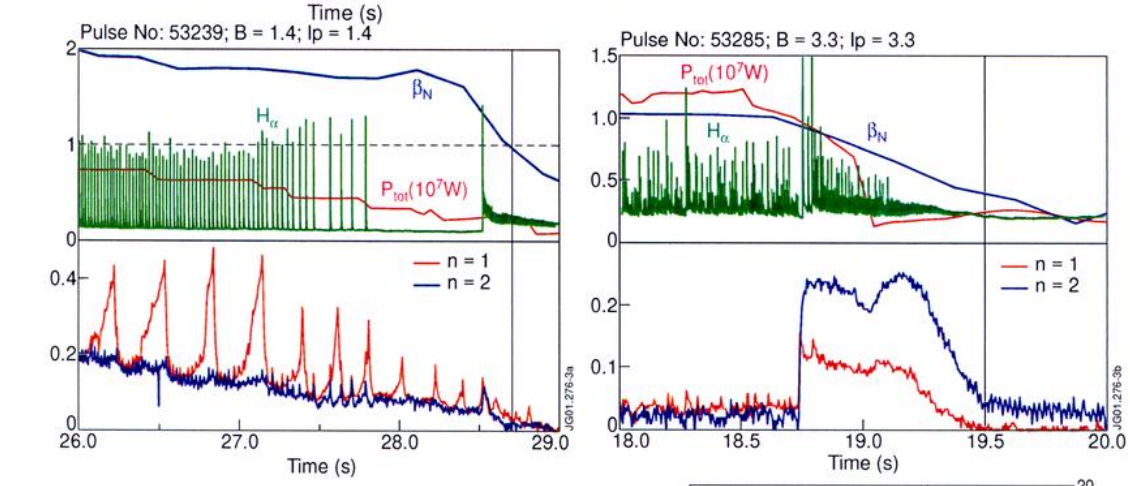

Fig. 3(above): Power ramp-down phase, after NTMs have been triggered, for cases at low and high magnetic field. Shot 53239 is heated by NBI only, while 53285 has NBI and 5MW of ICRH power. In both cases the mode is stabilised near the H-L transition, as seen from the H_α trace.

Fig. 4: Similar discharges at low magnetic field, 1.2T and current, 1.2MA. The total power waveform is the same, with NBI only for 52712 and NBI+ICRH in 51994. In the ICRH case, 5MW 2nd harmonic hydrogen minority heating is coupled with the resonance just outside the inversion radius, on the HFS.

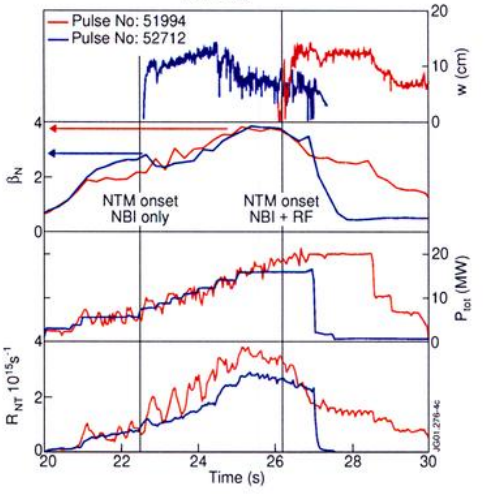

IMPURITY TRANSPORT IN SHAPED TCV PLASMAS

E. Scavino, J. S. Bakos[1], H. Weisen, A. Zabolotsky

Centre de Recherches en Physique des Plasmas
Association EURATOM - Confédération Suisse, EPFL, 1015 Lausanne, Switzerland
[1] KFKI Research Institute for Particle and Nuclear Physics
Budapest, Hungary

1. Summary

Impurities determine radiation losses, contribute to fuel dilution and hence play an important role in fusion plasmas. In view of advanced, strongly shaped reactor designs, one important and frequently neglected aspect is the effect of operating modes and plasma geometry on the confinement of fuel particles and impurities, specifically in relation with the energy confinement. The extreme shaping capabilities of TCV (Tokamak à Configuration Variable, R = 0.88 m, a = 0.25 m, vacuum vessel elongation κ = 3 and vacuum central magnetic field $B \leq 1.51$ T) allow the exploration of the effects of plasma geometry on both energy and impurity transport and confinement.

Small non perturbing quantities of laser-ablated impurities were injected into Ohmic plasmas in TCV and the time evolution of the soft X-ray emission was measured. The global lifetime of the impurities was obtained from the exponential decay of the X-ray emissions after the influx phase. For constant plasma geometry a correlation between the lifetime τ_{imp} and the line averaged electron density is observed. Remarkably this lifetime decreases in higher elongation plasmas and more importantly the ratio τ_{imp}/τ_{Ee} is reduced as well by a factor 3 when the elongation is increased from κ=1.6 to κ=2.3.

By means of the 1-D particle transport code STRAHL[1] the radial dependence of transport parameters (diffusion coefficient and convective velocity) has been modelled for different plasma configurations.

2. Diagnostics

Impurities are produced by laser ablation in a dedicated vacuum chamber, which is connected to the TCV vessel via a vacuum duct and a gate valve. The ablation target is mounted on a motorised chariot, inside the chamber at a distance of ~70cm from the plasma edge, and it is remotely moved after each shot. The target is made by a 1μm thin film, typically Aluminum or Silicon, on a glass slab which is large enough to be used for averagely one hundred shots. A single pulse laser beam, from a Q-switched ruby laser (up to 5J/pulse during ~20ns) is focused onto a spot whose diameter is roughly 3 mm for a corresponding energy density of ~30J/cm^2, producing a puff of 10^{15}-10^{16} atoms.

The most relevant diagnostics which were used for impurity tracking were the soft X-ray tomography system and the Thomson scattering system for the electron temperature and density. The former consists of 10 cameras with 20 channels each, viewing the plasma on a poloidal plane. It is equipped with a 47μm Beryllium filter, which gives a spectral sensitivity in the range from 1keV up to 10keV. The time resolution is 13μs, which allows the detailed separation of the sawtooth structures superimposed onto the impurity signal.

The Thomson scattering uses 3 coaxial Nd:YAG lasers which provide profile measurements from 25 positions at the total frequency of 60Hz.

3. Experimental results

Impurities have been injected in a large variety of TCV plasmas, with the main purpose of exploring the effects of shape on the particle transport and in particular on the impurity residence

time. This parameter is obtained from the raw X-ray signals, in which the background emissions and the sawteeth have been removed by means of the GSVD decomposition[2]. A fit is then performed on the signal tail, with an exponential function whose time constant defines the impurity confinement time. All raw signals tend to leave a non-zero asymptotic residual plateau, typically 5% of the peak intensity (Fig.1), indicating that a small part of the impurities recycle from the wall. Another common feature, among central chords, is the duration of the peak, defined as the fwhm of the signal: as will be shown in Sec.4, this fact suggests a rapid diffusion driven by sawteeth through the plasma core.

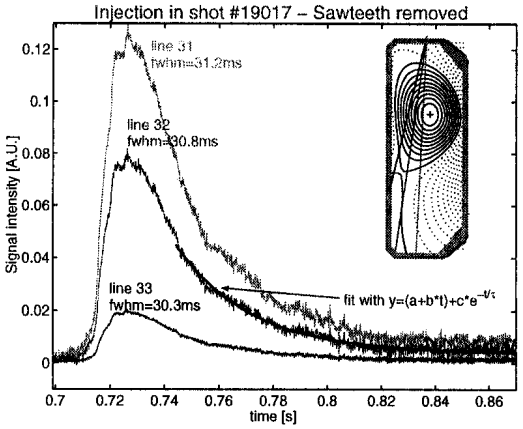

Fig.1. Raw signals provided by the soft X-ray tomography cameras. Sawteeth as well as the background emission have been removed by means of the GSVD decomposition[2] so to reduce the uncertainty on the fwhm and τ_{imp} values. In the inset, the poloidal cross section of the "standard shot", with the position of the viewing chords 31, 32, 33.

A density scan was performed in the so-called "TCV standard shot" (diverted L-mode ohmic plasma whose parameters are $\kappa = 1.64 \pm 0.02$, $\delta = 0.34 \pm 0.02$, $I = 272 \pm 5$ kA) during which the electronic density is normally varied during the shot. The results, presented in Fig.2a, show that there is a slight increase of the confinement time with density, as τ_{imp} goes from 18ms up to 32ms when $\langle n_e \rangle$ is increased from $3 \cdot 10^{19}\,m^{-3}$ up to $6 \cdot 10^{19}\,m^{-3}$.

A remarkable observation can be made in another series of experiments. The elongation of limited plasmas was varied from $\kappa = 1.6$ to $\kappa = 2.3$ in a series of ohmic limiter shots in which q_{eng} (proportional to the ratio $I_p/B_T\kappa$) was kept approximately constant. As shown in Fig.2b, the confinement time is more than halved as τ_{imp} goes from 48ms at moderate elongation, to less than 20ms when $\kappa = 2.3$. In this scan a possible minor contribution of density is not taken into account, since $\langle n_e \rangle$ decreases with κ by no more than 15% over the whole range of elongations.

For the same series of injections the electron energy confinement time was calculated, as the ratio of the electron energy content and the total heating power. As the energy confinement time was nearly constant for the different shots around the value of 16 ± 2 ms, the ratio τ_{imp}/τ_{Ee} shows the same correlation versus the elongation as τ_{imp} alone (Fig.2c). This factor-of-three decrease of the ratio τ_{imp}/τ_{Ee} is attractive for advanced, elongated tokamak reactor designs.

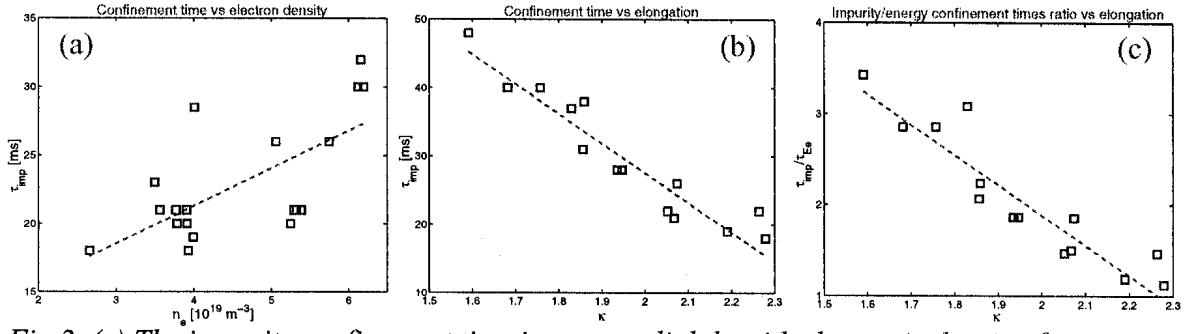

Fig.2. (a) The impurity confinement time increases slightly with electronic density, for constant geometry in diverted plasmas. (b) Elongation scan on limited plasmas, in which q_{eng} was kept approximately constant. Impurities show lower confinement times for high elongations not only as an absolute value, but also in comparison with the electron energy confinement time (c), which is roughly constant in this scan.

4. Transport simulations

A series of simulations have been conducted by means of the 1-D particle transport code STRAHL[1],[3], which provides the time evolution of the local density and soft X-ray emissivity of the injected neutral impurities. The results are used to reconstruct the signals as they would be measured by each chord of the system. Some input parameters, namely the plasma background (electron density and temperature), its geometry, the sawtooth frequency and the inversion radius are directly taken from the TCV experimental results. The transport parameters such as diffusion coefficient, pinch velocity and the recycling coefficient are free inputs and are adjusted such as to reproduce the real signals from several chords simultaneously, on the basis of the fwhm and the exponential decay time τ_{imp}.

Even if the signal shape is very sensitive to D and v, the simulations show that the recycling coefficient just affects the intensity level of the residual asymptotic signal, having very little effects on the shape of the peaked part of the signal. Its value, defined as the ratio N_{SOL}/N_{wall} of the impurity density in the scrape-off layer and in the walls, lies in the range $5–6 \cdot 10^{-6}$ and can be kept constant in the search for the best fitting set of the transport parameters.

Simulations (Fig.3) assume a parabolic radial dependence of the diffusion coefficient, $D = A + B\rho^2$, and a linear radial dependence of the pinch velocity, $v = v_1\rho$, where A, B and v_1 are free parameters. In agreement with the real measurements, the decay time τ_{imp} on many chords is the same, suggesting that the final part of the impurity outflow consists in the decay of the fundamental mode of the solution of the diffusion equation. In order to obtain agreement between the measured and simulated fwhm throughout the cross-section, the real sawtooth frequencies and mixing radii have to be used as conditions in the simulations. The sawtooth effect is modelled by assuming that at crash times the profile of the impurity density is flattened inside the mixing radius, conserving the total number of particles[3]. The mixing radius is assumed to be 1.4 times the inversion radius. It is evident from these simulations that sawteeth play a major role in the transport of impurities in the plasma core. As a general observation, in central viewing chords the simulated signal without sawteeth shows a higher fwhm. Fig.3b shows their effect on the shape of a signal, when the transport parameters are fixed for the two runs. As it can be expected, sawteeth increase the inward flux at the beginning of the process and the outward flux in the last part, thus shortening both the fwhm and the decay times.

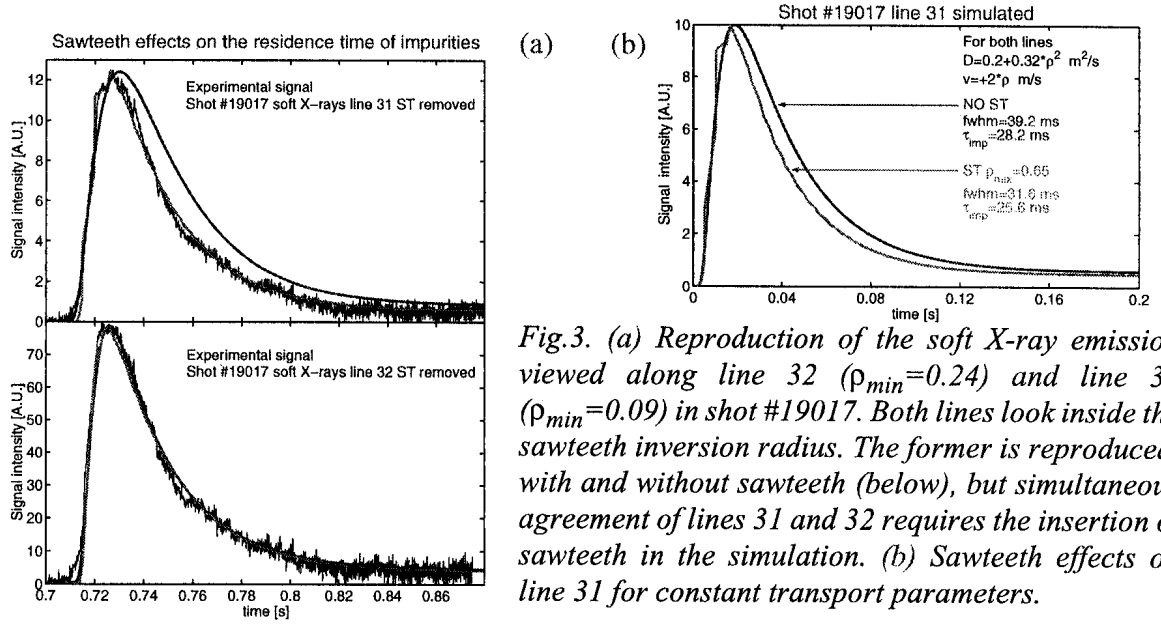

Fig.3. (a) Reproduction of the soft X-ray emission viewed along line 32 (ρ_{min}=0.24) and line 31 (ρ_{min}=0.09) in shot #19017. Both lines look inside the sawteeth inversion radius. The former is reproduced, with and without sawteeth (below), but simultaneous agreement of lines 31 and 32 requires the insertion of sawteeth in the simulation. (b) Sawteeth effects on line 31 for constant transport parameters.

$D=0.2+0.075\rho^2$ m^2/s, $v=+4\rho$ m/s, no ST
$D=0.2+0.3\rho^2$ m^2/s, $v=+2\rho$ m/s, ST, f_{ST}=0.2kHz, ρ_{mix}=0.65

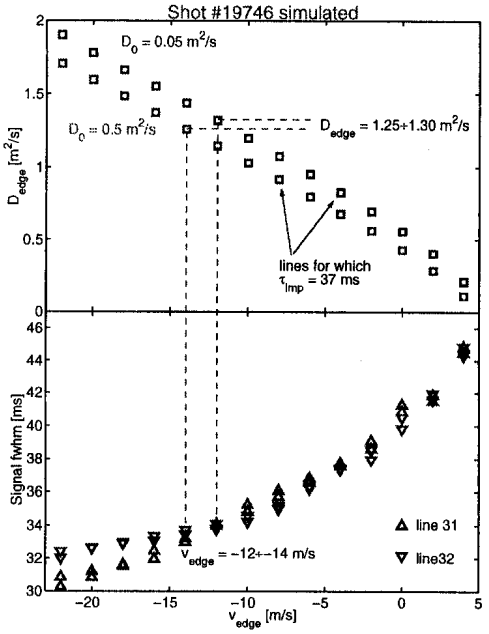

Fig.4. For two values of the central diffusivity (D_0=0.05m²/s and D_0=0.5m²/s), a scan of the edge pinch velocity is performed. The value of D_{edge} is found so to get the correct τ_{imp}=37ms, then the good set of parameters arises from the fwhm value, in this case fwhm=33.5ms. Shot parameters: κ=1.83, δ=0.26, I=436kA, n_e=5.8 · 10¹⁹ m^{-3}, ρ_{mix}=0.7, limited plasma.

From Fig.4 it is evident that the determination of the transport parameters presents some difficulties. In particular the edge pinch velocity cannot be determined accurately, as the fwhm for the signals from both lines 31 and 32 is fairly insensitive to the velocity. The central diffusivity D_0 is undetermined as well by τ_{imp} and the fwhm, due to the overwhelming contribution of the sawteeth to the transport phenomena in the central part of the plasma. On the other hand, the edge diffusivity D_{edge} is quite well determined, even if various different values are assumed for the central diffusion coefficient. In the example shown in Fig.4, for any D_0 lower than 0.5 m²/s, the interval of the possible D_{edge} values, around 1.30 ± 0.05 m²/s, is determined within a small error margin.

The best fitting transport coefficients have been obtained for some of the shots of the elongation scan shown above. While the velocity does not seem to show a correlation with the elongation (Fig.5b), the edge diffusivity clearly increases (Fig.5a) from D_{edge}=0.2m²/s for κ=1.68 to D_{edge}~1m²/s for κ=2.26, as it was expected from the lower confinement times combined with larger plasmas. The higher sawteeth frequency for the elongated plasmas in this scan (f_{ST}=0.2kHz for κ=1.68 to f_{ST}=0.4kHz for κ=2.26) may contribute to the fast radial transport of the impurities in the core of highly elongated plasmas, but their effect is not sufficient to explain the large observed reduction of τ_{imp}.

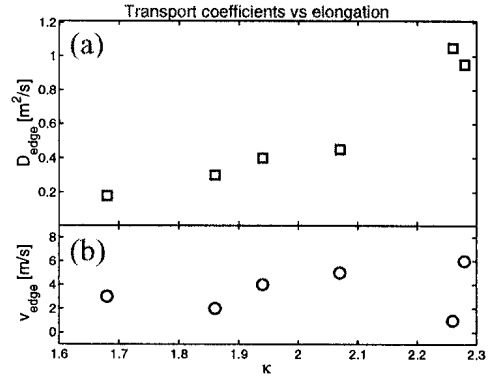

Fig.5. (a) The dependence of the edge diffusivity on the elongation. (b) The corresponding edge velocity does not seem to be correlated. The best fitting pinch velocity is found to be outward, but the uncertainty on its value is large.

Acknowledgements

This work was partly supported by the Swiss National Science Foundation. We wish to thank R. Dux for providing the STRAHL code.

References

[1] K. Behringer, JET Report No. JET-R(87) 08, 1987

[2] T. Dudok de Wit et al., *Phys. Plasmas* **5** (1998) 1360

[3] R. Dux, IPP Garching, STRAHL User Manual, private communication (2000)

Optimisation of $N = 6$ Helias-Type Stellarator

A.A.Subbotin[1], M.I.Mikhailov[1], J.Nührenberg[2], M.Yu.Isaev [1], W.A.Cooper[3], M.F.Heyn[4], V.N.Kalyuzhnyj[5], S.V.Kasilov[5], W.Kernbichler[4], V.V.Nemov[5], V.D.Shafranov[1]

[1] *Russian Research Centre "Kurchatov Institute", 123182, Moscow, Russia*
[2] *Max-Planck-Institute für Plasmaphysik, Teilinstitut Greifswald IPP-EURATOM Association, D-17491 Greifswald, Germany*
[3] *Centre de Recherches en Physique des Plasmas, Association Euratom-Confédération Suisse, Ecole Polytechnique Fédérale de Lausanne, PPB, 1015 Lausanne, Switzerland*
[4] *Institut für Theoretische Physik, Technische Universität Graz, Graz, Austria*
[5] *Institute of Plasma Physics, National Science Center "Kharkov Institute of Physics and Technology", 61108, Kharkov, Ukraine*

Abstract. Collisionless particle confinement in stellarator configurations in which the lines of the magnetic field strength $B = const$ lie on a helical path on the magnetic surfaces is investigated numerically for a six-period system. The optimisation is performed with different penalty functions that are connected with the pseudosymmetry condition and the condition that the second adiabatic invariant $J_{||}$ forms closed contours. In addition, the effect of β on the particle confinement is studied.

1. Introduction. The fulfillment of the quasisymmetry (qs) condition [1] for systems in which the lines $B = const$ lie in the helical direction on the magnetic surfaces leads to conservation of the invariant $\Psi + \rho_{||}F = const$ of the equations of motion in the drift approximation and, thus, to improvement of the collisionless particle confinement. It was shown [2] that the qs condition cannot be fulfilled exactly in the whole plasma volume. In Ref. [3] the less restrictive condition of pseudosymmetry (ps) was suggested. The ps condition means the absence of local extrema of B along the magnetic field lines.

In the present paper, the possibility to fulfill the ps condition is studied numerically and the effect of its fulfillment on the collisionless particle confinement is investigated. It is shown that the fulfillment of the ps condition itself is not sufficient for significant improvement of the particle confinement. Because of this, the condition of closure of the $J_{||}$ contours was added to the penalty function. The corresponding results are presented for both small and large values of β. In addition, results of neoclassical transport calculations for these optimised configuration are presented.

2. Optimisation toward pseudosymmetry. The starting point for the optimisation is an N=6 Helias-type configuration with a Mercier stability limit of about $\beta \approx 5\%$.

In Ref. [4], the mathematical formulation of the ps condition was presented. It requires $\mathrm{d}B/\mathrm{d}\theta_B \equiv 0$ along the lines $\iota\partial B/\partial\theta_B + \partial B/\partial\zeta_B = 0$. This condition alone was used for the construction of the penalty function. As a result, a configuration very close to ps was found. Fig. 1 shows the behaviour of the lines $B = const$ on the magnetic surface $s = 0.9$ near the boundary (s is proportional to the square of the average minor plasma radius) for the initial and the ps-optimised configurations. The confinement properties of these configurations were studied by direct calculations of the guiding centre motion of α-particles. It was shown that fulfillment of the PS condition does not lead to significant improvement of α-particle confinement. The number of the lost particles was reduced by $\sim 10\%$ because of elimination of locally-reflected particles.

3. Closure of the $J_{||}$ contours. The analysis of the behaviour of the $J_{||}$ contours for the ps-optimized configuration has shown that they are open, this being the reason for particle losses. Therefore, a new penalty function was used which vanishes when the $J_{||}$ contours are closed for all reflected α-particles born at 1/4 of the plasma minor radius. Depending on the geometry of the configuration and mainly on the β value, two different possibilities can be realised, with either maximum or minimum value of $J_{||}$ in the centre. In our calculations, we have considered configurations with small ($\beta \approx 0.06\%$) plasma pressure and have required a minimum for $J_{||}$ inside the plasma column. A configuration was identified in which the $J_{||}$ contours were closed for almost all trapped particles born near the magnetic axis. In Fig. 2, contours of $J_{||} = const$ for the initial and optimized configurations are presented. Here the pitch angle which is worst from the viewpoint of confinement is considered.

The results of the direct calculations of α-particles lost are presented in Fig. 3. In spite of the modification of the initial geometry, the configuration found still has a magnetic well.

It was shown that for large enough β values ($\sim 15\%$), the radial dependence of $J_{||}$ is reversed. The confinement in this case is good, too. It is seen from Fig. 4 that for intermediate values of β, particle confinement is deteriorated. A similar effect occurs for configurations with lines $B = const$ along the poloidal angle direction[5].

In Fig. 5, the shape of the boundary surface of the optimised configuration is displayed. The colours here are defined by the magnetic field strength which still exhibits qualitatively quasi-helical behaviour.

4. Computations of transport properties. For the $1/\nu$ transport, the characteristic features of the specific magnetic field geometry manifest themselves [6] through a factor ϵ_{eff} which is an effective ripple modulation amplitude of B and enters the expressions for transport coefficients as a factor $\epsilon_{\text{eff}}^{3/2}$. Computational results for $\epsilon_{\text{eff}}^{3/2}$ are presented in Fig. 6 as functions of $\sqrt{s}$. For an equivalent standard stellarator magnetic field the $\epsilon_{\text{eff}}^{3/2}$ value turns out to be $0.01 \div 0.03$. Therefore, the results obtained are approximately 5 times better than those for the standard stellarator although they are worse than those for the quasi-helically symmetric stellarator [1,6] by more than one order of magnitude.

The trapped particle motion can be described in terms of the second adiabatic invariant $J_{||}$. The variation of $J_{||}$ on a magnetic surface is connected with a displacement of the trapped particle orbit from the magnetic surface. This variation is characterised by a derivative $\partial J_{||}/\partial\theta_0$ where $\theta_0 = \theta - \iota\varphi$, θ and φ being the Boozer angular coordinates. In accordance with [7], we present the results for $\partial J_{||}/\partial\theta_0$ in a normalised form as a functional dependence between dimensionless parameters η and $\gamma = v_{||i}/v_{\perp 0}$ with

$$\eta = \frac{R}{J_\perp}\frac{1}{\tau_b\langle|\nabla\psi|\rangle}\frac{\partial J_{||}}{\partial\theta_0}, \quad \frac{\partial J_{||}}{\partial\theta_0} = \frac{e}{mc}\delta\psi, \quad v_{\perp 0} = \sqrt{J_\perp B_0}.$$

Here $J_\perp = v_\perp^2/B$, τ_b is the bounce period, $\delta\psi$ corresponds to the differential of ψ during τ_b. The normalisation of η is performed in such a way that for the standard stellarator magnetic field, the maximum η value, η_m, equals 0.5. The $v_{||i}$ quantity is $v_{||}$ at the point of a local minimum of B and the γ parameter relates to the pitch angle at this point.

Results of the η calculations are presented in Fig. 7 for an outer magnetic surface. The curves are labelled in accordance with the number of B minima along the magnetic field line. It is seen that non-zero values of η exist in the γ interval $0 \leq \gamma \leq \gamma_{max}$

which corresponds to the trapped particles. In contrast to the standard stellarator, the maximum η value turn out to be smaller than 0.5 and varies with γ. Calculations carried out for inner magnetic surfaces showed that the character of the dependencies of η on γ does not change but the maximum values of η turns out be smaller than those for the outer magnetic surface.

Conclusions. It has been shown through numerical calculations that the pseudosymmetry condition itself is not sufficient for good particle confinement. A new penalty function based on the condition of closure of the $J_{||}$ contours was introduced to the optimisation procedure. As a result of the optimisation, a configuration was found in which almost all α-particles born near the magnetic axis are confined. It was demonstrated that good collisionless particle confinement is possible in configurations far from omnigeneity.

Acknowledgements. This work was supported by INTAS Grant No 99-00592, by Russian-Germany agreement WTZ-V RUS-563-98, by Russian Federal program on support of leading scientific school, Grant No 00-15-96526, by Russian Fund for Basic Research, Grant No 00-02-17105, by the Fonds National Suisse de la Recherche Scientifique, by the Association EURATOM-OEAW and by the Austrian Academy of Sciences.

References

[1] J.Nührenberg and R.Zille, Phys. Lett. A **129** (1988), 113.
[2] D.A.Garren, A.H.Boozer, Phys. Fluids. **B3** (1991), 2822.
[3] M.I.Mikhailov, W.A.Cooper, M.Yu.Isaev, et al., Theory of Fusion Plasmas (International School of Plasma Physics), Bologna: SIF, 185 (1998).
[4] A.A.Skovoroda, Plasma Physics Reports, **24** (1998), 989.
[5] M.I.Mikhailov, M.Yu.Isaev, J.Nührenberg, et al., this conference.
[6] V.V.Nemov, S.V.Kasilov, W.Kernbichler, M.F.Heyn, Phys.Plasmas **6** (1999), 4622.
[7] V.V.Nemov, Phys. Plasmas **6** (1999), 12.

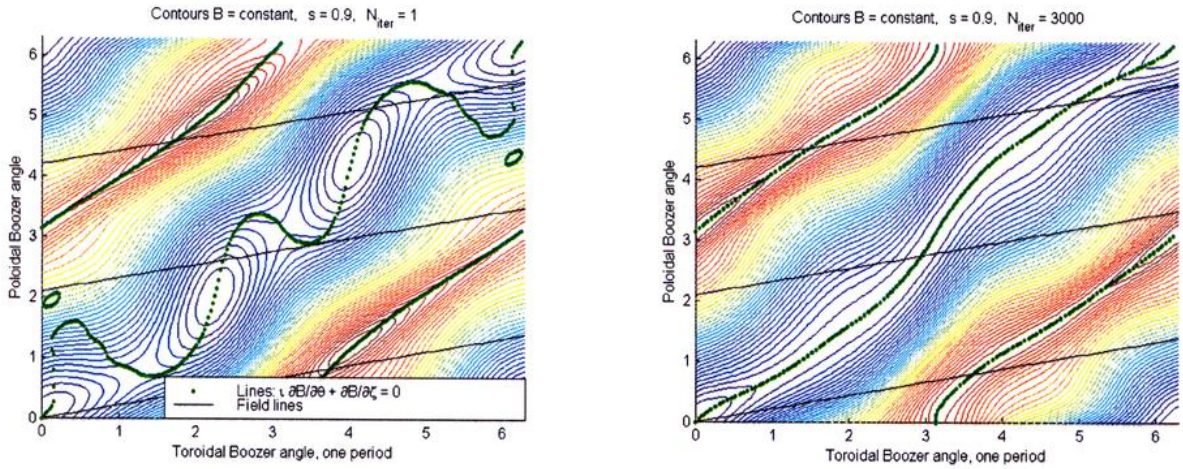

Fig.1. Optimisation of initial configuration to pseudosymmetry. Behaviour of lines B=const on the near boundary magnetic surface s=0.9 for initial (left) and optimised to PS (right) configurations.

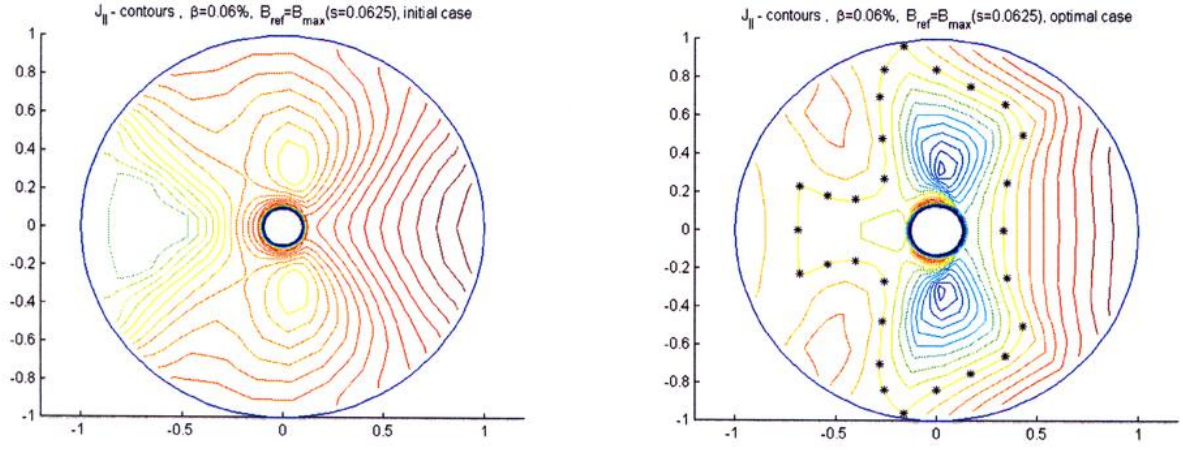

Fig. 2. Contours $J_{\parallel} = const$ for initial and optimal configurations. The worst from the viewpoint of confinement pitch angle is considered.

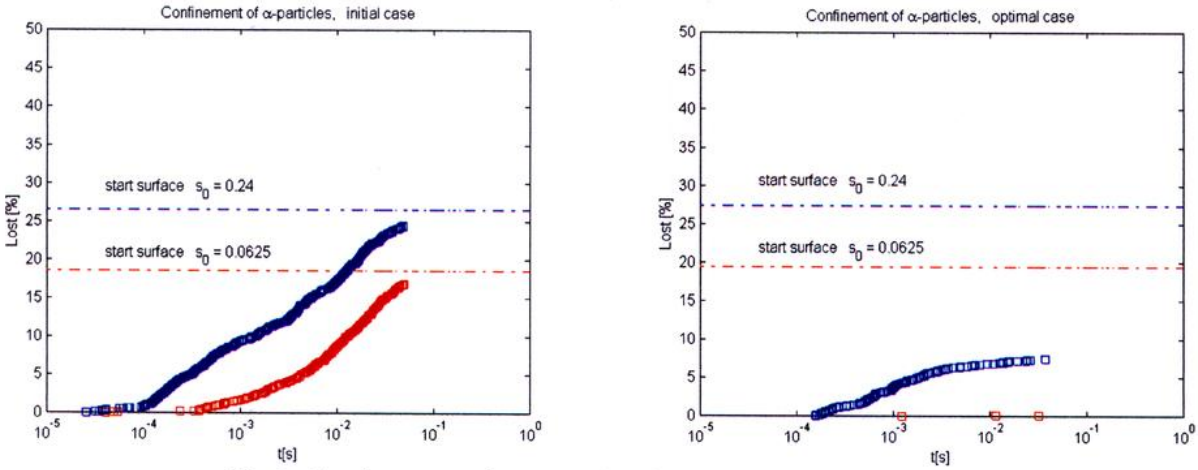

Fig.3. Confinement of α-particles for initial and optimal cases.

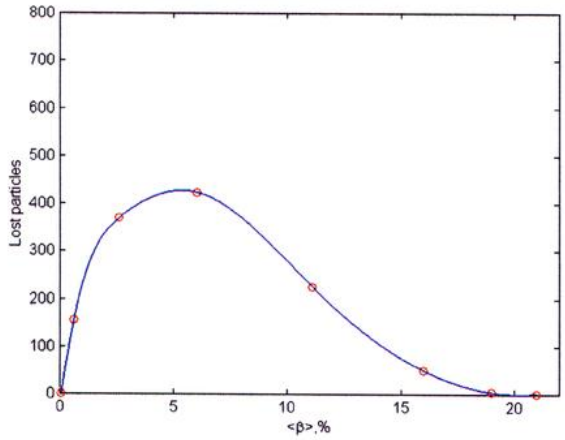

*Fig. 4. Effect of <β> on the particles confinement for the **J-contours optimised** system. Number of test α -particles is 2000. Particles are started at aspect ratio 44.*

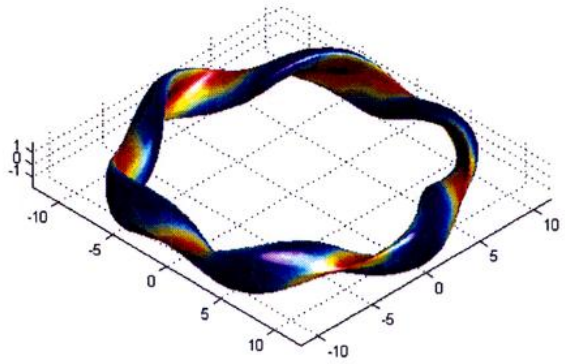

Fig. 5 Shape of the boundary surface of the considered configuration. The colours are defined by the magnetic field strength.

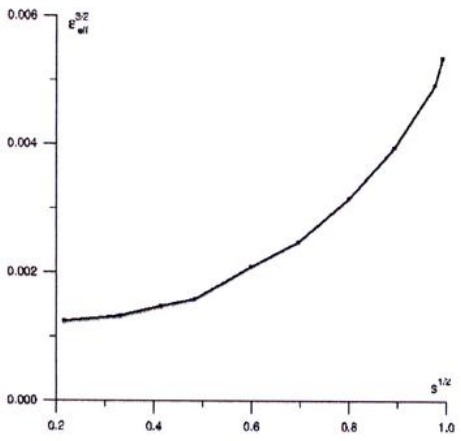

Fig. 6. Dependence of effective ripples amplitude on the averaged magnetic surface radius.

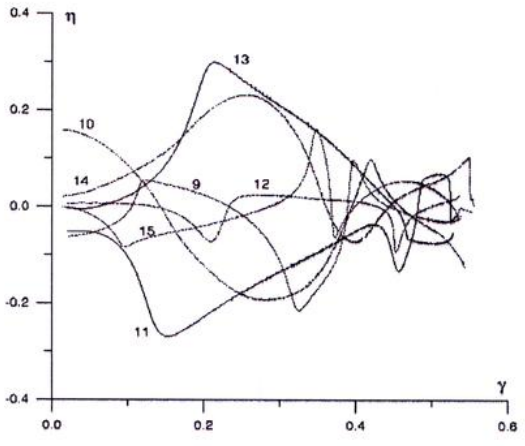

Fig. 7. The results of η calculations. Curves are numbered in accordance to the numbers of B minima along the magnetic field line. In contrast to the standard stellarator the maximum η value turns out to be smaller than 0.5 and varies with γ

PLASMA AND IMPURITY TRANSPORT MODELING OF NBI-HEATED LHD AND HELICAL REACTOR SYSTEMS

K. Yamazaki, M. Tokar[1], H. Funaba, B.J. Peterson, N. Noda,
A. Cooper[2], Y. Narushima, S. Sakakibara, K.Y. Watanabe, H. Yamada,
K. Tanaka, K. Ida, K. Narihara and the LHD Experimental Group

National Institute for Fusion Science, 322-6 Oroshi-cho, Toki, 509-5292, Japan
[1]Institut fuer Plsamaphysik, Forschungszentrum Jelich, D-52425 Juelich, Germany
[2]*Centre de Researches en Physique des Plasma, Ecole Polytechnique Federale de Lausanne, CH-1015 Lausanne, Switzerland*

Abstract

For the precise analysis of toroidal confinement systems, the Toroidal Transport Analysis Code "TOTAL" has been developed and applied to the Large Helical Device (LHD) plasmas and related reactor systems. The new LHD confinement scaling law is derived, which can extrapolate the present data to the reactor regime without confinement improvement.

Slow Relaxation oscillations called "breathing" have been analyzed using the TOTAL code and the physics simulation modeling with impurity sputtering process. The slight change in transport coefficient during oscillation is experimentally found, and roles of high-Z and low-Z impurities are clarified. The breathing waveform and the oscillation period are reproduced depending on plasma density by this modeling.

1. Introduction

Plasma confinement and related impurity behaviors are keys to getting high temperature plasmas and starting reactor plasma operations. In the Large Helical Device (LHD) the confinement times higher than the conventional scaling laws are achieved, which makes it possible to extrapolate the present database to the reactor regime [1]. So-called "breathing" phenomena [2,3] are found in LHD as a result of impurity dynamics. For the explanation and prediction of LHD and reactor plasma confinement, precise transport analysis is required. In this paper, "breathing" plasma analysis and reactor plasma projections are carried out.

2. LHD Transport Analysis Using TOTAL Code

2-1 TOTAL Code Development

For predictive simulation and experimental analysis of toroidal plasmas, a simulation code TOTAL (Toroidal Transport Analysis Linkage) has been developed as an extension of HSTR code [5]. This consists of a 3-dimensional equilibrium with ohmic and bootstrap currents and a 1-dimensional transport with neoclassical loss determined by ambipolar radial electric field as well as anomalous transport (empirical or drift turbulence theory).

2-2 Global Confinement Scaling and Reactor Plasma Projection

NBI-heated plasmas on LHD are analyzed using the TOTAL code. Different from the previous scaling laws, a new global confinement scaling law (New LHD scaling) by regression analysis has been obtained [1] based on heliotron-type experiments:

$$t_{NLHD\#1} = 0.263 P^{-0.58} \bar{n}_e^{0.51} B^{1.01} R^{0.64} a^{2.59}.$$

Units used here are $t_E(s)$, $P(MW)$, $\bar{n}_e(10^{20}m^{-3})$, $B(T)$, $R(m)$, $a(m)$, respectively. This scaling law suggested the strong gyro-Bohm like feature, which is different from previous scaling laws. This feature is also verified by local transport analysis near the edge region. Using this scaling low, Modular Heliotron Reactor plasma [1] can be predicted without confinement improvement.

2-3 Impurity Transport Analysis Using TOTAL Code

Consideration of the transport of impurities and their influence on plasma performance is one of important elements in a consistent predictive modeling. In particular, the development of "breathing" oscillations in LHD [2,3] gives an interesting example of impurity effects in helical devices.

The impurity dynamics is calculated using measured electron temperature and electron density. Figure 1 shows the breathing oscillation of measure input profiles and calculated radial electric field, radiation power and effective Z values. The initial total impurity density was assumed by the percentage of main plasma density. Here the recycling rates of all impurity ions are assumed to be unity. In this analysis, carbon, oxygen, and iron densities are assumed as 1%, 1% and 0.2 %, respectively. Their initial profiles are determined using coronal equilibrium model, and the time-variation of each charge-state impurity ions

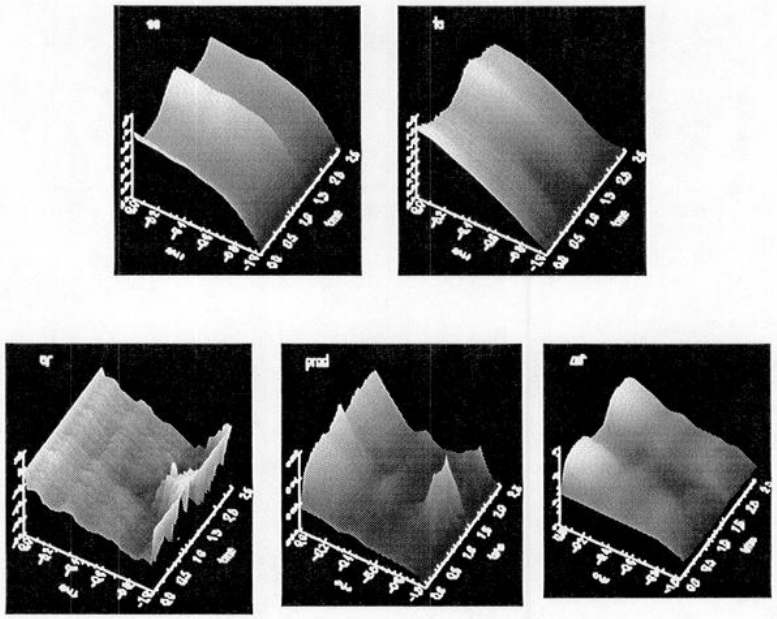

Fig. 1 Transport analysis on LHD plasma.
Upper raw: experimental data (n_e and T_e),
Lower raw: analyzed output (E_r, P_{rad} and Z_{eff})

is dynamically solved by the rate equation of each charge-state and the diffusion equation with the transport coefficient D of 1 m^2/s and without the inward flow (v = 0 m/s). The ambipolar electric field calculated from bulk plasma is negative (ion root), which contradicts with experimental observations. For precise determination of electric field, we might include impurity effects on the ambipolar flux calculation. The radiation profile has two peaks (central and near edge) corresponding to iron and low-Z (carbon and oxygen) impurities, which qualitatively agrees with experimental data.

Typical radial profiles of effective thermal diffusivity are shown in Fig. 2.

$$c_{eff} = -(Q_{NBI} + Q_{RF} - \frac{dW_p}{dt}) / (n_e \frac{d(T_e + T_i)}{dr})$$

In higher density, detached small plasma and low-Z impurity radiation dominant phase, the thermal diffusivity is rather low. On the other hand, in the temperature increase, low radiation and larger attached plasma phase, the diffusivity is slightly high. This transport change might also contribute to the appearance of periodic relaxation oscillations.

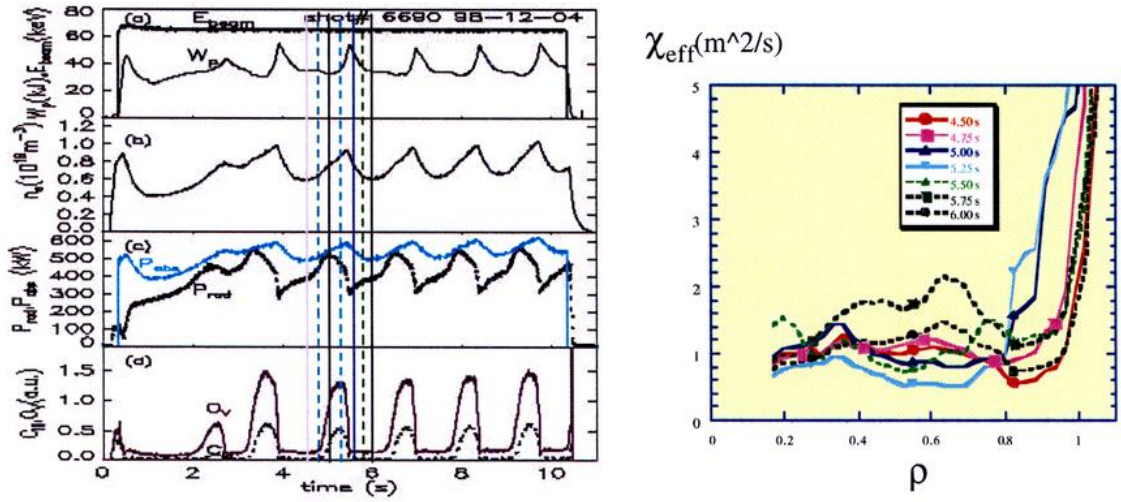

Fig.2 Breathing plasma waveforms and effective thermal diffusivity

3. Physics Modeling on Impurity-Induced Relaxation Oscillation in LHD

In discharges where the plasma touched wall elements of iron, an increase of the electron density in excess of a critical level led to slow with a period of a second oscillations in diverse plasma parameters, e.g., central and edge plasma temperature, integrated radiation losses and intensities of selected spectral lines, line averaged density, etc. A physical picture of this phenomenon proposed recently [5] implies the importance of radiation from both Fe ions in the plasma core and light impurities of C and O at the edge. In phases with a hot edge

the sputtered iron particles penetrate into the plasma core and increase the central radiation losses. This leads to reduction of the heat outflow to the edge and detachment due to radiation of C and O. As a result the iron-sputtering source disappears and Fe ions diffuse out of the plasma. The growing heat flow to the edge causes its reattachment.

With an ultimate goal to perform a self-consistent 1-D time-dependent modeling of "breathing" oscillations by the code TOTAL this has been first run in its interpretive option to reconstruct the behavior of transport coefficients. The results for the effective heat conductivity are shown in Fig.2. A modeling of Fe ion transport gives a diffusivity of 0.15-0.25 m^2/s in agreement with that obtained by the code MIST [4]. These coefficients have been used in a simple numerical model elaborated to check the mechanism of "breathing" proposed in Ref.[5]. The model includes a heat balance for the plasma edge and core, the balance of the main particles and a 1-D time dependent description of the total density of Fe ions with a self-consistently computed source of iron neutrals due to physical sputtering of the divertor. As a result the time evolution of the plasma temperature at the last closed magnetic surface and at the device axis, of the line averaged density, total radiation losses and luminosity of light impurities can be simulated. Figure 3 shows an example of such calculations for an NBI power of 1MW. These results are in agreement with measurements including peculiarities of their time phasing. The observed increase of the oscillation frequency with plasma density n can be reproduced firmly in computations if one assumes that the impurity diffusivity varies proportionally to n as it is predicted by neoclassical theory.

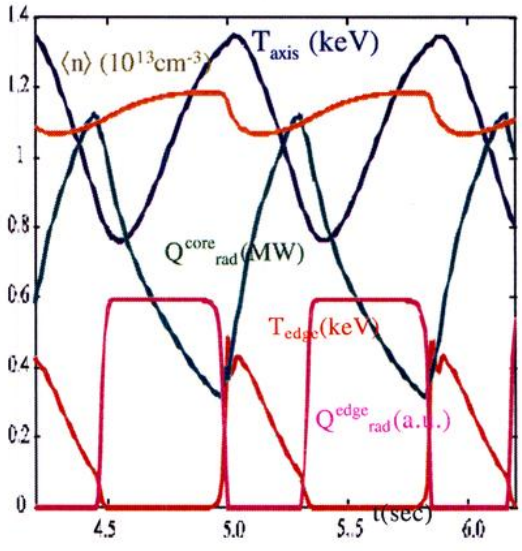

Fig.3 Results of Numerical Modeling

References

[1] K. Yamazaki et al., 18th IAEA Fusion Energy Conference (Sorrento, Italy, 2000) FTP2/12

[2] Y. Takeiri et al., Plasma Phys. Control. Fusion 42 (2000) 147.

[3] B.J. Peterson et al., Nucl. Fusion 41 (2001) 519.

[4] K. Yamazaki and T. Amano, Nucl. Fusion 32, 633 (1992).

[5] M.Z. Tokar et al., Physics of Plasmas 7 (2000) 4357.